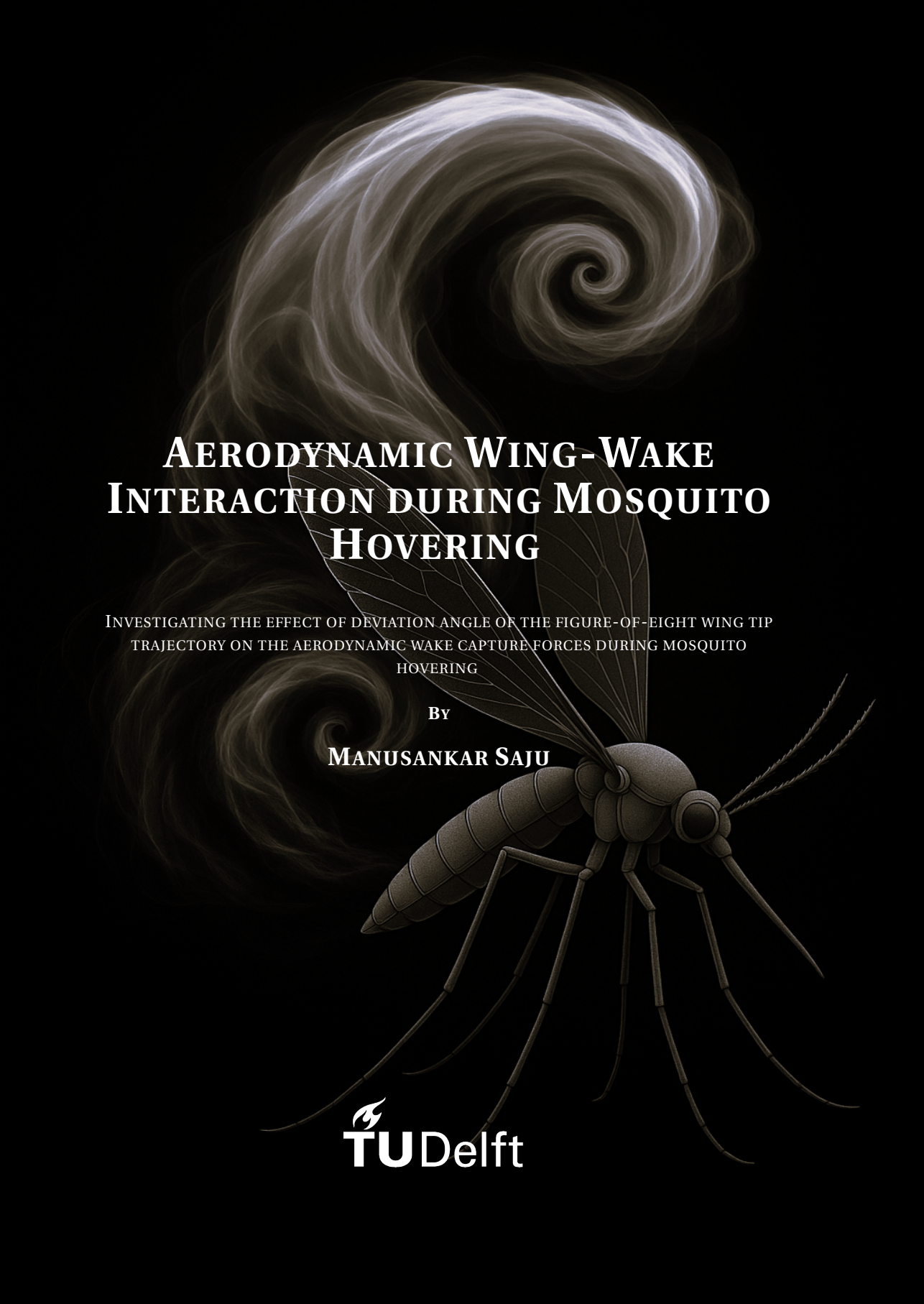

Aerodynamic Wing-Wake Interaction during Mosquito Hovering

Investigating the effect of deviation angle of the figure-of-eight wing tip trajectory on the aerodynamic wake capture forces during mosquito hovering

By

Manusankar Saju

TU Delft

AERODYNAMIC WING-WAKE INTERACTION DURING MOSQUITO HOVERING

INVESTIGATING THE EFFECT OF DEVIATION ANGLE OF THE FIGURE-OF-EIGHT WING TIP TRAJECTORY ON THE AERODYNAMIC WAKE CAPTURE FORCES DURING MOSQUITO HOVERING

Thesis Report
(ME55035)

to obtain the degree of Master of Science
at the Delft University of Technology,
to be defended publicly on September 16th, 2025 at 9:45 AM.

by

Manusankar Saju

Student ID: 5936101

Energy, Flow and Process Technology (EFPT),
Department of Mechanical Engineering,
Technical University of Delft,
Netherlands

TU Delft Delft University of Technology

Supervisor TU Delft:	Dr. A. J. L. L. Buchner
Co-Supervisor:	Ir. Dirk de Boer
Thesis Committee:	Dr. A. J. L. L. Buchner Dr. J. F. L. (Hans) Goosen Dr. H. Burak Eral Ir. Dirk de Boer
Institution:	Delft University of Technology
Thesis Duration:	December 2024 - September 2025

"Aerodynamically, the bumblebee shouldn't be able to fly,
but the bumblebee doesn't know it,
so it goes on flying anyway."

– Mary Kay Ash

ACKNOWLEDGEMENTS

I would like to express my deepest gratitude to my Professor and lead supervisor, Dr. Abel-John Buchner, for his invaluable guidance, unwavering support, and profound expertise throughout this academic journey. His insightful feedback, encouragement and enthusiasm have been instrumental in shaping my understanding of the research landscape.

I am equally indebted to my co-supervisor, Ir. Dirk de Boer, whose constant backing, technical knowledge, and willingness to engage in thoughtful discussions have significantly enhanced the quality of this research. His patience in addressing my questions and providing direction for my experimental work has been truly remarkable.

My sincere appreciation extends to Gertjan Mulder, my lab supervisor and technician, whose practical expertise has been crucial in setting up my experimental apparatus. His hands-on support on the Staubli Robot was invaluable in establishing the laboratory setup for the experiments.

I would like to acknowledge the enduring encouragement and steadfast presence of my Amma and Appa, whose guidance and understanding have been essential throughout the duration of this work. Their unfailing confidence in my abilities and their continuous moral and emotional support have been a source of strength and determination in bringing this research to completion.

My friends have played an incredible role throughout this journey, whose companionship and willingness to offer perspective beyond the academic scope have contributed to maintaining balance and focus during challenging stages. Their readiness to lend support and foster an environment of positivity has been truly priceless. Special thanks to Ricenberg (Jelly, AshGPT, Rauther, Jos, Kam, Aps and Lite). Love you guys!

I also extend my sincere gratitude to Dr. J. F. L. (Hans) Goosen and Dr. H. Burak Eral for their valuable participation as members of the committee.

Manusankar Saju
Delft, September 2025

MOTIVATION

Despite their small size, mosquitoes exhibit some of the most unconventional and counterintuitive flight mechanics found in nature. Unlike most insects, which already rely on unsteady aerodynamic mechanisms for lift generation, mosquitoes operate at the extreme end of the kinematic spectrum, combining unusually high wingbeat frequencies with small stroke amplitudes. These unique kinematic conditions are hypothesized to influence the unsteady aerodynamic mechanisms during their flight. Their ability to sustain stable hovering and execute precise manoeuvres depends on a combination of unsteady aerodynamic phenomena, including the interaction with their own wake, dynamic forces arising from wing rotation, and stable vortex formation near the wing leading edge.

This research is driven by two primary motivations. The first relates to the field of flapping-wing micro aerial vehicles (FWMAVs), which seeks to emulate biological flyers to enhance agility and maneuverability in small-scale aerial drones. While current understanding of mosquito flight mechanics remains incomplete, particularly regarding the utilization of wake capture, advancing knowledge in this area could potentially contribute to the design and optimization of FWMAVs for applications such as search-and-rescue missions, environmental monitoring, and military reconnaissance, where precise control and efficiency are critical.

Secondly, from a public health perspective, mosquitoes represent one of the deadliest disease vectors, transmitting ailments including malaria, dengue, and other life-threatening illnesses worldwide. Despite extensive control strategies, their adaptability and resilience continue to challenge vector management efforts. A fundamental understanding of mosquito flight mechanics may provide novel insights that support the development of more effective vector control methods, ultimately aiding in the reduction of global disease burden. The unique aerodynamic characteristics of mosquitoes, distinguishing them from other insects, therefore provide a valuable research opportunity bridging bio-inspired engineering and global health imperatives.

It is important to note that this study does not presuppose an inherent fluid dynamic optimality in the propulsion mechanisms of mosquitoes. Instead, this research aims to develop a framework for objectively evaluating the optimality - or lack thereof - of the interactions between the mosquito's wing motion and the vortices shed during its flapping cycle, specifically as influenced by variations in the vertical component of wing movement (deviation angle).

CONTENTS

ABSTRACT

Mosquitoes of the species *Aedes Aegypti* exhibit a particularly distinctive figure-eight shaped wingtip trajectory, which includes a vertical component of motion (characterized by deviation angle) that is hypothesized to influence aerodynamic force generation through interactions with the wing's own wake, referred to as wake capture. While standard quasi-steady (QS) aerodynamic numerical models can effectively predict the forces generated by translational, rotational, coupling and added mass effects during wing motion, they do not capture the additional forces arising from wake interaction.

This study aims to leverage this known limitation of quasi-steady models, to investigate the influence of deviation angle on wake capture forces during hovering flight. Aerodynamic forces were measured using a robotic flapping-wing apparatus programmed to replicate biologically plausible kinematics of a mosquito, across a range of deviation angles $0° - 6°$ (including an outlier at 7.5°). By subtracting forces predicted by a validated quasi-steady model from the experimentally measured forces, the residual unsteady component associated with wake capture was isolated and quantitatively analyzed.

The results of this study demonstrated that wake capture forces play a beneficial aerodynamic role in the mid-to-high deviation angle range, specifically between approximately 4° and 6°. Within this interval, the wake capture lift and drag forces exhibit relatively elevated mean values, and the experimentally observed lift-to-drag ratio surpasses quasi-steady predictions, indicating enhanced aerodynamic efficiency. Correspondingly, power utilization increases, and flapping efficiency peaks near 5° to 6°, collectively highlighting an optimal regime where unsteady wake interactions benefit aerodynamic performance. This favorable trend could be attributed to the pronounced out-of-plane wing motion at these deviation angles, which intensifies three-dimensional wake structures and possibly promotes more effective wing-wake vortex interactions that augment lift and overall flapping efficiency.

In spite of the high uncertainty in the force sensor readings, this study successfully established a kinematically accurate, high-fidelity setup for examining the influence of deviation angle on wake capture phenomena. The elevated noise from the inbuilt force sensor and structural vibration in the wing assembly were identified as the primary limitations, which could only be fully resolved through hardware replacement beyond the present scope. Nevertheless, the findings provide novel insights into the role of deviation angle in shaping wake capture forces, with both scientific implications for advancing flapping-wing micro air vehicle (FWMAV) design and societal relevance given the connection between mosquito flight and public health.

1

INTRODUCTION

1.1. THE ENIGMA OF INSECT FLIGHT: NATURE'S AERODYNAMIC MARVEL

The flight of insects represents a significant aerodynamic phenomenon in nature that has long captured scientific curiosity. The origins of winged insects are deeply rooted in the distant past, with their first flight likely occurring nearly 350 million years ago [58][24]. Over hundreds of millions of years, natural selection has refined their wings, kinematics, and sensory systems to achieve specialized flight capabilities [28].

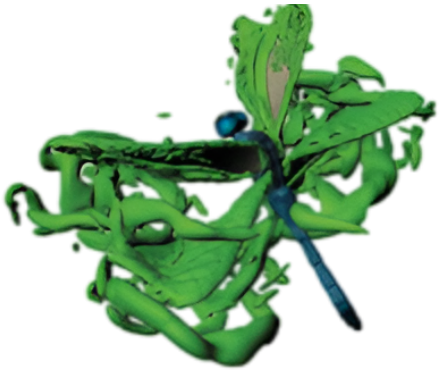

Figure 1.1: Visualization of the complex, three-dimensional flow structures generated around the wings of a dragonfly during flapping flight [28]. In this image, produced using computational flow diagnostics, the green isosurfaces denote regions of high vorticity magnitude, thereby highlighting vortex formation and fluid-structure interactions that characterize the unsteady aerodynamics of insect flight. Such visualizations, enabled by advances in computational techniques, provide critical insight into the mechanisms governing force generation in flapping-wing insects [47].

1

The flight of insects has been a fundamental factor in their evolutionary success, providing flying insects with measurable advantages over their flightless ancestors [47]. The ability to take to the air has conferred insects with enhanced mobility, enabling them to evade predators with improved agility, locate food sources with precise spatial and temporal resolution, and colonize new habitats that would otherwise be inaccessible. Certain species demonstrate controlled flight maneuvers, such as backward takeoff to evade threats, lateral flight for obstacle navigation, or landing on inverted surfaces with notable positional accuracy [13]. These complex aerial behaviors arise from an integration of physiological and anatomical specializations that remain only partially characterized. Such specializations include wing structures exhibiting considerable flexibility, finely tuned neuromuscular control systems, and sophisticated sensory feedback mechanisms, in conjunction with the intricate aerodynamic interactions involved [16]. Collectively, these attributes have enabled insects to occupy diverse terrestrial ecosystems.

From a physics standpoint, the fluid mechanics underlying insect flight capabilities have been a subject of sustained scientific interest and discussion. Insect flight initially seems to contradict conventional steady aerodynamic principles developed for fixed-wing aircraft. This contradiction was notably exemplified by the "bumblebee paradox" [42], in which early aerodynamic analyses indicated that bumblebees should be incapable of flight due to the mismatch between their relatively large body mass and small wing size. This paradox resulted from oversimplified assumptions inherent in steady-state aerodynamic models, which did not incorporate the unsteady aerodynamic forces produced by flapping wing motions. Contemporary aerodynamic theories have addressed this issue by integrating unsteady flow dynamics and mechanisms of vortex generation, thereby resolving the paradox. Nevertheless, it highlights the complex nature of insect flight mechanics. The diminutive scale of insects, their high wingbeat frequencies, often reaching several hundred cycles per second, and distinctive reciprocal wing flapping further complicate conventional, simplified aerodynamic estimations.

Understanding the complexities of insect flight demands careful attention to subtle aerodynamic phenomena that often elude purely theoretical models or isolated experimental approaches. To address these challenges, recent advances in experimental techniques, such as high-speed imaging and digital particle image velocimetry (DPIV) [33, 53], combined with computational simulations have significantly enhanced our ability to visualize and quantify the unsteady flow structures surrounding flapping wings [47] as shown in Figure 1.1. These tools reveal intricate mechanisms such as leading-edge vortex formation and stability, wake capture, and vortex shedding patterns, as well as the dynamic deformation and response of flexible insect wings to aerodynamic loading [47, 28].

1.2. A BLUEPRINT FOR MICRO AERIAL VEHICLES (MAVS)

From an engineering point of view, insect aerodynamics offer untapped potential for advancing flapping-wing micro aerial vehicles (FWMAVs), shown in Figures 1.2 and 1.3. These bio-inspired technologies mimic natural flyers like insects to achieve unparalleled agility and maneuverability compared to fixed-wing or rotary-wing designs [50]. FW-

MAVs have diverse applications ranging from search-and-rescue missions to environmental monitoring and military reconnaissance. Examples of successful FWMAV prototypes include the Delfly, developed at the Technical University of Delft [14], and the Microbat developed by Aerovironment in collaboration with Caltech [50]. By studying insect flight mechanics - including wing geometry, kinematics, and lift generation, researchers aim to optimize MAV performance while minimizing energy consumption.

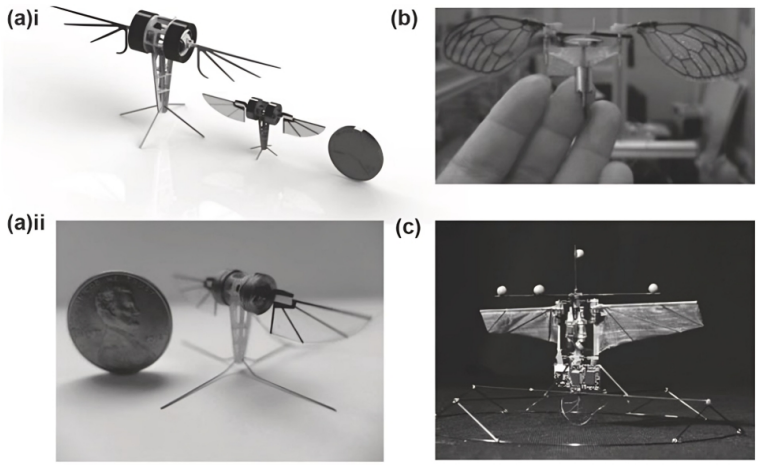

Figure 1.2: Examples of bio-inspired micro aerial vehicles, including robotic insects and flapping-wing drones, shown alongside a coin for scale [9]. (a) Electromagnetic flapping-wing robots (b) A motor-driven flapping wing robot (c) Hummingbird-mimicking flapping-wing robot with direct drive

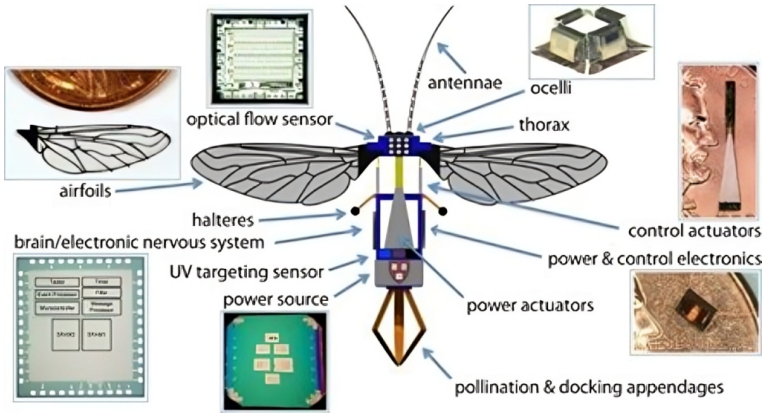

Figure 1.3: Diagram of a bio-inspired robotic insect showcasing its components such as airfoils, optical flow sensors, electronic nervous system, power source, and pollination appendages [52].

SIGNIFICANCE OF HOVERING FLIGHT

One particularly fascinating aspect of FWMAV research is the study of hovering flight. Hovering is a critical capability for many MAV applications, including search-and-rescue missions, environmental monitoring, and detecting hazardous agents like biological or chemical substances. Hovering flight serves as an ideal benchmark for evaluating FW-MAV designs due to its simplicity and practicality [24]. For one, the absence of forward flight speed simplifies lift and power calculations because the surrounding airflow is essentially stationary relative to the wing motion, eliminating additional aerodynamic complexities like forward translational velocity, induced drag, and asymmetric flow patterns, thereby allowing forces and power to be computed based solely on the wing's flapping kinematics and local flow interactions. Additionally, hovering provides a stable testbed for assessing control mechanisms while minimizing pendulum-like instabilities [47]. Studies have also revealed that lift coefficients (defined as the ratio of the aerodynamic lift force to the product of fluid dynamic pressure and wing planform area, representing the wing's efficiency in generating lift relative to its size and the fluid conditions) tend to peak during hovering before declining at higher speeds, making it a valuable reference point for optimizing flight performance across different speed ranges [19]. Moreover, if an insect-inspired MAV can hover efficiently, it is likely capable of sustaining its weight and powering its wings across a broad range of speeds [58, 24, 42].

1.3. MOSQUITO FLIGHT: UNIQUE KINEMATICS AND SOCIETAL IMPLICATIONS

Mosquitoes stand out as remarkable outliers in the realm of insect flight. Unlike their counterparts, these tiny insects employ a unique set of wing kinematics that challenge our understanding of aerodynamics at small scales. Mosquitoes flap their wings at extraordinarily high frequencies, sometimes exceeding 800 Hz, which is significantly faster than any other insect of comparable size [27]. Coupled with this rapid wing beat is an unusually small stroke amplitude of about 40° to 45°, less than half that of other measured insects [7]. This combination of high-frequency, low-amplitude wing movements and a very distinctive wing-tip trajectory (explained in section 2.2.1) compels mosquitoes to rely on their extraordinary physiology and a set of unique unsteady aerodynamic mechanisms, such as wake capture, delayed stall, Kramer effect and many more (explained in section 2.1.2), to support their flight [58][33]. Notably, mosquitoes have been shown to maintain stable flight even after tripling their body weight with blood meals [33]. However, it remains inconclusive whether this feat is attributed to their extraordinary biology (such as unique muscle structure and anatomy) or their ability to utilize the aforementioned unsteady aerodynamics.

Mosquitoes' flight mechanics are not only a scientific curiosity but also carry profound implications for public health. As vectors of diseases like malaria, dengue, Zika virus, and chikungunya, mosquitoes are responsible for over one million deaths annually and infect hundreds of millions more [40][1] as shown in figure 1.4. Climate change has exacerbated this crisis by enabling mosquito populations to expand into new territories, with dengue cases alone showing a 228% increase in 2024 compared to the previous year. Traditional control methods, such as insecticide-treated bed nets, indoor resid-

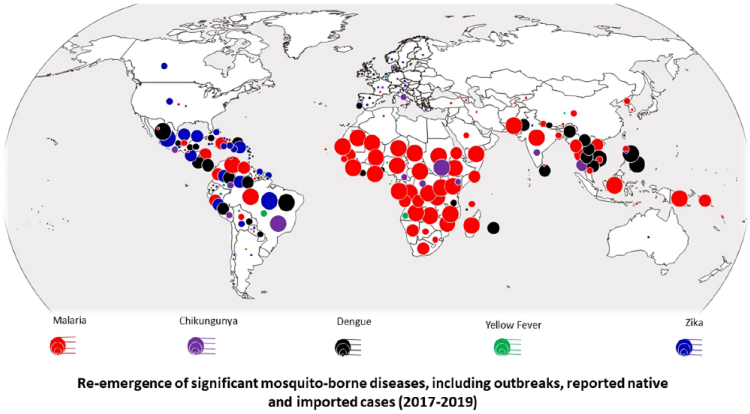

Figure 1.4: The global re-emergence of significant mosquito-borne diseases, including malaria, chikungunya, dengue, yellow fever, and Zika, highlighting outbreaks and reported cases (native and imported) from 2017 to 2019 using color-coded markers[52].

ual spraying, and larvicides, have proven insufficient in combating these resilient vectors, prompting innovative approaches such as genetically modified mosquitoes and Wolbachia-infected specimens designed to reduce populations or block disease transmission [8][44][2]. However, the adaptability of mosquito populations often undermines these strategies over time [3].

Understanding mosquito flight mechanics, particularly during hovering, could provide crucial insights for enhancing these control methods [59]. For instance, this knowledge could improve the design of genetically modified mosquitoes with better mating fitness, thereby optimizing the release strategies for Wolbachia-infected mosquitoes [4]. The convergence of public health imperatives and aerodynamic innovation thus makes the study of mosquito flight an interesting area of research.

2

LITERATURE REVIEW

2.1. UNCONVENTIONAL FLUID DYNAMICS OF INSECT FLIGHT

2.1.1. WHY STEADY THEORIES CAN'T FULLY EXPLAIN INSECT FLIGHT

Insect flight presents a fascinating aerodynamic challenge, defying classical steady-state theories that explain conventional aircraft and avian flight. Observations reveal that insects generate lift forces exceeding twice their body weight, a feat unattainable under traditional steady aerodynamic calculations[15]. Wind tunnel experiments and blade-element analyses consistently show that the effective lift coefficients required for insect flight, measured under highly unsteady, flapping-wing conditions : (1.5 – 2), exceed typical steady-flow lift coefficients encountered by conventional aircraft, implying the presence of unsteady lift-generating mechanisms [47].

The intricacies of insect wing kinematics, characterized by a sequence of oscillatory motions, such as pronation (the forward rotation of the wing preparing for downstroke), downstroke, supination (the reverse rotation preparing for upstroke), and upstroke, shown in Figure 2.1, generate unsteady flow phenomena such as rotational forces and leading-edge vortices (LEVs) that enhance lift [48]. These mechanisms lie beyond the scope of steady-state aerodynamics, which cannot account for the dynamic forces observed in insect flight[59].

For instance, the flow field structures such as leading edge vortices (LEVs), which are regions of concentrated, stable swirling airflow formed along the front edge of the wing, shown in Figure 2.2 along with unsteady phenomenon such as delayed stall, play a crucial role in sustaining lift during wing strokes [48] (explained in section 2.1.2), as demonstrated in studies on hawkmoths and dragon flies [24]. However, exceptions like mosquitoes, which use high flapping frequencies and small stroke amplitudes, challenge the universality of these mechanisms. The limited time available during each wingbeat cycle restricts the development of fully formed leading-edge vortices (LEVs), preventing them from attaining their maximum aerodynamic potential before wing reversal. In this context, "fully developed" denotes the stage at which an LEV achieves optimal circulation

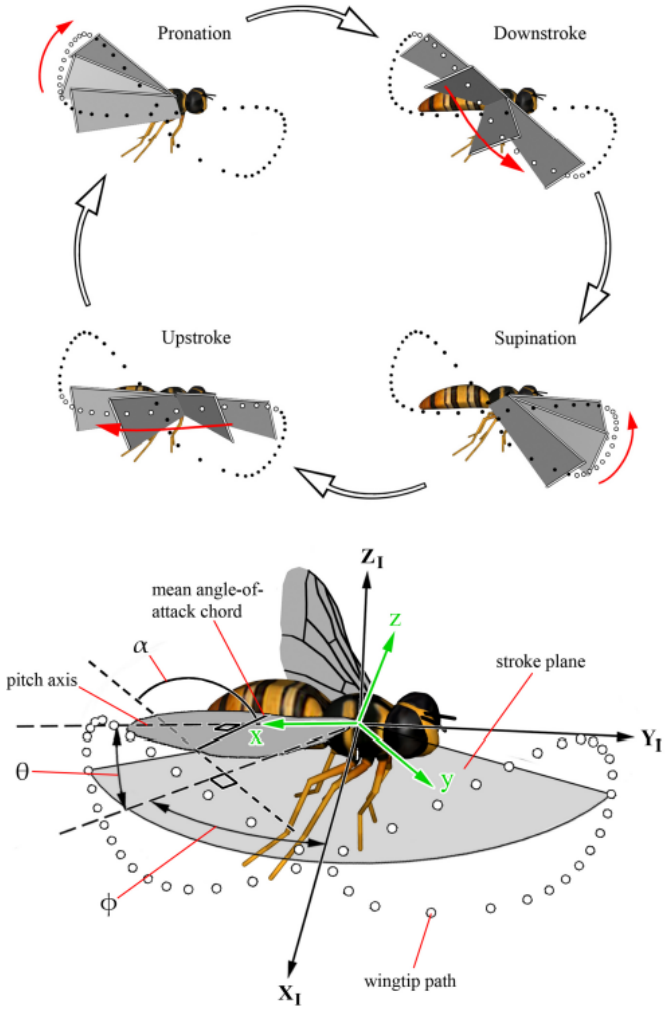

Figure 2.1: The flapping cycle of a hovering insect, illustrating key phases - pronation, downstroke, supination, and upstroke - alongside the kinematic parameters defining wing motion. The bottom diagram details the stroke plane, wingtip path, pitch axis, and mean angle of attack in a 3D coordinate system [41].

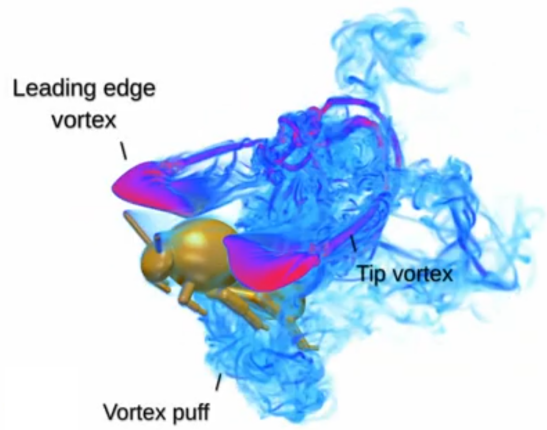

Figure 2.2: Visualization of a leading-edge vortex (LEV) formed along the front edge of a flapping insect wing. The LEV appears as a region of concentrated, swirling airflow near the leading edge, stabilized during the downstroke. This flow structure is critical for sustaining lift in insect flight by maintaining a low-pressure region over the wing [48, 28, 25]. The aerodynamic significance of LEVs and related unsteady mechanisms is discussed further in section 2.1.2.

strength and a coherent structure that sustains a stable low-pressure region on the wing surface, thereby maximizing lift. The rapid wingbeat frequencies characteristic of insects such as mosquitoes, operating at several hundred hertz, significantly constrain this vortex growth phase.

Vortex dynamics studies reveal that LEVs require a characteristic formation time to reach full development, during which circulation intensifies and the vortex stabilizes to enhance lift effectively. This timescale corresponds to a non-dimensional parameter known as the vortex formation number, generally close to unity when scaled by stroke length and velocity, as reviewed by Dabiri (2009) [12]. For mosquitoes, the optimal vortex growth period often exceeds the available half-stroke duration at their high flapping frequencies. When vortices surpass this formation threshold, they tend to detach or shed, leading to reduced lift and increased drag; similarly, premature detachment due to insufficient maturation also diminishes aerodynamic effectiveness.

Given these temporal constraints, LEVs may contribute only partially to lift generation within each stroke. To compensate, mosquitoes likely rely more heavily on alternative unsteady aerodynamic mechanisms such as wake capture, wherein the wing interacts with vortices shed during the preceding stroke at stroke reversal. These interactions enable partial recovery of energy from the wake vortices, offsetting any lift deficits arising from limited LEV development. This aerodynamic strategy aligns with mosquito flight kinematics, characterized by high wingbeat frequency and narrow stroke amplitude, which restrict the temporal window for LEV formation but facilitate exploitation of wake interactions to sustain flight performance.

This dynamic balance between limited LEV maturation and compensatory wake capture mechanisms highlights the intricate fluid dynamic environment underlying insect flight and underscores the importance of incorporating unsteady aerodynamic modeling beyond the constraints of classical steady-state or quasi-steady approaches [59][33].

Moreover, experimental limitations have historically hindered progress in understanding these phenomena. Measuring forces on small, rapidly moving wings and visualizing high-frequency flow patterns remain challenging. Early models relied on far-field wake analyses rather than direct airflow measurements, limiting their accuracy by failing to capture complex near-field vortex dynamics and transient flow structures crucial for understanding lift generation mechanisms[47][59].

Furthermore, at the low Reynolds numbers typical of insect flight, viscous forces dominate over inertial forces, creating unique flow conditions that differ fundamentally from those in conventional aerodynamics[59]. This viscous dominance promotes the attachment and coherence of leading-edge vortices (LEVs), thereby stabilizing these vortical structures against premature detachment by increasing vorticity diffusion and preventing rapid vortex breakdown or shedding. In this context, "stable" refers to the persistence of a coherent vortex that remains attached and dynamically relevant during substantial portions of the wingbeat cycle, contributing to enhanced lift generation. Additionally, viscous effects modify boundary layer behavior by delaying or suppressing flow separation near the wing's leading edge compared to higher Reynolds number conditions. This alteration shifts transition and detachment points along the wing surface, influencing lift and drag characteristics in ways that differ fundamentally from classical aerodynamics. These fluid dynamic conditions heighten the role of unsteady aerodynamic phenomena and complex fluid-structure interactions, necessitating the application of specialized analytical methods and experimental techniques designed to accurately capture and predict aerodynamic forces within such low Reynolds number, highly unsteady flow regimes.

Wing flexibility further complicates the analysis. Unlike rigid aircraft wings, insect wings deform dynamically under aerodynamic forces. This flexibility enhances lift through additional unsteady effects that traditional theories fail to capture[59]. Computational fluid dynamics (CFD) simulations, such as those shown in Figure 2.3, have advanced understanding of wake dynamics and vortex structures around flapping wings[25]. Engels et al. [25] demonstrated that flexible bumblebee wings generate complex helical vortices, illustrating how wing deformation shapes three-dimensional flow and sustains aerodynamic forces during hovering. These results highlight the significant role of wing flexibility in unsteady aerodynamics and emphasize the limitations of rigid-wing models in capturing insect flight behavior.

Section 2.1.2 discusses, in detail, the major unsteady aerodynamic mechanisms integral to insect flight such as LEV stability, Kramer effects during wing rotations, wing-wake interactions, and added mass effects during acceleration and deceleration. Early quasi-

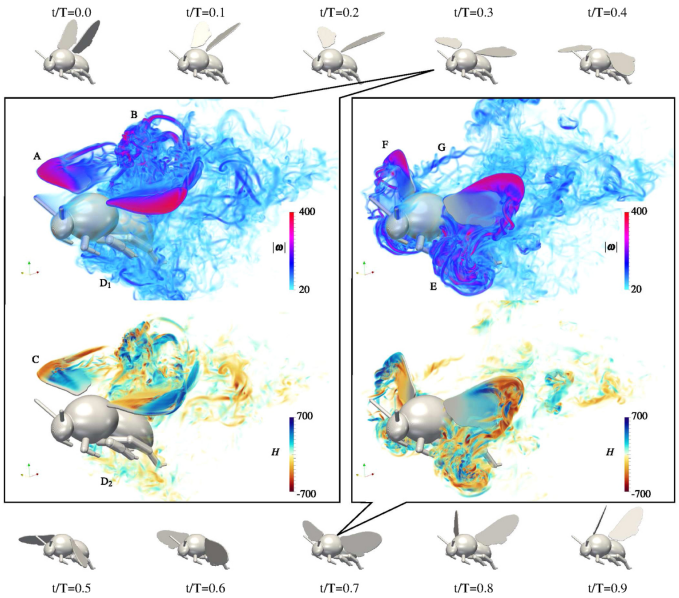

Figure 2.3: Computational fluid dynamics (CFD) simulation of a hovering bumblebee, illustrating wingbeat phases and the resulting wake dynamics through vorticity ($|\omega|$) and helicity (H) visualizations, where helicity quantifies the alignment of rotational motion and flow direction within wake structures, thereby providing insight into the coherence and aerodynamic significance of three-dimensional vortices [25].

steady models failed to account for one or more of these mechanisms or the sustained lift required for hovering flight [47]. Notably, these often over simplified models failed to capture wake capture phenomena, where a wing interacts with the vortices shed during previous strokes. This omission led quasi-steady approaches to underestimate the aerodynamic forces produced by insect wings, especially sustained hovering flight.

Thus, insect flight showcases remarkable adaptability and diversity in lift-generation strategies. And the above insights highlight the limitations of classical aerodynamic theories to explain these strategies, and underscore the need for well designed experiments and refined numerical quasi-steady models to fully understand the unsteady aerodynamics driving their extraordinary capabilities.

2.1.2. UNSTEADY AERODYNAMIC MECHANISMS USED BY INSECTS

EXPERIMENTAL INVESTIGATION OF UNSTEADY MECHANISMS

The advent of experimental studies brought significant breakthroughs in understanding the unsteady mechanisms used by insects. Pioneering research by Weis-Fogh first identified the aerodynamic phenomena responsible for the "missing lift" in insect flight, particularly the "clap and fling" mechanism, observed in tiny insects like Encarsia formosa, which generates high lift without the delay caused by the Wagner effect[42]. Later, Dickinson's experiments using scaled models of Drosophila melanogaster wings flap-

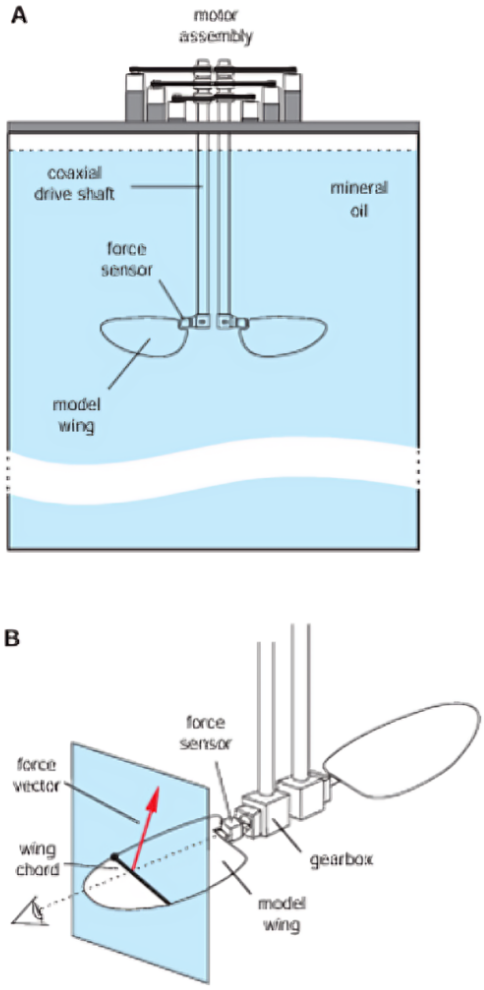

Figure 2.4: (A) The diagram shows a motor-driven experimental setup with model wings submerged in mineral oil, connected via a coaxial drive shaft and equipped with force sensors to measure aerodynamic forces.(B) The schematic illustrates the orientation of the model wing, highlighting the force vector, wing chord, and angle of attack while connected to a gearbox and force sensor for precise measurements [18].

ping in a low-Reynolds-number environment, shown in Figure 2.4, provided deeper insights into the time-dependent aerodynamic forces and flow patterns during various wing kinematics[16]. These studies identified three key contributors to enhanced lift: rotational circulation at the stroke's end, delayed stall resulting from unsteady motion, and wake capture, where wings interact with disturbed airflows from previous strokes[42]. These mechanisms work synergistically to generate the extraordinary aerodynamic performance observed in insects.

DYNAMIC SCALING AND NON-DIMENSIONAL NUMBERS

As shown in Figure 2.4, researchers often rely on mechanical models that replicate insect flight dynamics. A key aspect of these models is ensuring that critical nondimensional parameters - primarily the Reynolds number, Rossby number, and, in forward flight, the Advance Ratio - are matched to those of real insects, an approach known as dynamic scaling. The Reynolds number characterizes the balance of inertial to viscous forces and is crucial for capturing the dominant flow regimes and boundary layer behavior. The Rossby number represents the influence of rotational effects due to finite wing length, affecting spanwise flow and the structure of leading-edge vortices. The Advance Ratio quantifies the ratio of the mean forward velocity to the mean wingtip velocity, governing the relative importance of translational versus flapping kinematics; however, in pure hovering flight, the Advance Ratio approaches zero, rendering its influence negligible in this context. As a result, the Reynolds number emerges as the most significant nondimensional parameter governing the aerodynamic forces and flow structures relevant to flapping-wing models under hovering conditions.

- **Reynolds Number (Re):**

  The Reynolds number characterizes the ratio of inertial to viscous forces in the flow, using a characteristic length (typically the mean chord length, c), a characteristic velocity (commonly the mean wingtip or translational velocity, U), and the kinematic viscosity of the fluid (ν):

$$Re = \frac{Uc}{\nu} \tag{2.1}$$

- **Rossby Number (Ro):**

  The Rossby number quantifies the relative influence of inertial effects to Coriolis (rotational) effects and is often expressed for flapping wings as:

$$Ro = \frac{U}{2\Omega c} \tag{2.2}$$

  or, equivalently for flapping wings with angular velocity Ω:

$$Ro = \frac{R}{c} \tag{2.3}$$

  where:

  - R = wing length (span)
  - c = mean chord length
  - Ω = angular velocity of wing rotation
  - $U = \Omega R$ for circular motion at the wingtip

- **Advance Ratio (J):**

  The Advance Ratio relates the mean forward (translational) velocity of the body (U_{forward}) to the mean wingtip velocity (U_{tip}), and is defined as:

$$J = \frac{U_{\text{forward}}}{2\Phi f R} \tag{2.4}$$

  where:

  - U_{forward} = mean forward flight speed
  - Φ = stroke amplitude in radians
  - f = wingbeat frequency
  - R = wing length (span)

  For hovering ($U_{\text{forward}} \approx 0$), $J \approx 0$.

By correctly matching these parameters, particularly the Reynolds number, scaled robotic or mechanical models preserve the essential fluid dynamic behaviors observed in natural insect flight. This dynamic similarity enables researchers to conduct precise force measurements and flow visualization experiments that would be impractical or impossible with live insects, due to the challenges of measuring tiny, rapidly fluctuating forces and resolving high-frequency flow structures at such small scales. Consequently, dynamically scaled models are invaluable for analyzing a range of complex unsteady aerodynamic phenomena, including the clap-and-fling effect[6][38], delayed stall[24][20][16][17], rotational lift[6][49][48], and wing–wake interactions[17]. The following section delves into these mechanisms in detail:

UNSTEADY MECHANISMS EXPLAINED

Delayed Stall

One of the many unsteady mechanisms that is inherent in insect flight dynamics is the delayed stall [16][38], a phenomenon critical for maintaining lift at high angles of attack. Insects often operate at angles that would cause stall on fixed wings. However, during flapping motion, a leading-edge vortex (LEV) forms above the wing (Figure 2.5), creating a separated flow region that remains attached for a significant portion of the stroke. This region prevents the wing from stalling, allowing for sustained lift generation. Unlike in conventional wings, where the vortex detaches quickly, insect wings benefit from the stabilizing influence of spanwise flows, which induce the three-dimensional transport of vorticity from the wing root toward the tip, effectively advecting and stretching the LEV. This process generates helicity that enhances vortex coherence and limits uncontrolled growth or premature detachment of the LEV, as illustrated in Figure 2.6. Such

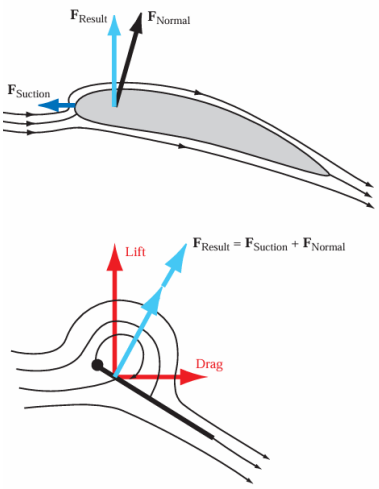

Figure 2.5: The Polhamus' leading edge suction analogy compares flow around a blunt wing, where sharp flow diversion creates a leading-edge suction force, to flow around a thin airfoil with a leading edge vortex, which diverts flow normal to the airfoil surface, enhancing the force perpendicular to the wing section and contributing to delayed stall. [47].

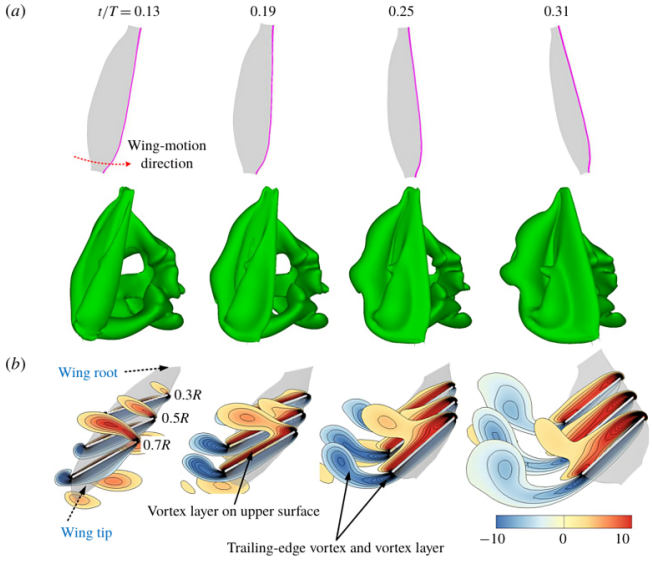

Figure 2.6: The aerodynamic behavior of a flapping wing, with (a) showing iso-vorticity surface plots highlighting trailing-edge vortices during the downstroke and (b) depicting non-dimensional spanwise vorticity contours at different wing sections [33].

stabilization is essential to maintain an attached, low-pressure vortex over the wing during high angle-of-attack phases, enabling insects to achieve high lift forces in oscillatory wing motion. Delayed stall is central to understanding how insects can maintain high lift during slow hovering or rapid manoeuvres without experiencing the catastrophic loss of lift associated with conventional stall.

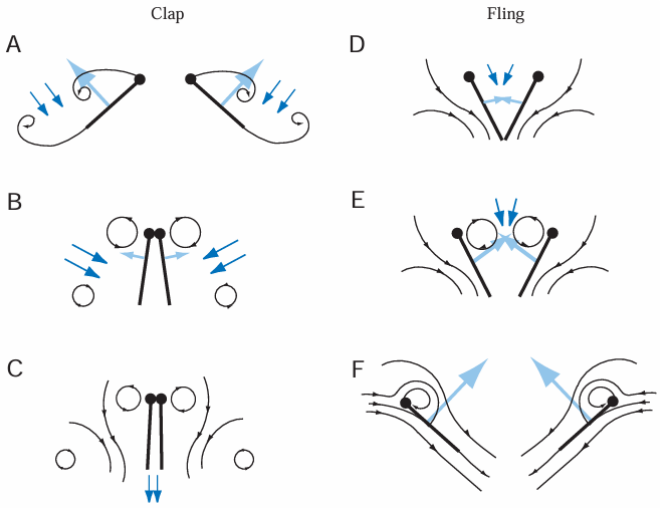

Figure 2.7: The "clap and fling" mechanism in insect flight. During the clap phase (A–C), wings approach dorsally, creating stopping vortices as trailing edges meet, while the closing gap pushes fluid outward, generating additional thrust. In the fling phase (D–F), wings separate by rotating around the trailing edge, allowing fluid to rush into the gap, boosting circulation and forming new leading-edge vortices, while opposite-circulation trailing edge vortices annihilate each other, aiding rapid circulation build-up. [47].

Clap-and-fling mechanism

The clap-and-fling mechanism shown in figure 2.7, observed in smaller insects, involves a coordinated movement of the wings during the transition between strokes[57]. In the clap phase, the wings come together dorsally, eliminating opposing vortices and ensuring rapid circulation buildup for the next stroke. During the fling phase, the wings separate, creating a low-pressure zone that draws in air, further enhancing circulation and lift. While this mechanism provides a notable lift boost, it is not universally used by all insects and often occurs only in species with smaller wing spans or in situations requiring high force production [47]. Despite not being universally employed by all species or in all flight circumstances, clap-and-fling remains a compelling example of how insects exploit unsteady flows to overcome aerodynamic challenges.

Kramer effect

The Kramer effect, also known as rotational lift, plays a significant role during the rapid pronation and supination of insect wings at stroke reversals[6][48]. Fundamentally, this effect is governed by the establishment of circulation around the wing, as described by the Kutta condition[29]. The Kutta condition states that, for an airfoil with a sharp trail-

ing edge, such as in mosquito wings, the flow organizes so that a stagnation region forms at the trailing edge via the generation of circulation[30]. During stroke reversal, when the wing transitions between half-strokes by rotating about its spanwise axis, this rotational motion is superimposed on the translational movement through the stroke plane. In these moments, the usual stagnation point at the trailing edge is displaced onto the upper or lower wing surface, temporarily violating the Kutta condition and resulting in a high local velocity and pressure gradient at the trailing edge.

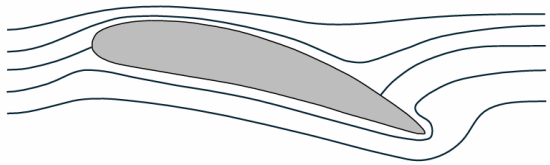

Figure 2.8: Illustration of the streamline pattern around a wing without circulation, showing stagnation points at the leading edge and near the trailing edge on the rear surface [48].

This transient disruption is comparable to a wing at rest that is suddenly accelerated; in both cases, the absence or sudden change of circulation causes the stagnation point to deviate from the trailing edge. As depicted schematically in Figure 2.8, the streamlines around a wing with no initial circulation show a stagnation point on the upper surface near the trailing edge, rather than at the edge itself. As the wing accelerates, a surface-bound circulation rapidly develops, restoring the stagnation point to the trailing edge, in accordance with the Kutta condition. This induced circulation accelerates the flow above the wing and decelerates the flow below, resulting in a pressure differential that produces lift.

In flapping wing kinematics, the rotational movement at pronation and supination shifts the stagnation point away from the trailing edge and re-establishes circulation upon completion of the wing's rotational transition. This process is formalized as 'rotational circulation'[48], and the resulting lift generated during these stroke reversals becomes particularly critical when translational lift is minimal. Modern aerodynamic models incorporate these rotational mechanisms to more accurately predict the complex force production observed in insect flight.

Added mass

Added mass is a significant concept that explains the reactive forces experienced when a wing accelerates through the air [22][49]. As the wing moves, it must displace the surrounding fluid, effectively accelerating a volume of fluid adjacent to it. This interaction manifests as an inertial resistance force mathematically proportional to the wing's acceleration, commonly expressed as:

$$\mathbf{F}_{\text{added mass}} = -m_a \mathbf{a}, \tag{2.5}$$

where m_a is the added mass coefficient reflecting the effective mass of fluid accelerated by the wing, and **a** is the wing's acceleration vector. Although this force is transient and most pronounced during the initial stages of motion or abrupt changes in velocity, added mass plays a critical role in the unsteady aerodynamic loading. Combined with circulatory effects such as the leading-edge vortex and wake interactions, added mass forces contribute fundamentally to the dynamic nature of insect flight.

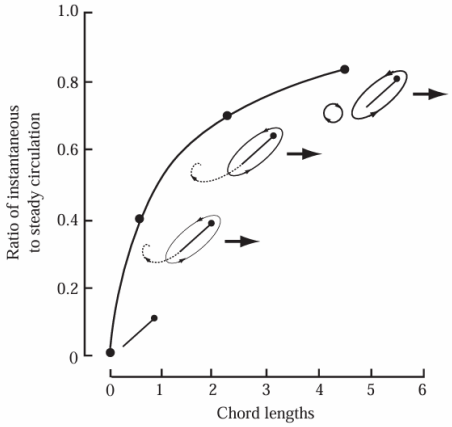

Figure 2.9: The Wagner effect illustrates how the ratio of instantaneous to steady circulation around an airfoil increases as the trailing edge vortex moves away, with bound circulation building up around the wing section as vorticity is shed into the wake, eventually reaching steady-state conditions after several chord lengths of travel [47].

Wagner effect

Another niche unsteady mechanism is the Wagner effect, which highlights the transient nature of lift generation as a wing begins motion. The Wagner effect describes the delay in the buildup of lift when a wing begins motion[55]. When an inclined wing starts moving, the circulation around it does not instantly reach its steady-state value. This delay occurs because vorticity shed from the trailing edge counteracts the growth of bound circulation around the wing. As the shed vorticity moves farther away, the circulation around the wing gradually increases to its maximum value as shown in figure 2.9. This transient behaviour reduces lift at the onset of motion, acting as a damping mechanism [48]. However, recent studies suggest that the Wagner effect has a limited impact at the Reynolds numbers typical of insect flight. Nonetheless, understanding this effect is critical, as it demonstrates how unsteady forces evolve in response to changing wing motion.

Wake capture

Now coming to the case in point, Wake capture is another fascinating mechanism where insect wings interact with the disturbed airflow left behind by previous wing strokes, though whether this truly provides an aerodynamic advantage or not remains unclear[15][16].

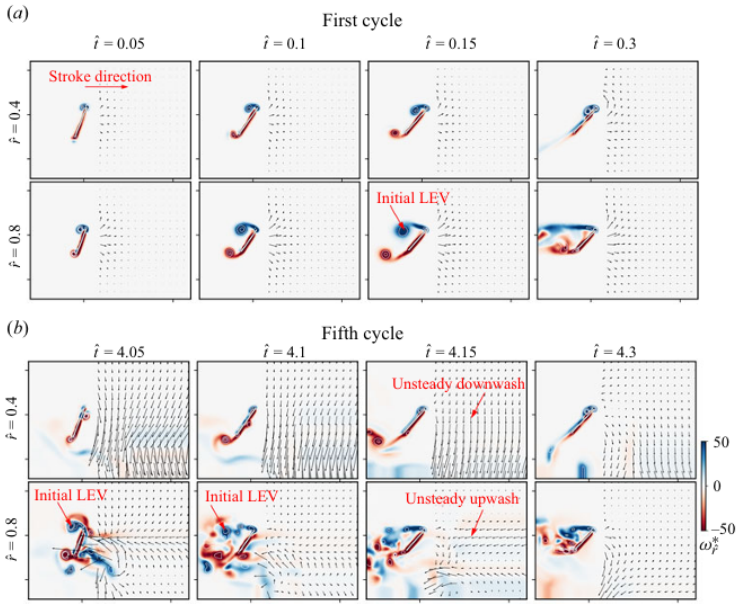

Figure 2.10: Comparison of sectional flow structures and velocity fields from the first and fifth wingbeat cycles at $Re = 10^3$ for representative inboard and outboard wing sections of the wing planform with $AR = 4$ and $\hat{r}_1 = 0.5$. For clarity, flow field velocity vectors are not included beside the wing surface [32].

When a wing reverses direction, it re-enters its own wake, encountering regions of elevated relative velocities and pressure gradients as shown in Figure 2.10. This interaction results in sudden changes in the aerodynamic forces during stroke reversal, potentially allowing insects to recycle energy from the wake that would otherwise dissipate, though the extent of this energy recovery remains under investigation. While this mechanism demonstrates the remarkable ability of insects to exploit unsteady flows, it remains insufficiently studied and poorly understood compared to more established phenomena like delayed stall or leading-edge vortices.

The significance of wake capture becomes particularly evident in insects with unconventional wing kinematics, such as mosquitoes, which operate with small stroke amplitudes and unique wing trajectories[18][53] which would be discussed further in section 2.2.1. Unlike insects with larger stroke amplitudes that primarily rely on leading-edge vortex stability and delayed stall, mosquitoes might encounter stronger wake interaction effects during flight, which they must navigate or potentially exploit to generate sufficient lift for sustained flight [33][7]. Thus, it's important to note that the role of wake capture in mosquito flight is nuanced, with it potentially enhancing performance in some contexts while possibly introducing challenges that must be overcome through compensatory adaptations [7]. This underexplored phenomenon represents an important frontier in unsteady aerodynamics, with potential applications in bio-inspired engineering, particularly in the development of MAVs [58][24][42] as discussed earlier. Understanding wake

capture could provide valuable insights into the evolutionary diversity of flight strategies and reveal how insects adapt to various ecological and biomechanical constraints.

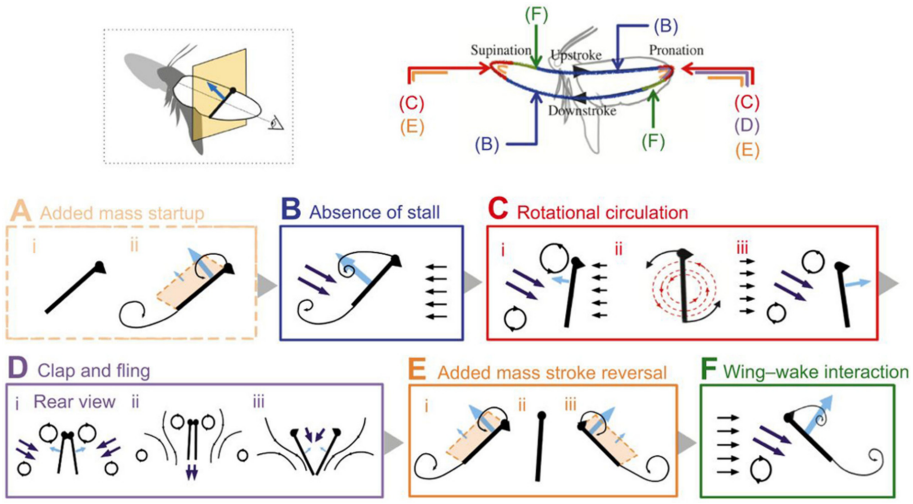

Figure 2.11: The image illustrates the complex aerodynamic mechanisms underlying insect flight, including added mass effects (A, E), stall prevention through leading-edge vortices (B), rotational circulation during wing rotation (C), clap-and-fling mechanism (D), and wing-wake interactions (F), with detailed diagrams explaining the forces and flow dynamics at each stage [10].

Together, these unsteady aerodynamic mechanisms, ranging from the Wagner effect and delayed stall to rotational forces, clap-and-fling, wake capture, and added mass, shown in Figure 2.11, create a comprehensive picture of how insects achieve their extraordinary flight capabilities.

It is however to be noted that not all unsteady aerodynamic mechanisms mentioned above, contribute positively to flight performance, as their effects can vary depending on the specific context of flight. Research has demonstrated that some mechanisms may hinder efficiency by introducing aerodynamic penalties, such as increased drag or energy expenditure, which can impair overall flight dynamics [50]. However, these negative effects are often counteracted by other mechanisms that enhance performance, creating a delicate balance in insect flight. For instance, adaptations like wake capture might play a compensatory role by recovering energy from previously shed vortices, allowing insects to offset the limitations imposed by less efficient mechanisms. The ability to balance these competing effects highlights the sophistication of insect flight mechanics and underscores the importance of understanding how these mechanisms interact to potentially enhance the aerodynamic performance.

2.2. RESEARCH GAP IN MOSQUITO WING KINEMATICS

2.2.1. UNIQUE WING TRAJECTORY AND ITS AERODYNAMIC IMPLICATIONS

Mosquitoes represent a distinctive example of flight mechanics, showcasing unique adaptations that utilize one or more principles of unsteady aerodynamics that were discussed in the previous section. Their flight is characterized by extraordinarily high wingbeat frequencies (up to 800 Hz) and narrow stroke amplitudes (~40 degrees), which contrast sharply with other insects' broader wing motions [33][7]. Through a dynamic interplay of aerodynamic mechanisms, mosquitoes maintain stable hovering flight, operating at Reynolds numbers of approximately 120 [27], calculated using the characteristic wing chord length and the mean wingtip velocity derived from their high-frequency wingbeat kinematics. This Reynolds number is somewhat lower than that of many other Diptera, reflecting their specialized combination of high-frequency wing motion and limited sweep amplitude [33].

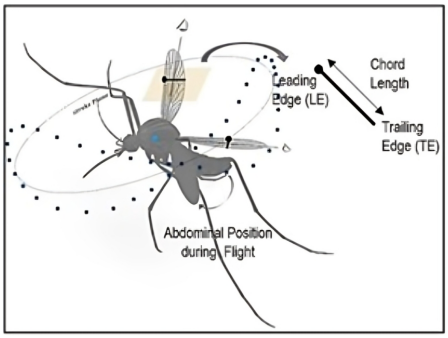

Figure 2.12: The figure-eight-shaped wingtip trajectory of mosquitoes during flight, highlighting key features such as the leading edge (LE), trailing edge (TE), chord length, and abdominal positioning [51].

Perhaps the most distinctive feature of mosquito flight is the figure-eight wing tip trajectory, a complex motion pattern emerging from the interplay of stroking, pitching, and heaving movements [50]. This trajectory, illustrated in Figure 2.12, could be assumed to play a pivotal role in force generation and wing-wake interactions. Unlike the standard wing movements seen in most insects, the figure-eight pattern introduces a vertical component to the wing's motion, generating drag forces during the downstroke and contributing to lift production [27][35].

The influence of this trajectory becomes apparent when considering mosquito-specific parameters: narrow wings characterized by a relatively small chord length and an aspect ratio typically ranging from 4.5 to 5.5, coupled with high flapping frequencies and low Reynolds numbers. The deviation motion within the figure-eight pattern dynamically alters the angle of attack, substantially affecting aerodynamic forces during each stroke phase [54][27]. This mechanism is particularly relevant during stroke reversals, where precise timing facilitates controlled vortex detachment and mitigates the accumulation of vortices that could adversely impact subsequent strokes [36].

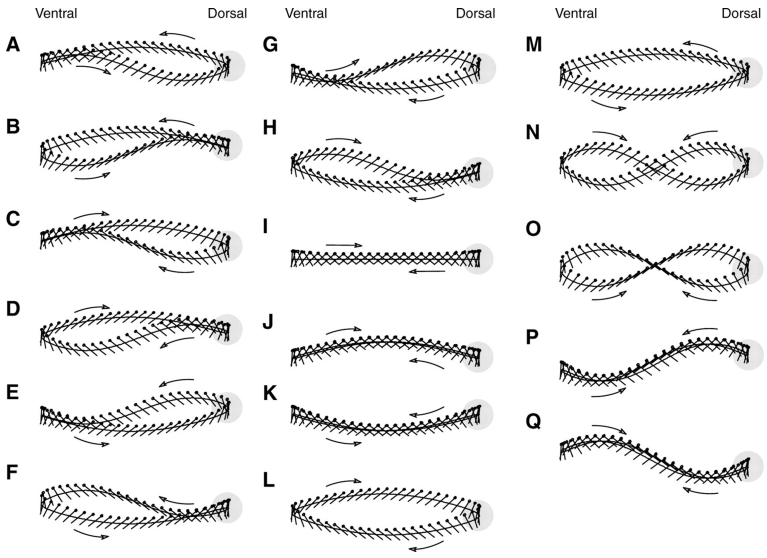

Figure 2.13: Illustration of mosquito wingtip trajectories during various maneuvers, adapted from Lehmann and Pick (2007)[31]. Panels A–F depict ventral and dorsal stroke patterns observed during forward flight; G–L show intermediate or transitional trajectories; M–Q display specialized figure-eight shapes associated with hovering and yaw maneuvers. The panels N and O emphasize figure-eight trajectories, highlighting their proposed role in modulating aerodynamic force production and facilitating wake capture for stable hovering and directional control.

Figure 2.13 further illustrates different variations of wing-tip trajectories which can influence aerodynamic forces. Wing-wake interactions are critical here; as the wings trace their path, they encounter wake structures from previous strokes, and depending on the kind of trajectory they follow, the aerodynamics forces would vary [31]. These interactions can enhance or diminish force production depending on the trajectory's timing and spatial orientation [11][36]. We could hypothesize that the manipulation of these wake dynamics illustrates mosquitoes' evolutionary adaptation for achieving stable flight despite their constrained wing kinematics.

The figure-eight motion also demands higher mechanical power due to its constrained sweep amplitude but compensates by maximizing vertical force through effective utilization of drag forces [35]. Although not yet fully quantified or explored qualitatively, numerical simulations suggest that this figure-eight trajectory substantially influences aerodynamic force production and flight efficiency at small sweep amplitudes and within specific Reynolds number ranges, consistent with mosquito flight characteristics [11][36]. Figure 2.14 demonstrates how variations in stroke angle, deviation angle, and pitch angle influence the trajectory across different phases of the flapping cycle.

While significant strides have been made in understanding the figure-eight wing tip trajectory of mosquitoes, several critical aspects remain unexplored. Current research has primarily focused on documenting and analysing existing figure-eight patterns, but

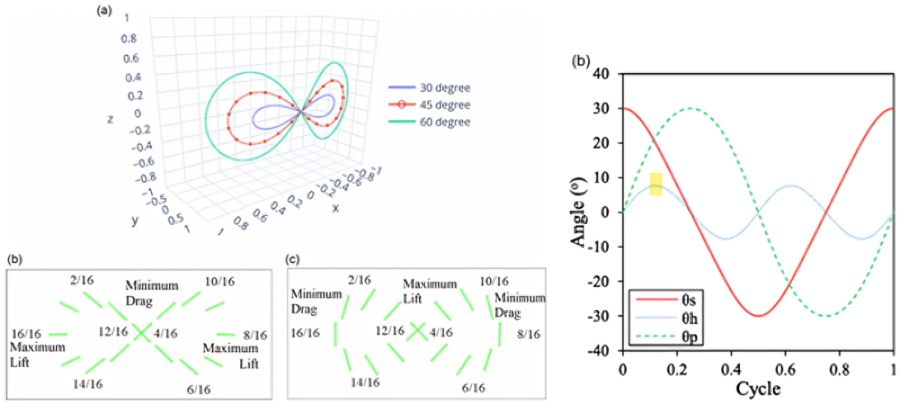

Figure 2.14: The wingtip trajectories and Euler angles for mosquito wing motion, showing (a) figure-eight-shaped trajectories at different input link angles (30°, 45°, 60°) and (b) the variation of stroke angle, deviation angle, and pitch angle over a flapping cycle[11].

there's limited understanding of how variations in the trajectory's shape, timing, and spatial orientation might affect wake interaction forces, and thus presents a compelling avenue for future research.

While the figure-eight trajectory involves multiple variables that could affect aerodynamic performance, we focus specifically on the deviation angle as a starting point to understand its isolated effect on wing-wake interaction forces. A change in the deviation angle would fundamentally modify the figure-8 shape's height, subsequently influencing the dynamic angle of attack and how the wing interacts with wake structures. Rather than seeking an optimal configuration, our aim is to characterize how changes in this particular parameter influence the complex fluid dynamics and the aerodynamic forces and moments during hovering, specifically the interaction between the wing and previously shed vortices.

2.3. QUASI-STEADY AERODYNAMIC MODELS FOR FLAPPING WING ANALYSIS

Quasi-steady aerodynamic models have long been used as simplified yet effective frameworks for estimating the unsteady forces generated during insect-like flapping wing motion. Unlike fully unsteady computational methods that require intensive calculations to resolve the time-dependent behaviour of the surrounding airflow, the quasi-steady model simplifies the problem by assuming that, at each instant in time, the forces acting on the wing are equivalent to those that would be produced if the wing were moving steadily at that same configuration. In practice, this means that the continuous, complex motion of the wing is broken down into a series of discrete time steps or "snapshots". At each of these moments, although the wing may be accelerating, the model computes the forces based on the instantaneous kinematic state, such as position, velocity and angular acceleration, as if the wing were moving, at that moment, in a steady flow with those

properties, and then advances to the next step. By repeating this process throughout the entire flapping cycle, the quasi-steady model builds up a time-resolved picture of the aerodynamic forces without ever needing to simulate the full, unsteady flow field or track the evolution of vortices and wakes in the fluid.

The formulation typically involves decomposing the total aerodynamic force into several additive components: translational forces arising from wing motion through the fluid, rotational forces due to angular pitching, added mass forces representing the inertia of the fluid displaced by the wing's acceleration, and, in more refined models, nonlinear coupling terms between rotation and translation. The detailed implementation of these force components is explained in section 4.4. Each of these components is modeled using empirically derived force coefficients, often obtained from experiments or high-fidelity CFD simulations. As demonstrated by Wang et al [56], recent refinements to quasi-steady formulations also improve their physical consistency and adaptability to non-sinusoidal kinematics, making them highly useful for predicting force trends over a wide range of flapping trajectories.

One of the main advantages of quasi-steady modeling lies in its computational efficiency and physical interpretability. In contrast to fully unsteady CFD simulations - which are computationally expensive, sensitive to boundary conditions, and require fine spatiotemporal resolution - quasi-steady models allow for rapid evaluation of aerodynamic loads using only the time series of wing kinematics. This makes them particularly attractive for parametric studies, control design, and embedded use in optimization frameworks. Moreover, their analytical structure offers clear insight into how specific motion components contribute to net force production.

However, despite these benefits, quasi-steady models are fundamentally limited by their neglect of flow history and wake effects, as well as their simplified treatment of viscous stresses. Typically, QS models emphasize pressure-driven forces and parameterize viscous effects implicitly within empirical force coefficients, but they do not explicitly resolve the spatially and temporally varying viscous shear stresses that can play a non-negligible role at the low Reynolds numbers characteristic of insect flight. This limitation means that viscous drag contributions, boundary layer dynamics, and near-wing shear effects may be underrepresented or oversimplified. Accurately capturing these viscous phenomena generally requires high-fidelity, time-resolved computational or experimental analyses.

A particular shortcoming of QS models is their inability to account for wake capture [56]. Wake capture, as explained previously, is governed by the interaction of the incoming flow field, shaped by previous wing motion, with the newly initiated stroke. Since quasi-steady models compute forces based solely on instantaneous kinematics, they cannot account for such time-history-dependent phenomena. This limitation is especially pertinent for insects such as *Aedes Aegypti*, which exhibit highly curved figure-eight trajectories with significant stroke-to-stroke wake interaction.

Consequently, while quasi-steady models accurately capture the dominant pressure-driven components of flapping wing aerodynamics - such as translation, rotation, and added mass - they are hypothesized to systematically underestimate total force during stroke reversals, where wake capture is substantial, and potentially underrepresent viscous contributions. In the present study, this limitation is exploited as a methodological advantage: by subtracting the quasi-steady predicted forces from the experimentally measured ones, the residual force can be interpreted as the unmodeled contribution due to wake capture effects, as explained in section 4.2. This approach enables direct, quantitative investigation of how wake interaction mechanisms, particularly as modulated by wing deviation angle, influence net aerodynamic force generation.

3

Research Question

Despite significant advances in understanding insect aerodynamics, there remains a notable gap in knowledge regarding the specific role of deviation angle (heaving motion) in influencing wing–wake interaction forces during hovering flight. Prior studies have primarily concentrated on other kinematic parameters, such as stroke amplitude and angle of attack, while deviation motion has often been treated as secondary or insignificant for aerodynamic performance in many insects[19][15]. This oversight is particularly relevant given that certain insects, most notably mosquitoes, exhibit a unique combination of relatively small stroke amplitudes and comparatively large deviation angles. These characteristics are hypothesized to enhance the exploitation of unsteady wing–wake interaction mechanisms.

Recognizing the importance of this deviation angle, this study focuses on an abstracted insect-like flapping wing kinematics incorporating features typical of insect wing beating. The parameter ranges are informed by mosquito flight as a biologically relevant model organism, selected for its pronounced deviation motion, its hypothesized utility in highlighting the aerodynamic role of this kinematic variable, and its societal importance as a disease vector. These insights may also inform optimization of wing kinematics and control strategies in flapping-wing micro aerial vehicles (FWMAVs), possibly enhancing their aerodynamic performance during hovering and maneuvering.

Thus, the present study investigates, analyzes, and quantifies how variation in deviation angle (heaving motion) of an abstracted insect-like, figure-of-eight, wing-tip trajectory, representative of general insect flapping kinematics during hovering, influences aerodynamic wing–wake interaction forces.

4

METHODOLOGY

OVERVIEW OF METHODOLOGY

To address the role of deviation angle in modulating wake capture forces during hovering flapping flight, this study employs a comprehensive framework combining hydrodynamic force measurements from a dynamically scaled experiment and comparative numerical modeling based on quasi-steady (QS) aerodynamic theory.

The foundation of this approach lies in a specific limitation of quasi-steady models - the inability to account for wake capture forces, as discussed in section 2.3. Conversely, the experimental measurements inherently capture these wake capture forces, as the physical wing interacts fully with the generated flow structures during flapping motion. Thus, by subtracting the quasi-steady predicted forces from these experimentally obtained hydrodynamic forces, the residual force can be interpreted as the unmodeled contribution arising predominantly from wake capture.

The process begins with the execution of prescribed wing kinematics using a robotic manipulator, followed by the collection of time-resolved force data across different configurations. Subsequently, the net hydrodynamic force acting solely on the wing is isolated through a series of wet and dry runs. Finally, by comparing these measured forces with those predicted by the quasi-steady aerodynamic model, the residual component, specifically the wake capture, is extracted. This integrated approach enables a direct, quantitative assessment of wake capture forces and their variation with deviation angle.

The following sections outline comprehensively, the experimental apparatus, the setting up of the experiments and the quasi-steady model, as well as the assumptions and approximations employed in this study to address the research objectives.

4.1. EXPERIMENTAL APPARATUS

The physical implementation of this experimental process relies on three core components: the Stäubli TX2-140 industrial robot, which executes the prescribed wing kinematics with high repeatability; a custom-built wing assembly mounted to the robot interface; and a water tank that serves as the test medium for generating fully submerged flows. Together, these elements form the basis of the experimental setup used to generate and quantify the wake capture forces relevant at different prescribed deviation angles.

4.1.1. STAUBLI ROBOT TX2-140

This experimental study is conducted using the Stäubli TX2-140 robot shown in figure 4.1a, a high-precision, six-degree-of-freedom industrial manipulator at the TU Delft Laboratory for Aero and Hydrodynamics. This robot features a sophisticated structure consisting of interconnected links: the base, shoulder, inner link, elbow, forearm, and wrist, as shown in figure 4.1b.

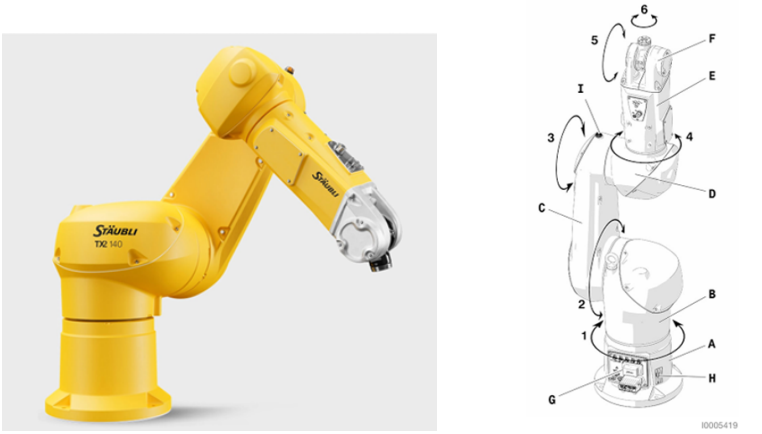

(a) Stäubli TX2-140 industrial robot (b) Configuration of Stäubli Joints

Figure 4.1: The Stäubli TX2-140 industrial robot and its Joint Configurations [45]

COORDINATE SYSTEMS AND CONTROL

The TX2-140 operates with multiple coordinate systems, as shown in Figure 4.2, that facilitate accurate and repeatable positioning and motion control. The primary reference frames include the World Coordinate System, which is fixed at the robot's base and provides a stable global reference frame regardless of arm position. This coordinate system serves as the foundation for all robot movements and remains constant throughout operations. The Flange Coordinate System is attached to the robot's tool flange and moves with the arm to track end-effector position and orientation, providing a reference frame that follows the tool's perspective. This multi-frame structure enables the robot to execute kinematic trajectories with high precision, characterized by a positional repeatabil-

ity typically on the order of ±0.02 mm [45], ensuring that the prescribed wing motions are consistently reproducible throughout the experiments.

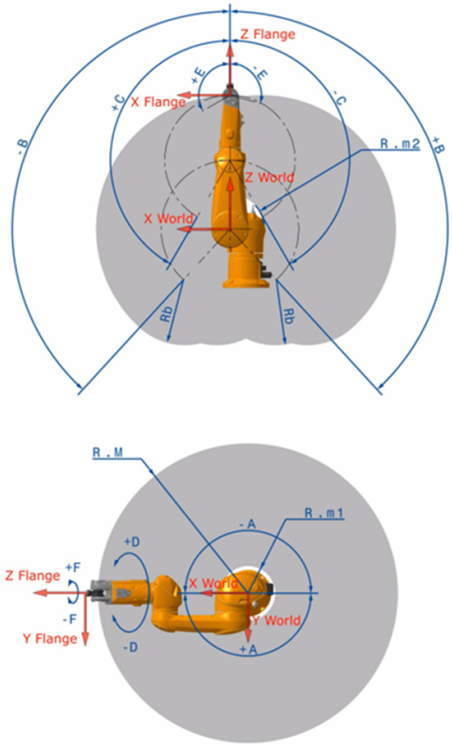

Figure 4.2: World and Flange Coordinate Systems on Stäubli TX2-140 [45]

Additionally, the robot supports a Tool Coordinate System that is user-definable at arbitrary points, allowing custom kinematics definitions for specific experimental setups. This flexibility enables me to define the robot's kinematics with respect to an arbitrary frame position instead of using the World or Flange coordinates, which can be advantageous in my experimental scenarios. These coordinate systems also enable programming complex trajectories and transformations between different reference frames, essential for sophisticated experimental protocols.

FORCE-TORQUE SENSING CAPABILITIES

The TX2-140 robot is equipped with an BOTA Systems (LaxONE-Ethercat version) force-torque sensor mounted directly at the robot flange. This sensor provides six-axis measurements - three orthogonal forces and three moments - relative to the flange coordinate system, facilitating comprehensive real-time monitoring of aerodynamic loads

during wing flapping experiments. The sensor features force measurement range of approximately 1800 N and torque measurement ranges up to approximately 60 Nm, with resolutions on the order of 0.075 millinewtons for force and 0.003 millinewton-meters for torque components. Its high sampling frequency capability, here set at 250 Hz, allows effective capture of the dynamic force variations during the experiment.

However, limitations include relatively high signal noise and resolution constraints at very low force levels, as well as mechanical coupling effects that may require careful calibration and filtering to ensure accurate separation of aerodynamic forces from structural vibrations or inertial loads of the robotic arm (explained in Appendix A.6). Despite these constraints, the integrated force-torque sensing system provides robust and precise measurement essential for quantitative force analysis and dynamic control in this experimental investigation.

OPERATIONAL MODES OF STÄUBLI ROBOTS

Stäubli industrial robots operate through several distinct control modes that enable both manual manipulation and automated execution of programmed tasks. These operational modes provide different levels of control over the robot's motion, from direct joint manipulation to sophisticated programmed sequences.

The JOG mode represents a fundamental manual control interface that enables precise positioning and direct manipulation of the robot arm. This mode is primarily accessed through the SP2 teach pendant, which serves as the primary human-machine interface for direct robot control. In JOG mode, operators can control the robot's position through multiple coordinate systems, each offering distinct advantages for different positioning tasks. It allows individual manipulation of each robot axis (J1 through J6) independently, providing direct control over the robot's mechanical configuration.

VAL 3 is Stäubli's proprietary programming language designed specifically for robot control. It enables the creation of sophisticated motion sequences and complex automation routines that can be stored in the controller's memory and executed on demand. Structured Programming in VAL 3 supports modern programming constructs including variables, conditional statements, loops, and functions, enabling the development of complex applications with sophisticated decision-making capabilities. Motion Programming allows programmers to define precise movements using various motion types: point-to-point movements (movej) for joint-space trajectories, linear movements (movel) for straight-line paths, circular movements (movec) for arc trajectories, and spline movements for smooth, continuous multi-point paths. This variety of motion types enables the creation of complex trajectories. Programs created in VAL 3 can be developed using the Stäubli Robotics Suite (SRS) software on a PC, which provides a comprehensive development environment including simulation capabilities. During program execution, the robot automatically follows the defined trajectories with precise control of position, velocity, and acceleration profiles.

4.1.2. WING ASSEMBLY

This experiment uses a wing assembly fixed on the robot arm to perform the required kinematics. While the initial plan involved laser-cutting a dynamically scaled mosquito wing profile from stainless steel to faithfully replicate the morphological characteristics of *Aedes Aegypti* (figure 4.3) (explained further in section 5.3), the final experimental configuration utilized a simplified rectangular stainless steel plate, as shown in figure 4.4 and 4.5. The rectangular plate, originally employed during intermediate water trials to validate system performance and force measurement protocols, was repurposed in the final testing phase to simplify the aerodynamic analysis. This provisional wing, measuring 240 mm in length, 60 mm in width, and 4 mm in thickness, maintained identical mounting geometry to the final design, utilizing the same shaft interface and fastening methodology illustrated in figure 4.4 and 4.6. This change represents a notable approximation, while offering some key advantages, both of which are explained in detail in section 5.3.

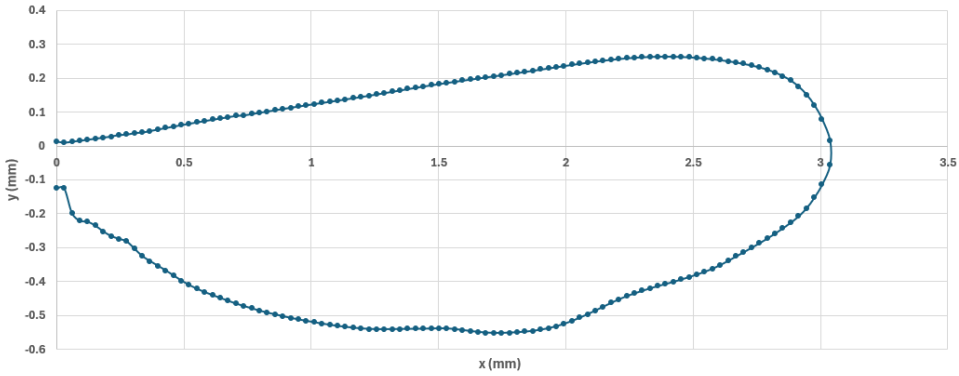

Figure 4.3: Aedes aegypti mosquito wing profile sourced from Prof. Dr. A. J. L. L. Buchner, who measured it by imaging Aedes mosquito wings under a microscope (12 males and 12 females) and using edge detection method to determine the outline and thereafter scaling and averaging the profile. The profile was then reconstructed by mapping the scaled wing geometry based on the extracted dataset. This was later abstracted to a simple rectangular profile due to reason explained in section 5.3

Note that the experimental protocol requires the wing model to be submerged in a liquid medium with precisely controlled viscosity to achieve the target Reynolds number matching that of a hovering mosquito. This immersion presents significant technical challenges that necessitated careful design considerations for the mounting system. Primary among these considerations is the risk of the robot arm coming into contact with the viscous liquid medium. Such contact would create substantial flow disturbances that could compromise the validity of experimental measurements by introducing artificial flow patterns and turbulence not present in the biological system being modelled. More critically, exposure of the robot arm to the liquid medium poses significant risks to the robotic system itself. The Stäubli TX2-140 robot, while robust, is not designed for liquid immersion, and contact with the experimental fluid could potentially damage electrical components, compromise seals, and introduce corrosion to precision mechanical ele-

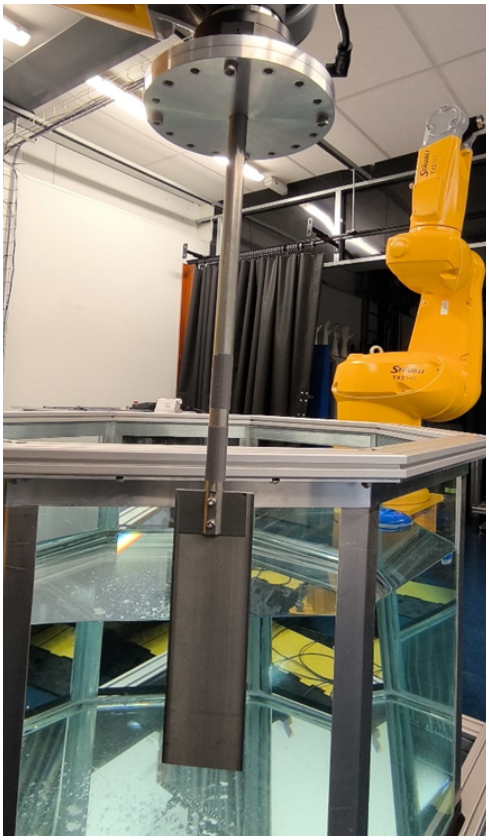

Figure 4.4: Rectangular Stainless Steel Wing Assembly attached to the Staubli Flange.

Figure 4.5: The disassembled rectangular wing.

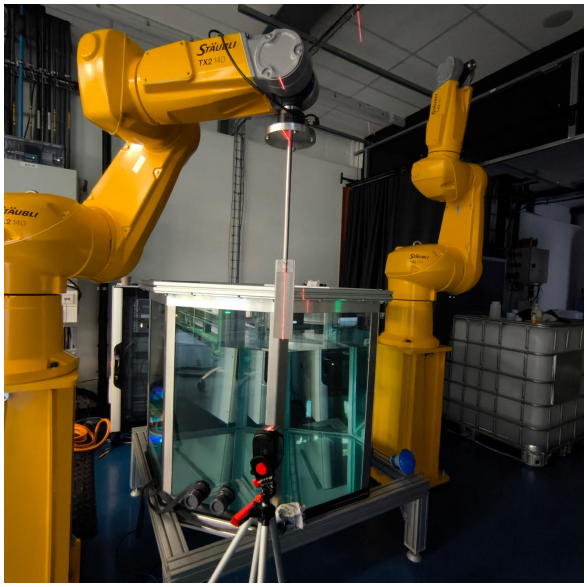

Figure 4.6: The figure illustrates how the stainless steel rectangular wing was precisely aligned with the axis of the robot flange using a laser alignment setup.

ments.

To address these challenges, the wing assembly incorporates a specialized mounting solution featuring a slender yet structurally rigid metal shaft, as shown in figure 4.7. This shaft serves as an extension arm that maintains a safe separation distance between the robot flange and the liquid surface while also minimizing flow disturbance in the experimental medium.

Thus, the wing base is securely attached to this cylindrical shaft measuring 400 mm in length and 15 mm in diameter. This connection is achieved using a pair of bolts and a metallic bushing, which serves to minimize play and vibrations during operation (explained in A.6.1 and A.6.2), thereby enhancing the stability and accuracy of the experimental setup. The free end of the shaft is connected to a disk, which is then bolted onto the robot flange using an additional set of bolts, as shown in figure 4.8. This robust assembly ensures a rigid and reliable interface between the wing model and the robot arm, facilitating precise control and repeatability in experimental conditions.

4.1.3. TANK

The experiment, as mentioned above involves submerging the wing assembly in a fluid mixture, contained inside an octagonal-shaped top-open tank, shown in figure 4.9, constructed from transparent plexiglass to enable optical access for flow visualization and measurement techniques in the later stages of this experimental pursuit. Each side of the octagonal tank measures 500 mm in length with a total height of 900 mm, providing suf-

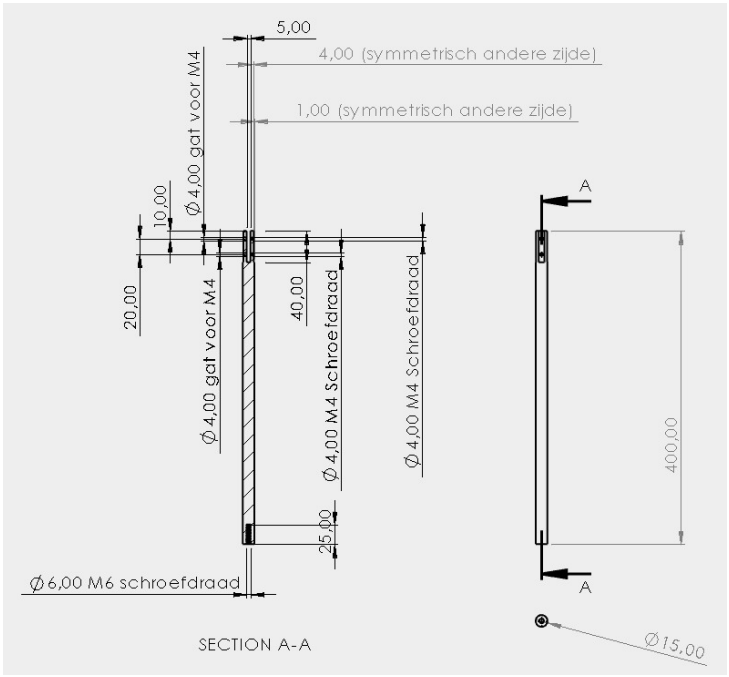

Figure 4.7: Dimensions of the Shaft that connects the Wing to the Robot Flange. All units in mm. (Drawing by Dirk De Boer)

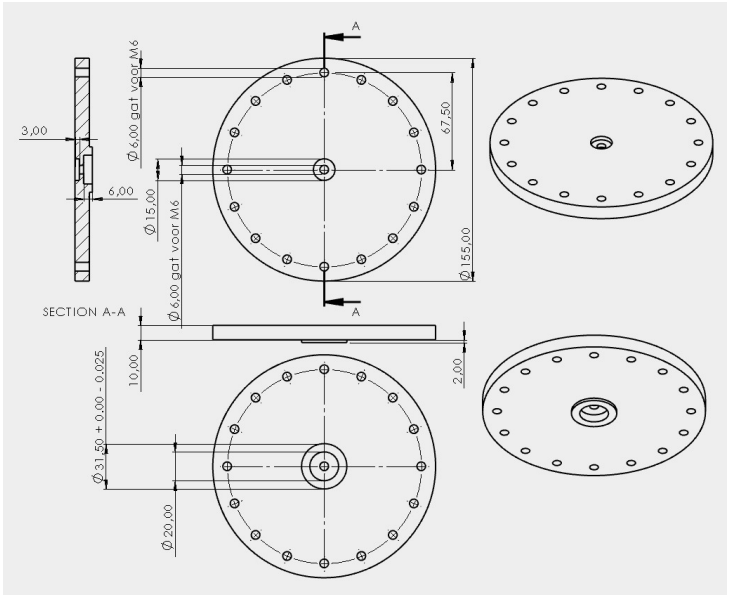

Figure 4.8: Dimensions of the Robot Flange that connects the Wing-shaft assembly to the robot arm. All units in mm. (Drawing by Dirk De Boer)

ficient volume to accommodate the wing flapping motion while minimizing wall effects, such as flow confinement, blockage, and boundary layer development along the tank walls, that can alter the velocity field around the wing and introduce spurious pressure gradients, thereby affecting the fidelity of aerodynamic force measurements [49][46].

The octagonal geometry further reduces flow recirculation and corner vortices often observed in rectangular tanks, contributing to a more uniform and quasi-infinite fluid environment [26]. This design choice is grounded in classical fluid dynamic principles of flow confinement, which indicate that to limit wall-induced interference, the minimum distance between the model and the nearest boundary should exceed several characteristic length scales of the flow structures generated - in this case, at least three to five times the wing chord length [43]. Given the wing chord length scale in the present study, the tank dimensions satisfy these criteria, thus reducing blockage effects and ensuring negligible influence of viscous boundary layers from the tank walls on the near-field vortex dynamics.

While direct experimental validation of wall effects, such as velocity profile measurements or force comparisons across tank sizes, was not explicitly conducted here, widely accepted scaling laws and previous investigations on flapping wing models in similarly sized tanks affirm the adequacy of these dimensions for approximating unbounded fluid conditions [16][18].

Figure 4.9: Tank configuration

The tank assembly is mounted on a custom-fabricated metallic support frame with a height of 420 mm, which provides adequate clearance beneath the tank for the installa-

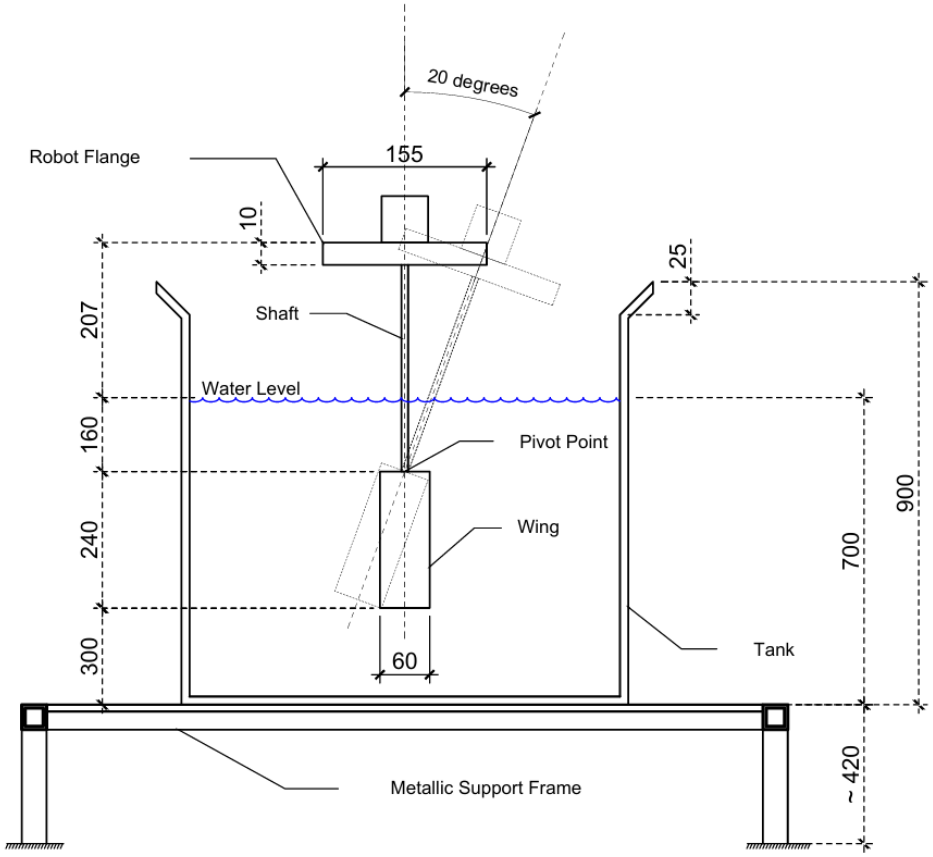

Figure 4.10: Schematic of the overall wing assembly configuration submerged within the octagonal tank. All dimensions are given in millimeters (mm). The figure illustrates the wing-shaft assembly attached to the robot flange, with the tank measuring 900 mm in height and a fluid level maintained at 700 mm. The tank is supported by a 420 mm high metallic frame, providing adequate clearance for the installation of Particle Image Velocimetry (PIV) equipment and associated optical components required for flow field measurements in future experimental phases. The wing, 60 mm in width and 240 mm in length, executes figure-eight trajectories about a static pivot point located 160 mm below the fluid surface.

tion of Particle Image Velocimetry (PIV) equipment and associated optical components required for flow field measurements in subsequent experimental phases. During experimental operations, the tank was planned to be filled with a fluid mixture to a height of approximately 700 mm, leaving sufficient freeboard to prevent spillage during wing flapping operations while ensuring complete submersion of the wing model. The shaft-wing assembly is positioned such that a precisely calculated portion of the 400 mm shaft extends above the fluid surface, maintaining the robot flange at a safe distance from the liquid medium. This overall configuration, shown in figure 4.10 ensures that the robot components remain completely isolated from the experimental fluid while allowing the wing to operate within the required fluid environment.

4.2. PROCESS FLOW FOR WAKE CAPTURE FORCE COMPUTATION

The methodology employed for the computation of wake capture forces integrates experimental measurements, systematic post-processing routines, and quasi-steady aerodynamic modeling, as schematically represented in the process flow diagram (see Figure 4.11). In the experimental phase, the Stäubli robot is programmed to execute prescribed wing kinematics corresponding to a series of deviation angles, specifically ranging from 0° to 6° in increments of 0.5°. Additionally, an outlier case at 7.5° is included as an addition. For each deviation angle, force data are collected under four distinct configurations: (i) in air with the wing attached, (ii) in air without the wing, (iii) in water with the wing attached, and (iv) in water without the wing.

For each of these configurations, five independent trials are conducted at every deviation angle. During each trial, the wing undergoes five consecutive cycles of the figure-eight flapping motion, with each cycle having a period of 2.6 seconds. This time period was identified as an optimal balance between minimizing velocity-induced instabilities and maintaining motion stability, as detailed in Appendix A.4.2. At the beginning of each trial, the wing assembly is positioned outside the fluid. The robot then gradually submerges the assembly into the fluid over a period of approximately 10 seconds. Upon full immersion, the wing remains stationary in the fluid for an additional one minute. This interval is critical, as it allows any disturbances introduced during submersion to dissipate, thereby ensuring the fluid is quiescent prior to the initiation of the flapping cycles.

Following this settling period, the prescribed five cycles of the figure-eight motion are performed, lasting approximately 15 seconds in total. Upon completion of the cycles, the wing is withdrawn from the fluid and repositioned at the initial starting location. Subsequently, the assembly is allowed to rest for approximately two minutes prior to the commencement of the next trial. This rest period allows any residual motion in the fluid to subside and enables draining of any fluid adhering to the wing assembly, thereby promoting experimental repeatability and minimizing potential sources of error associated with mass loading due to adhering fluid.

During the experiments, the sensor exhibited noticeable drift (~0.1N) over time (explained in Appendix B.2), resulting in a bias in the absolute force measurements. To address this issue, 5 seconds of static offset forces were recorded both before and after each

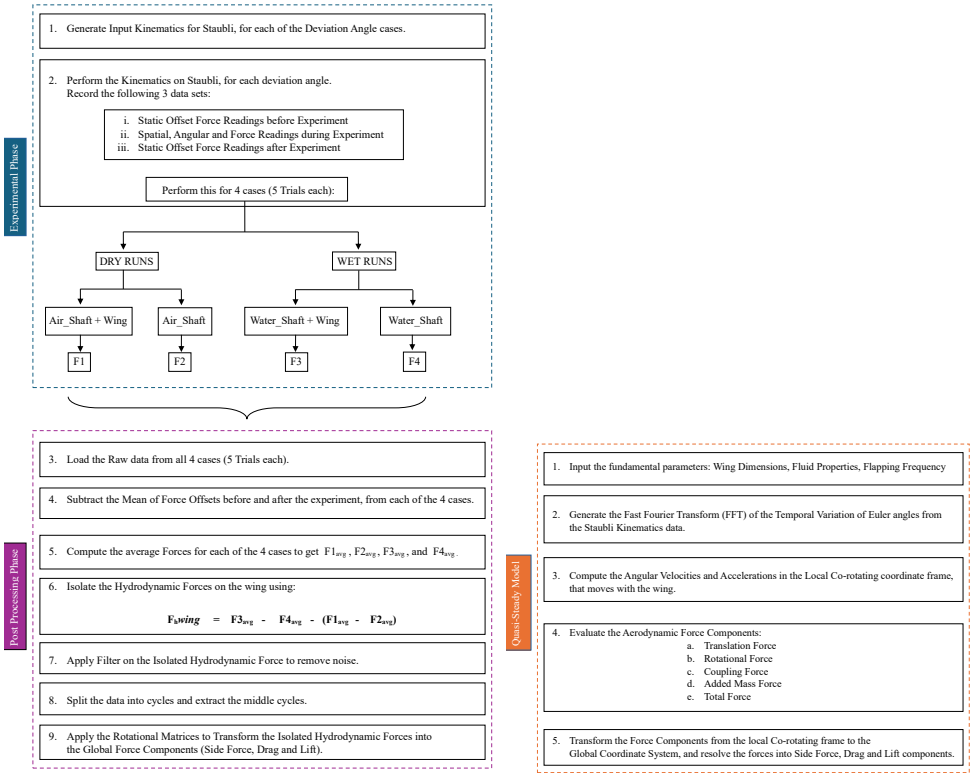

(a) Experimental Work flow

(b) Quasi-steady model work flow

(c) Last step to isolate the wake capture forces

Figure 4.11: Overview of the Process Flow for Wake Capture Computation.

run, and the average of the two readings was subtracted from the force measurements, enabling correction for temporal drift or bias. Additionally, the purpose of performing multiple trials was to ensure the repeatability and reliability of the corrected measurements.

Once the raw data is acquired, the post-processing phase involves correcting the time-resolved force signals by subtracting the corresponding mean of offsets before and after each experiment, followed by averaging across trials. The net hydrodynamic force acting solely on the wing is then isolated by removing contributions from the shaft and air cases.

The raw force data acquired from the Staubli robot contains significant noise, making direct interpretation challenging. To address this, a combination of technical and practical filtering strategies was employed, as detailed in Section 4.3.3. Thus, to extract clean periodic signals, the force data is filtered, and the middle flapping cycles are isolated to avoid edge transients. The resulting force signal is transformed into a global coordinate frame using rotational matrices, yielding time-resolved side force, lift, and drag components.

Parallel to this, the quasi-steady model reconstructs the expected aerodynamic forces based on the same input kinematics. Using Fourier-transformed Euler angles, the model computes angular velocities and accelerations in the local co-rotating frame and evaluates all relevant force components - translational, rotational, nonlinear coupling, and added mass. These are resolved into the global reference frame to match the format of the experimental data.

The final wake capture force is obtained by subtracting the quasi-steady prediction from the experimental force. This residual reflects the unsteady aerodynamic contribution, primarily associated with wake capture, that is not captured by quasi-steady assumptions.

4.3. SETTING UP THE EXPERIMENT

4.3.1. COORDINATE SYSTEM AND EULER ANGLES

The experimental setup employs two distinct coordinate systems as defined in the Stäubli robot architecture: the World coordinate system and the Flange coordinate system. Since the wing assembly is directly attached to the robot flange, the wing motion and the corresponding forces acting on the wing are defined with respect to the flange coordinate system, which is also referred to as the wing coordinate system in this experimental context. The angular orientation of the wing is defined using three Euler angles - Sweep(ϕ), Deviation(θ), and Pitch(α) - which are established with respect to the World coordinate system.

For the left wing of a mosquito, as represented in image 4.12, these Euler angles are defined with specific conventions. Sweep represents rotation about the Z axis in the horizontal plane, with forward motion (toward the head) considered positive. Deviation indicates rotation about the X axis in the vertical plane along the body of the mosquito,

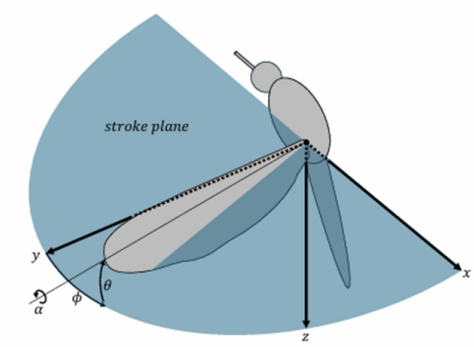

Figure 4.12: Schematic illustrating the definition of three Euler angles - Sweep (ϕ), Deviation (θ), and Pitch — used to describe the orientation of the left wing of a mosquito relative to a fixed (x, y, z) coordinate system. The x-axis denotes the anteroposterior axis of the mosquito's body (running head-to-abdomen), the y-axis points laterally (outward from the midline towards the left wing base), and the z-axis is oriented dorsoventrally (vertical in the body frame). The schematic depicts the mosquito's thorax and the root of the left wing attached at the wing base. The shaded region represents the wing's stroke plane, swept predominantly by rotation about the z-axis (sweep angle ϕ). The deviation angle (θ) represents out-of-plane angular displacement about the body x-axis, while the pitch angle (α) is defined as rotation of the wing about its own spanwise y-axis. In this convention, $\alpha = 0°$ occurs when the wing's chord lies perpendicular to the incoming flow, with positive values indicating nose-up pitch (leading edge raised), typically encountered at the two extreme points of the figure-eight trajectory at stroke reversal (supination and pronation). The illustrated framework provides the basis for reconstructing three-dimensional wing kinematics and force evaluation in subsequent analysis [4].

with downward motion away from the horizontal plane considered positive. Pitch denotes rotation about the Y axis in the vertical plane perpendicular to the body of the mosquito, with rotation forward toward the head considered positive. These coordinate systems and the corresponding Euler angles provide a comprehensive framework for describing the complex three-dimensional motion of the wing during flapping. Through the simultaneous variation of these three Euler angles with time, the complete wing kinematics of mosquito flight can be accurately represented.

4.3.2. KINEMATICS IMPLEMENTATION

ACTUAL MOSQUITO KINEMATICS

The wing kinematic data utilized in the present study were obtained through high-resolution motion capture and advanced computational analysis performed by Prof. Dr. A. J. L. L. Buchner. The methodology involved tracking and analysing the wing motion and associated kinematics of adult *Aedes Aegypti* mosquitoes during free flight under controlled laboratory conditions. Precise trajectories of the wingtip and body were reconstructed from synchronized multi-camera recordings using machine learning-based pose estimation algorithms, as shown in figure 4.13. These algorithms enabled the three-dimensional extraction of key morphological markers, allowing for the reconstruction of wingbeat kinematics with high temporal fidelity. From the resulting datasets, the time-resolved evolution of the three primary Euler angles - sweep, deviation, and pitch - that characterize the wing's orientation relative to the body was derived. The resulting empirical profiles served as the reference kinematics for the present experimental and modeling

investigations, ensuring biological realism and direct relevance to real mosquito hovering flight.

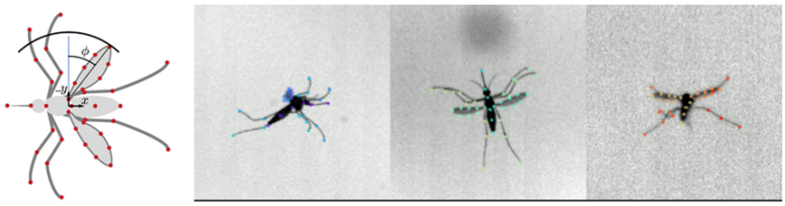

(a) Schematic drawing (b) Stitched triplet recording

Figure 4.13: Wing and body tracking of *Aedes Aegypti* mosquitoes performed using Resnet-50 model of the DeepLabCut (DLC v.2.3.0) package, which is a neural network-based transfer learning framework [37, 4].

The analysis of this data revealed that the variation of the Euler angles, particularly the sweep and deviation angles, follows near-sinusoidal trends, as shown in figure 4.14. The pitch angle also exhibits quasi-sinusoidal motion, though not as pronounced as the other two angles. For experimental convenience and to facilitate parametric studies, Fourier transforms were applied to extract dominant harmonics and convert the actual mosquito wing kinematics into sinusoidal approximations, as explained in section 5.2. This simplification allows for better control of the kinematic parameters and enables systematic investigation of the effects of variations in these parameters on flight performance and aerodynamic forces.

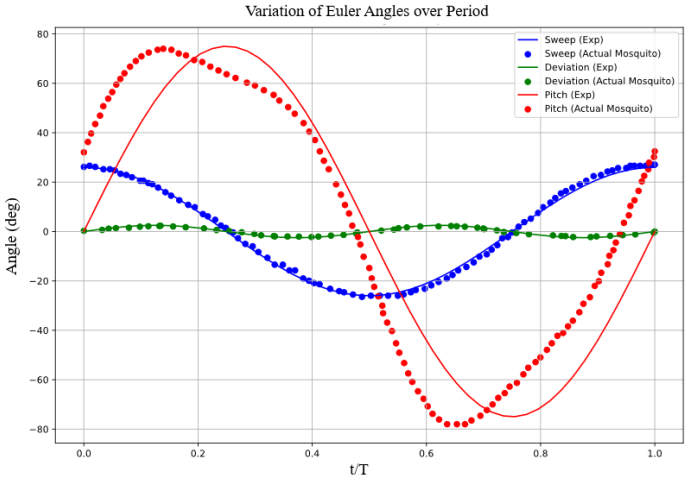

Figure 4.14: Variation of the actual euler angles in a real mosquito versus the sinusoidal approximation of euler angles. Explained further in section 5.2.

IMPLEMENTING THE KINEMATICS ON THE ROBOT

After securing the wing-shaft assembly to the robot flange, the desired wing kinematics can be achieved by precisely controlling the motion of the robot flange. A critical consideration in this implementation is that the experimental focus lies on the motion of the wing rather than the shaft. The point of attachment between the wing and the shaft is analogous to the shoulder joint of the insect wing. This point serves as a pivot that remains stationary in space while the wing and shaft move around it. Consequently, the motion of the robot flange must be defined such that this shoulder point maintains its static position while the wing executes the prescribed kinematic pattern. The execution of this requirement is explained in detail in Appendix A.1.

Given the known dimensions of the wing and shaft, combined with the temporal variation of the Euler angles, trigonometric relationships can be employed to define the trajectory of the robot flange that ensures the wing tip follows the required kinematics while maintaining the stationary position of the shoulder point. In the experimental setup, the shoulder point is designated as the origin (also referred to as the Frame coordinates), and the spatial positions and orientations of the robot flange are calculated relative to this origin.

To input this kinematics into the Stäubli robot system, the required motion of the flange must be represented in terms of spatial positions (X, Y, and Z coordinates), angular orientations (the Euler angles), and velocities. These parameters serve as inputs to the VAL3 program of the Stäubli robot, which executes the prescribed motion.

For this thesis research, a dedicated Python program was developed to define the three Euler angles as sinusoidal functions with controllable amplitudes and periods. This program converts these angular functions into the required coordinates for the robot flange, based on the dimensions of the wing and shaft, which are defined as variables within the program. The program allows for discretization of the motion into a user-specified number of points. Based on this discretization, it computes the velocity values necessary for the robot to transition between consecutive points such that it completes the required cycle at the specified frequency.

The program also generates a three-dimensional simulation of the motion of the wing assembly and robot flange, clearly visualizing the trajectories of both the wing tip and the flange as shown in figure 4.15. This simulation capability enables verification of the intended motion before implementation on the physical robot. Upon confirmation of the desired motion, the program outputs a text file that defines the spatial and angular positions of the flange, along with the velocities, in the VAL3 format compatible with the robot's control system.

Once the required input kinematics are defined in VAL3, the Stäubli software provides a three-dimensional simulator that executes the code and generates a real-time visualization of the robot motion as shown in figure 4.16. This simulation serves as an additional verification step before implementing the motion on the physical robot.

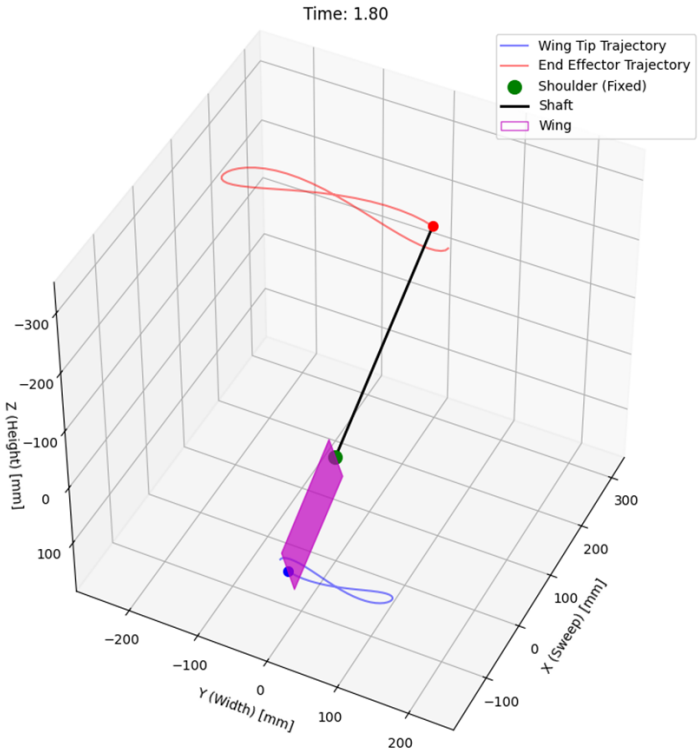

Figure 4.15: 3D simulation of the motion of the wing assembly and robot flange, clearly visualizing the trajectories of both the wing tip (Blue Point) and the flange/end effector (Red Point). The green point here represents the point of attachment between the wing and the shaft is analogous to the shoulder joint of the insect wing. This point serves as a pivot that remains stationary in space while the wing and shaft move around it. This simulation capability, developed in Python, enables verification of the intended motion before implementation on the physical robot

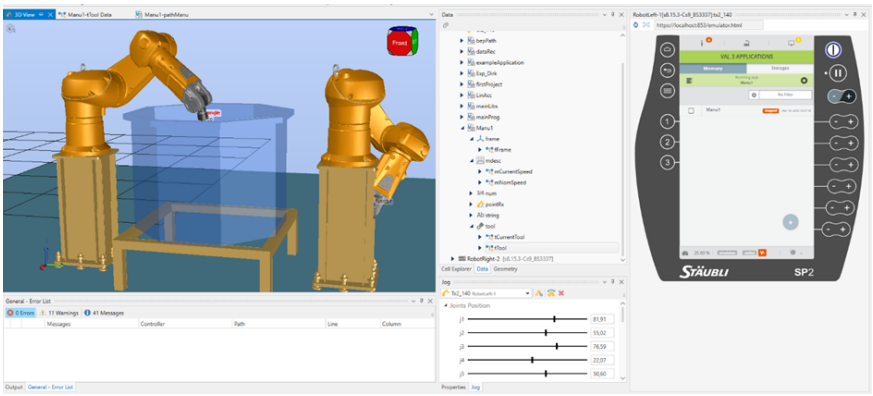

Figure 4.16: 3D real-time visualization of the robot motion, provided by the Staubli Software. This simulation serves as an additional verification step before implementing the motion on the physical robot.

As a precautionary measure prior to simulation, safety boundaries are established around the robot arm, within the software. If the robot exceeds these spatial safety limits during operation, the program automatically terminates execution. This safety feature is designed to prevent accidents during the experiment. During the VAL3 simulation, the program ensures that the robot remains within these predefined safety boundaries at all times.

After the motion has been validated through software simulation and meets the experimental requirements, it is uploaded to the main server or memory of the robot control system for physical implementation. The program is configured to execute five complete cycles of the prescribed motion. During these cycles, the robot records both its own motion parameters and the force-torque data acting on the flange, which can subsequently be exported as a text file for analysis.

4.3.3. STAUBLI OUTPUT AND DATA PROCESSING

The Staubli robotic system generates output text files containing time-resolved kinematic and dynamic data recorded during flapping trials. Each output file encapsulates five consecutive flapping cycles, capturing spatial coordinates (X, Y, Z), Euler angles (sweep Φ, deviation Θ, pitch α), velocities, forces (Fx, Fy, Fz), and torques (Tx, Ty, Tz) at the robot flange - the interface between the robotic arm and wing mount. Critically, force and torque measurements are recorded in the co-rotating wing coordinate system, reflecting loads directly experienced by the wing structure.

A custom Python post-processing program, developed during this thesis, systematically analyses this data. The program first segments the five-cycle dataset into individual cycles, isolating the middle cycle for detailed analysis. This middle cycles are prioritized as it represents steady-state motion, free from transient effects inherent in the initial startup and final deceleration cycles. Cycle segmentation enables comparative studies

across trials and ensures consistency in evaluating force profiles under repeatable kinematic conditions.

TRAJECTORY COMPLIANCE AND FINETUNING

The program then performs kinematic validation by overlaying the recorded Euler angles, spatial trajectories, and velocities against the input reference kinematics. In figure 4.17, the side-by-side comparison quantifies deviations between the middle cycles through metrics like root mean square (RMS) error, for each of the deviation angle cases. Spatial data discrepancies, such as the one shown in figure 4.18 are analysed to see how much the robot trajectory varies from the prescribed input motion.

To further validate the accuracy and repeatability of the robotic execution across the range of deviation angle cases, an uncertainty analysis was conducted, as shown in figures 4.19, 4.20, and 4.21. This analysis commenced by superimposing the normalized temporal profiles of the Euler angles to visually assess variations in the implemented kinematics. Subsequently, a quantitative evaluation was performed by computing the root mean square (RMS) uncertainty matrix, capturing the inter-trial variability among the individual deviation cases for each of the three Euler angles (sweep, deviation, and pitch). The results demonstrated negligible variation in the sweep and pitch angles across the different cases, while the deviation angle exhibited only minimal uncertainty as seen in figure 4.20, with a maximum RMS deviation of 0.13 degrees, well within acceptable limits for experimental precision. Collectively, these findings confirm that the robotic system successfully implemented the prescribed kinematics with a high degree of fidelity and repeatability across all tested deviation angles. The detailed explanation of the iteration performed to finetune the kinematics on the Robot given in Appendix sections A.2, A.3, and A.4.

For force isolation, the program leverages the differential fluid density between air and water. Aerodynamic forces from air trials are subtracted from hydrodynamic forces measured in water, isolating the net hydrodynamic contribution. This subtraction accounts for inertial and frictional loads common to both media, which are attributable to the wing's mass and robotic system dynamics rather than fluid interaction. The resulting hydrodynamic forces, particularly the wing-normal component (Fx), are retained in the co-rotating frame for direct comparison with quasi-steady model predictions. This approach, explained in detailed in the upcoming subsection, preserves the force vector orientation relative to the wing's instantaneous motion, avoiding ambiguities introduced by global coordinate transformations.

HYDRODYNAMIC AND INERTIAL FORCE ISOLATION METHODOLOGY

The wing assembly, comprising both the wing model and supporting shaft, experiences coupled hydrodynamic and inertial effects during flapping motion. However, this investigation focuses exclusively on isolating the hydrodynamic forces acting on the wing itself, requiring systematic separation from inertial forces and hydrodynamic interactions generated by the shaft.

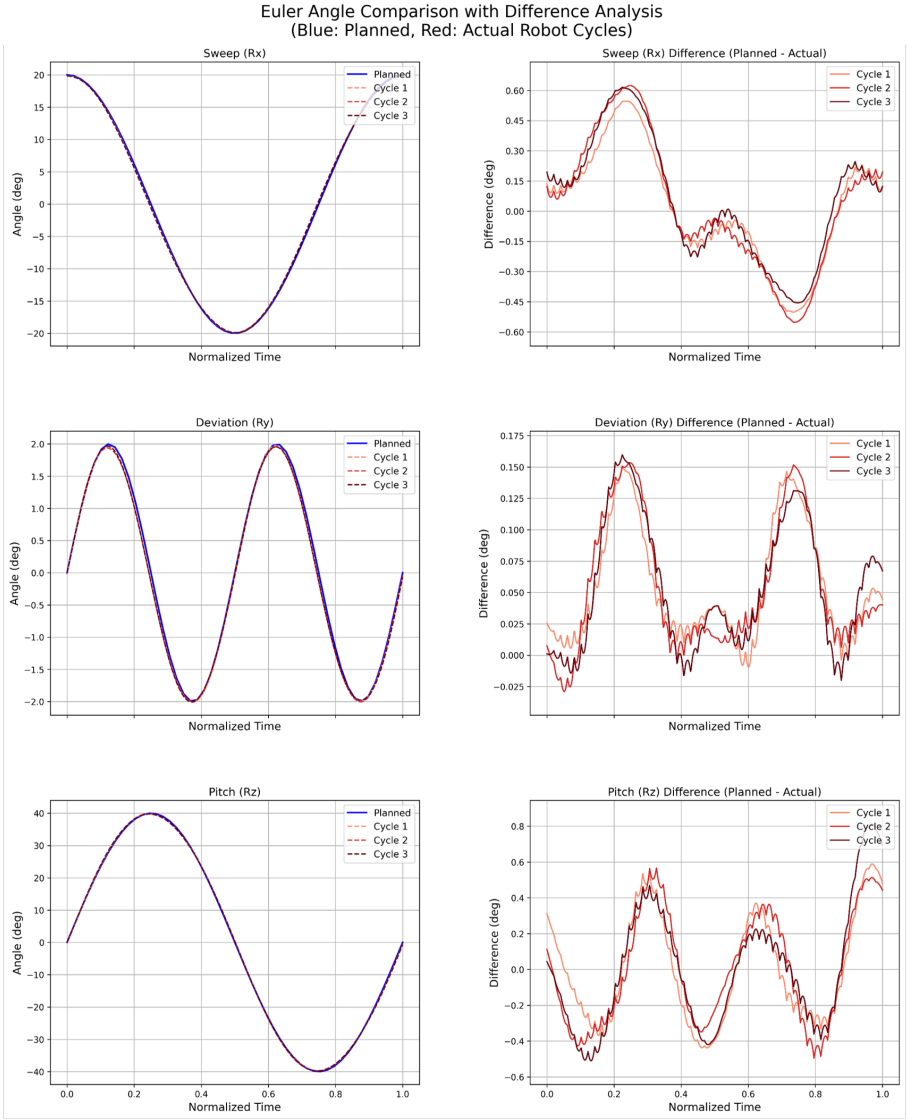

Cycle	Sweep RMS	Deviation RMS	Pitch RMS
1	0.28°	0.07°	0.30°
2	0.33°	0.08°	0.31°
3	0.31°	0.08°	0.34°

Figure 4.17: Figure showing the variation of each of the Euler angles actually executed by the Staubli, compared against the planned input motion. This enhanced Euler analysis gives a clear quantitative idea of how the actual kinematics executed by the Staubli deviate from the input kinematics. The case shown corresponds to a deviation angle of 2.5°.

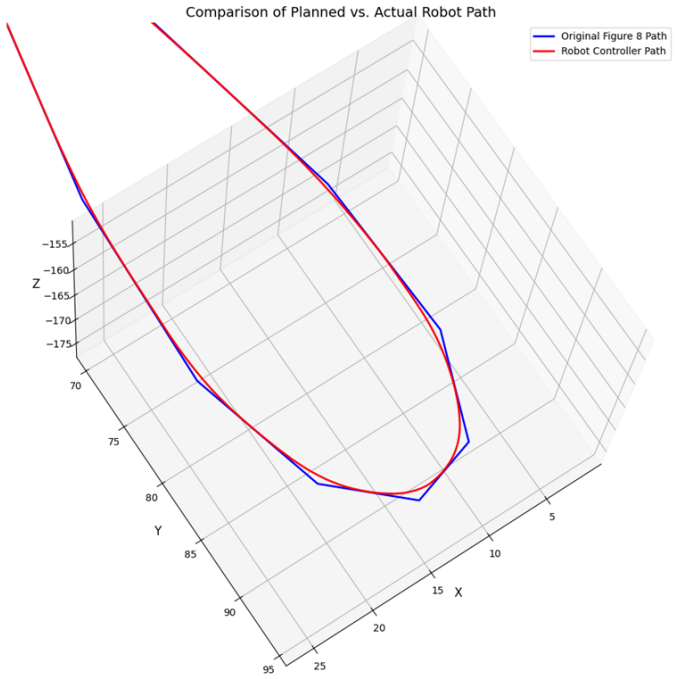

Figure 4.18: Spatial Trajectory Conformance Image, that shows the path actually followed by the Staubli, overlayed against the input trajectory. The conformity between the actual and input motion is a function of the Leave, Reach and number of data points prescribed in the robot input. This analsis gives a visual confirmation of the level of confirmtity, between the ideal and actual trajectories. A more quantitative analysis of this confirmity was already obtained from the enhanced euler analysis shown in figure 4.17. Detailed explanation of the finetuning of Leave, Reach and number of data points parameters is given in Appendix A.2, A.3 and A.4.

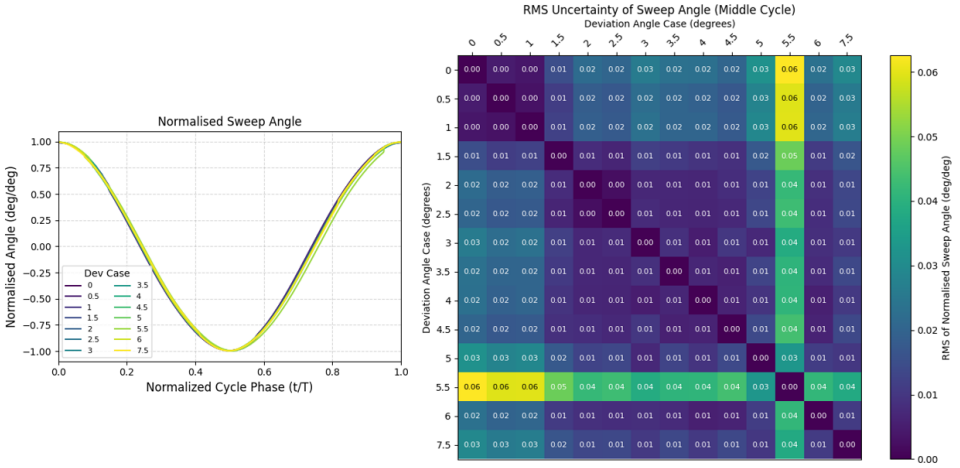

Figure 4.19: Comparison of normalised sweep angle profiles (left) and the RMS uncertainty of the normalised sweep angle (right) at mid-flapping cycle, across a range of deviation angle cases. The left plot shows the repeatability of the prescribed sweep kinematics for different deviation angles, with only minimal deviations between cases. The right heatmap quantifies the RMS error in the normalised sweep angle for each pair of deviation cases, confirming low kinematic uncertainty throughout the experimental parameter space.

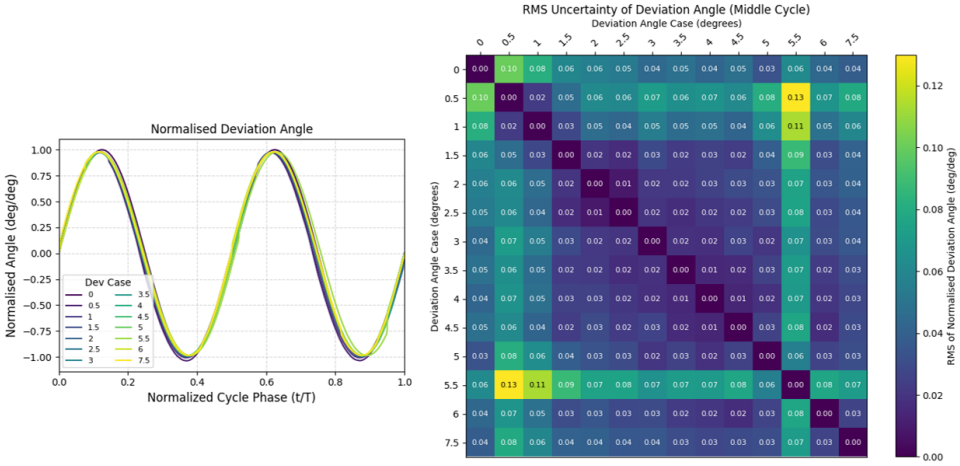

Figure 4.20: Comparison of normalised deviation angle profiles (left) and the RMS uncertainty of the normalised deviation angle (right) at mid-flapping cycle, across a range of deviation angle cases. The left plot shows the repeatability of the prescribed deviation kinematics for different deviation angles, with only minimal deviations between cases. The right heatmap quantifies the RMS error in the normalised deviation angle for each pair of deviation cases, confirming low kinematic uncertainty throughout the experimental parameter space.

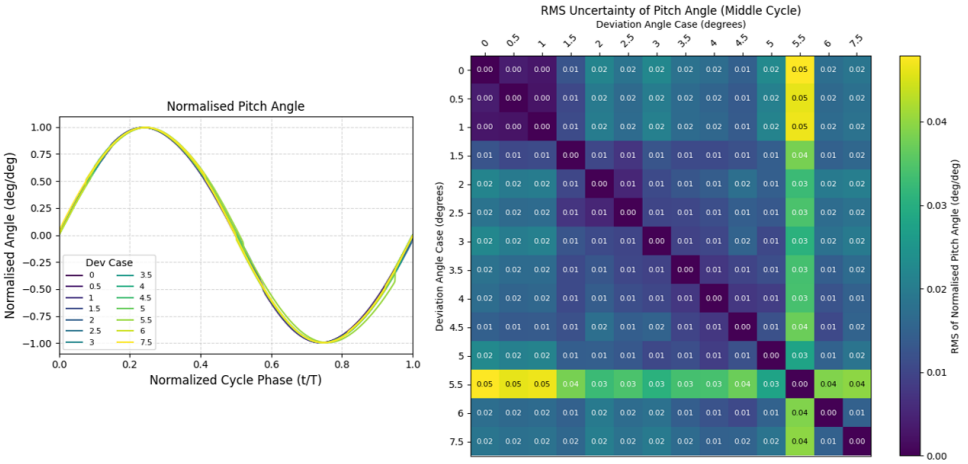

Figure 4.21: Comparison of normalised pitch angle profiles (left) and the RMS uncertainty of the normalised pitch angle (right) at mid-flapping cycle, across a range of deviation angle cases. The left plot shows the repeatability of the prescribed pitch kinematics for different deviation angles, with only minimal deviations between cases. The right heatmap quantifies the RMS error in the normalised pitch angle for each pair of deviation cases, confirming low kinematic uncertainty throughout the experimental parameter space.

A two-phase experimental protocol was implemented, consisting of dry (in-air) and wet (submerged) configurations.

Dry Run: In the dry experiments, the wing-shaft assembly is rigidly fixed while the robot executes the programmed kinematics in air. The measured forces (denoted as F_1) represent the combined inertial contributions of the wing and shaft:

$$F_1 = F_{\text{air, wing}} + F_{\text{air, shaft}} = F_i w + F_i s$$

where $F_i w$ and $F_i s$ are the inertial forces of the wing and shaft, respectively. A subsequent dry run removes the wing, leaving only the shaft attached. The measured forces (F_2) now represent the inertial effects of the shaft alone:

$$F_2 = F_i s$$

Wet Run: In the submerged configuration, the experiment is repeated in the water-glycerol mixture with the full wing-shaft assembly. The measured forces (F_3) include both hydrodynamic and inertial components:

$$F_3 = F_h w + F_h s + F_i w + F_i s$$

where $F_h w$ and $F_h s$ represent the hydrodynamic forces on the wing and shaft. A final

submerged run removes the wing, measuring forces (F_4) attributable to the shaft's hydrodynamic and inertial effects:

$$F_4 = F_h s + F_i s$$

Thus, the wing's hydrodynamic forces are isolated by subtracting confounding factors through the following relationship:

$$F_h w = F_3 - F_4 - (F_1 - F_2)$$

This equation systematically eliminates:
1. Shaft inertial forces ($F_i s$) via $F_1 - F_2$
2. Shaft hydrodynamic forces ($F_h s$) via $F_3 - F_4$
3. Wing inertial forces ($F_i w$) through differential cancellation

FORCE TRANSFORMATION FROM WING COORDINATES TO GLOBAL COORDINATES

Once the isolated normal forces are computed in the wing coordinate system, the transformation to global coordinates requires a sophisticated application of sequential rotation matrices that accurately represent the wing's spatial orientation at each instant during the flapping cycle. This transformation process employs three fundamental rotation matrices corresponding to the wing's sweeping, heaving, and pitching motions, which are mathematically represented by the matrices R_ϕ, R_θ, and R_η respectively. The sweeping rotation matrix R_ϕ accounts for the primary back-and-forth motion of the wing in the horizontal plane, effectively rotating the coordinate system about the vertical axis. This is followed by the heaving rotation matrix R_θ, which captures the vertical deviations of the wing from the primary stroke plane by rotating about the intermediate horizontal axis. Finally, the pitching rotation matrix R_η adjusts for the wing's angle of attack by rotating about the wing's own spanwise axis, which is critical for determining the instantaneous orientation of the wing's chord line relative to the incoming airflow.

The transformation process requires attention to the order of matrix multiplication, as rotation matrices are non-commutative, meaning that the sequence in which they are applied fundamentally affects the final result. The composite transformation matrix is formed by the sequential multiplication $R_\phi * R_\theta * R_\eta$, where each matrix operates on the coordinate system established by the previous rotation, as shown in the Appendix code A.1. The normal force vector, initially expressed in the wing's local coordinate system where it acts perpendicular to the wing surface, is then multiplied by this composite transformation matrix to project it onto the global coordinate axes.

The resulting transformed force vector is subsequently decomposed into three biologically and aerodynamically meaningful components within the global reference frame. The side force component represents lateral forces that would cause the insect to accelerate sideways, perpendicular to both its forward motion and the gravitational field. The drag force component captures the horizontal resistance opposing the insect's forward motion, directly relevant to thrust requirements and energy expenditure during flight.

Most critically, the lift force component represents the vertical force that counteracts the insect's weight, enabling sustained flight and altitude control. This careful decomposition is essential because each force component has distinct implications for flight dynamics and control, with lift being paramount for weight support, drag determining propulsive efficiency, and side forces affecting lateral stability and manoeuvrability. The transformation must account for the precise definition of both the wing coordinate system, where forces are initially calculated based on local flow conditions and wing geometry, and the global coordinate system, which is typically aligned with the insect's body axes or gravitational field, ensuring that the resulting force components can be directly interpreted in the context of flight mechanics and compared with experimental measurements.

SENSOR NOISE AND FILTER SETTINGS

A key issue in the above stage was that the force-torque sensor exhibited significant levels of high-frequency noise, which persisted through the data processing pipeline and affected the accuracy of the transformed force measurements. To ensure that the final force data used for analysis were both clean and physically meaningful, it was necessary to implement an effective noise filtering strategy.

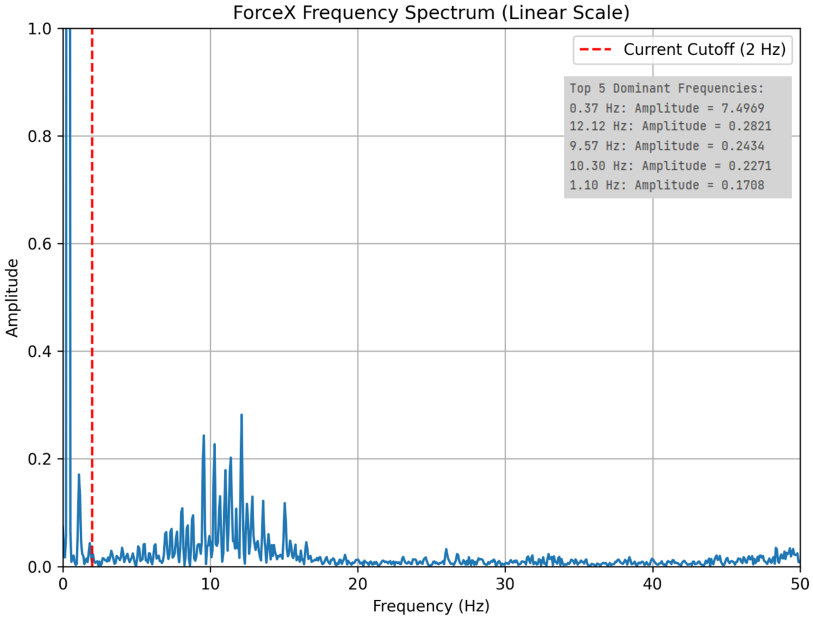

Figure 4.22: Results from the FFT Analysis performed on the raw sensor signal. The Image shows that all the dominant frequencies lie below 2Hz, and hence a cut off frequency of 2Hz would successfully remove the signal noise/vibration issues. The analysis also identified the top 5 dominant frequencies in the signal.

A systematic approach was adopted, beginning with the application of a Fast Fourier Transform (FFT) to the raw sensor signal. Prior to performing the FFT, the mean of the

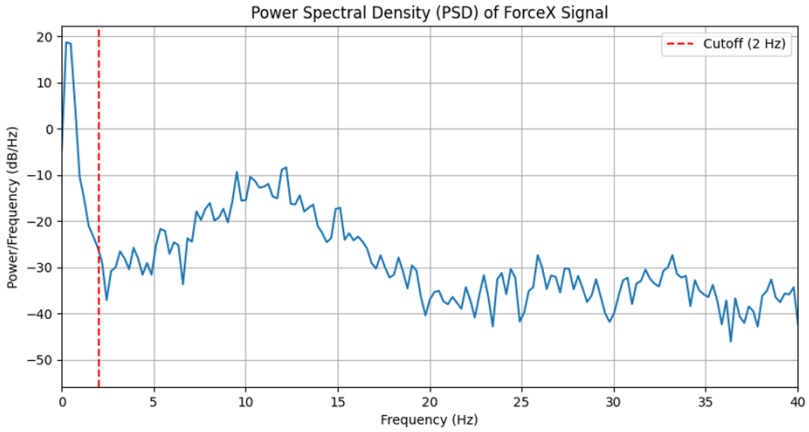

Figure 4.23: Results from Power Spectrum Density (PSD) analysis that provides a quantitative measure of the signal's energy distribution across different frequency bands, offering additional confirmation of the frequency ranges dominated by noise/vibration.

signal was subtracted and a Hanning window was applied to minimize spectral leakage and improve frequency resolution. The resulting FFT analysis enabled the identification of the dominant frequency components present in the signal, distinguishing between those associated with the actual physical motion and those attributable to possible sensor noise, as shown in figure 4.22.

To further validate the findings from the FFT, a Power Spectrum Density (PSD) analysis was also conducted, as shown in figure 4.23. This analysis provided a quantitative measure of the signal's energy distribution across different frequency bands, offering additional confirmation of the frequency ranges dominated by possible noise signals.

Both analyses consistently indicated that a pronounced separation is visible between low-frequency components, below approximately 2 Hz, and those concentrated around the 9–15 Hz region. The low-frequency content directly corresponds to the fundamental kinematic frequencies prescribed for the flapping motion, governed by the wingbeat period (approximately 0.4 Hz for the experimental cycle). These low-frequency harmonics encode the slow, periodic forces generated by the primary physical motion of the wing, and thus reflect the true hydrodynamic responses expected from the experiment. In contrast, the spectral peak observed between 9–15 Hz does not align with any prescribed physical motion, nor with plausible harmonics of the wing kinematics. The source of this energy cannot be attributed to random electronic noise, as such a feature would not be coherent or repeatable across multiple trials. Averaging across repetitions would reduce non-correlated sensor noise, but the persistence of this peak suggests a structural resonance, a vibrational mode of the shaft-wing assembly or mounting system that is excited during the rapid acceleration and deceleration phases of wing motion. Based on manual Rayleigh calculations, the natural frequency of the wing-shaft assembly was

estimated to be about 20–25 Hz, which is already in the same frequency range as the observed vibration peaks at 10–15 Hz, especially when considering minor compliance in the clamping or fixtures. This assumption goes well with the documented observations of high-frequency oscillations and mechanical vibration discussed throughout the implementation challenges (Appendix A.6).

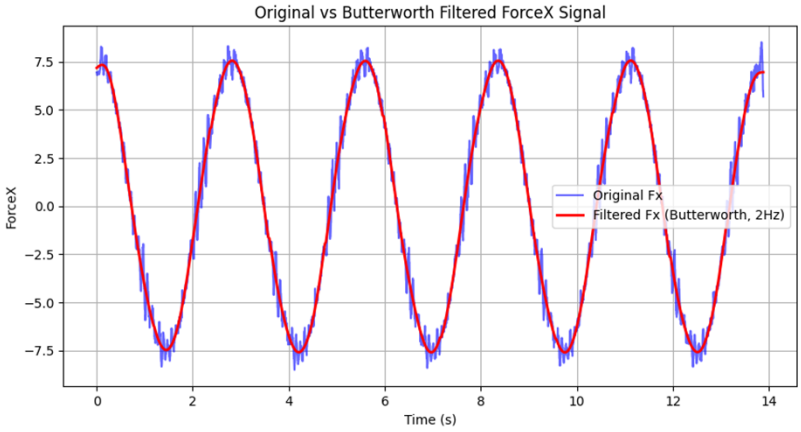

Figure 4.24: Comparison of the raw signal against the filtered signal at a cut of frequency of 2Hz

Based on the combined spectral analyses, a low-pass filter with a cutoff frequency of 2 Hz was selected for all subsequent post-processing stages. This choice was motivated by the observation, from both FFT and PSD analyses, that all frequency components above approximately 2 Hz appeared to be dominated by vibration issues, with the physically meaningful content of the force signal largely concentrated below this threshold. Importantly, setting the cutoff below this frequency - such that only the lowest one or two Fourier coefficients remain - would yield either a simple average value or a pure sinusoidal representation. While this would maximize noise/vibration suppression, it would also risk over-simplifying the data and excluding possible legitimate high-frequency features associated with physically relevant force fluctuations during the wingbeat. Conversely, adopting a significantly higher cutoff (e.g., 10 Hz) would fail to sufficiently remove evident noise/vibration contributions seen in the raw sensor output. The 2 Hz cutoff therefore represents a conservative yet safe approximation, balancing the need to retain dynamic force features linked to the prescribed wing kinematics, ensuring the post-processed force measurements remain both physically interpretable and quantitatively reliable for subsequent aerodynamic analysis. The effectiveness of this filtering strategy is illustrated in figures 4.25a, 4.25b, 4.25c, 4.25d and 4.25e, which demonstrate that the 2 Hz filtered data maintains signal fidelity while markedly enhancing signal-to-noise ratio.

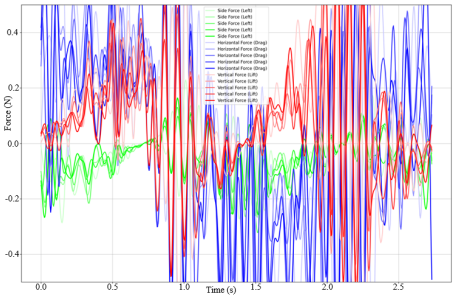

(a) Cutoff: 13 Hz

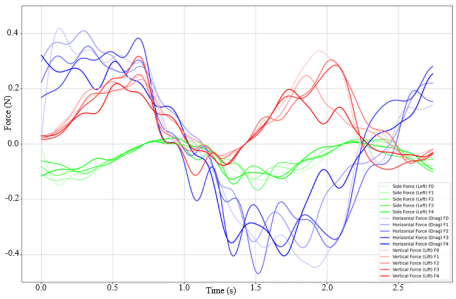

(b) Cutoff: 5 Hz

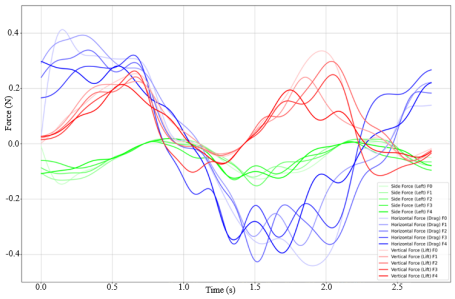

(c) Cutoff: 4 Hz

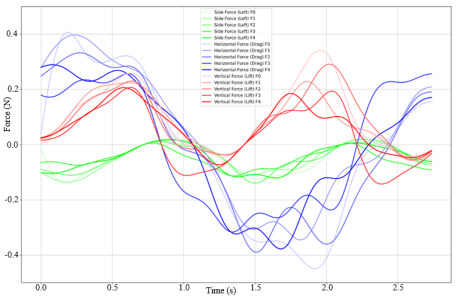

(d) Cutoff: 3 Hz

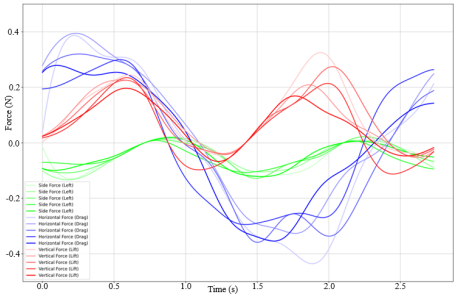

(e) Cutoff: 2 Hz

Figure 4.25: Transformed forces filtered using various low-pass cutoff frequencies. The Red, Blue and Green lines correspond to the Lift, Drag and Side forces, respectively, across the middle cycles.

ISOLATION OF WING-WAKE INTERACTION EFFECTS

The final stage of aerodynamic analysis focuses on isolating wing-wake interaction forces by comparing experimentally measured forces from the Staubli robot with predictions from the quasi-steady model. After transforming both datasets into the global coordinate system, the quasi-steady forces, which assume instantaneous force equilibrium and neglect wake effects, are subtracted from the experimental forces. This differential approach captures deviations attributable to unsteady phenomena, particularly the interaction between the wing and its self-generated wake. Thus, the residual forces represent the net contribution of wing -wake interaction, not modelled in the quasi-steady framework.

To quantify how wing kinematics modulate wake interactions, this subtraction process is repeated across trials with systematically varied deviation angles. By altering the vertical component of wing motion, different wake topologies are generated. Analysing the residuals across these trials reveals the sensitivity of wake effects to kinematic parameters, such as how increased deviation amplifies wake-induced lift fluctuations during stroke reversals. This parametric study provides critical insights into optimizing wing trajectories to either exploit favourable wake interactions (e.g., wake capture for enhanced lift) or minimize detrimental ones (e.g., vortex-induced drag).

Note that during each experiment, force measurements were recorded over complete flapping cycles, consisting of both downstroke and upstroke phases. Analysis revealed pronounced symmetry between these phases, attributable to the sinusoidal kinematic protocol, with lift profiles nearly identical and drag profiles showing sign-inverted correspondence. Given this, both upstroke and downstroke data were averaged at each phase to enhance statistical reliability and mitigate experimental variability (see Section 5.8 for detailed justification). This approach ensures robust extraction of aerodynamic force trends from the measured data.

4.4. SETTING UP THE QUASI-STEADY MODEL ON MATLAB

4.4.1. INPUT FRAMEWORK FOR THE QUASI-STEADY MODEL

The model requires four primary input categories to compute aerodynamic forces on flapping wings. First, wing geometry is defined by the wing length (R) and aspect ratio (AR), which determine the spanwise discretization and chord distribution. These parameters influence the lift-generating capacity through the modified lifting line theory, with higher aspect ratios enhancing aerodynamic efficiency by reducing induced drag. Second, the flapping time period sets the base frequency of motion, scaled via a dimensionless *freq_factor* to study frequency-dependent effects without altering the kinematic pattern. Third, fluid density (ρ) directly scales force magnitudes, enabling adaptation to different media (e.g., air vs. liquid environments).

The most critical input is the kinematic profile derived from Staubli robot measurements, which defines the time-varying Euler angles - stroke (Φ), deviation (Θ), and pitch (α). To ensure kinematic consistency, the Fourier series coefficients are constructed specifically from the average of the middle cycles of the five consecutive flapping cy-

cles executed by the Staubli robot. This approach excludes transient effects present in the initial and final cycles, isolating a representative steady-state motion for analysis.

A custom Python program processes the raw robot output by extracting and averaging the middle cycles of the recorded data to minimize transient effects. This averaged time-domain signal is then subjected to a Fourier transform, which is necessary to convert the discrete, potentially noisy measurements into a smooth, continuous harmonic representation compatible with the quasi-steady model's numerical framework. The resulting harmonic coefficients encode the essential frequency components of the wing motion, enabling precise reconstruction of the Euler angles, as illustrated in Figure 4.26.

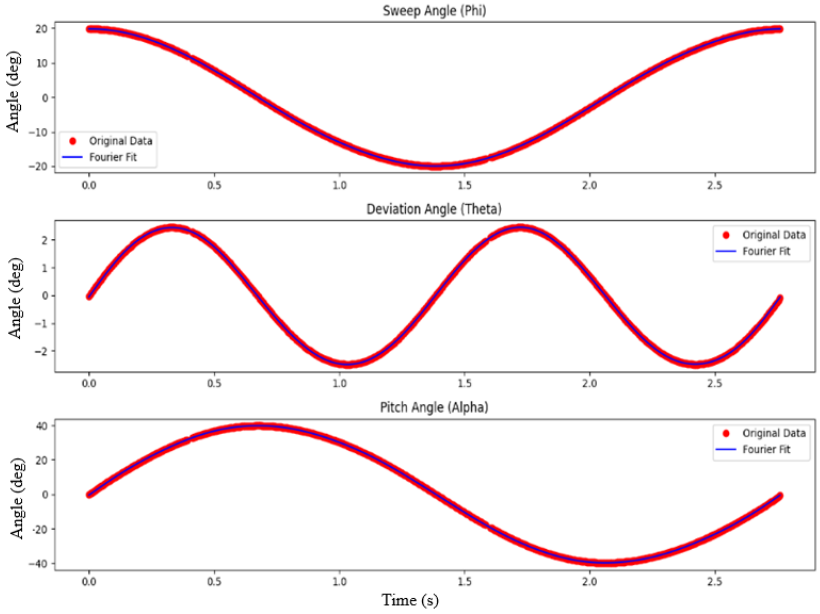

Figure 4.26: Fourier Fit of actual kinematics performed on Staubli Robot. This fourier fit will be now used as input to the QS Model.

The Fourier decomposition captures higher-order harmonics (up to eight times the base frequency), which resolve rapid pitch adjustments and stroke reversals essential for biological realism, as shown in Appendix figure A.1. The decision to retain up to eight harmonics was with the intention to maintain a sufficiently high resolution of the key transient features in the wing motion while avoiding excessive complexity and potential overfitting to noise.

The kinematics are sampled at 101 timepoints per flapping cycle, a choice informed by the need to ensure sufficient temporal resolution. Given that the Fourier-transformed kinematics exhibit predominantly sinusoidal and symmetric patterns, increasing the sampling density beyond this level did not yield appreciable returns in accuracy. Al-

though higher sampling rates could provide finer resolution in principle, the relatively smooth nature of the underlying signals suggested that 101 points adequately capture the relevant dynamic features. Phase alignment between Φ, Θ, and α preserves the temporal coordination of rotational motions observed in biological systems, ensuring physically consistent force phasing. This input framework allows the model to reconstruct insect-like flapping patterns while retaining the flexibility to explore unorthodox kinematic regimes, such as varying deviation angles.

4.4.2. AERODYNAMIC FORCE COMPUTATION IN WING-BOUND COORDINATES

The QS model calculates aerodynamic forces through a systematic pipeline that translates kinematic inputs into wing-bound force components. This process involves four key stages: angular kinematics derivation, coordinate transformation, force component computation, and visualization.

ANGULAR KINEMATICS AND WING-BOUND COORDINATE TRANSFORMATION

The first step computes time derivatives of Euler angles (Φ, Θ, α) using central differencing. Angular velocities ($\dot{\Phi}$, $\dot{\Theta}$, $\dot{\alpha}$) and accelerations ($\ddot{\Phi}$, $\ddot{\Theta}$, $\ddot{\alpha}$) are numerically derived from the reconstructed kinematics. These derivatives quantify the wing's rotational dynamics, essential for determining inertial and Coriolis effects in subsequent force calculations.

Euler angles and their derivatives are transformed into wing-bound angular velocities (ω_{xc}, ω_{yc}, ω_{zc}) using rigid body rotation principles. This conversion accounts for coupled rotations across all three axes - stroke, deviation, and pitch - ensuring forces are computed relative to the wing's instantaneous orientation. Angular accelerations are similarly transformed to capture unsteady effects critical for added-mass force calculations.

FORCE COMPONENT COMPUTATION

To accurately represent the time-dependent aerodynamic forces acting on the flapping wing, the quasi-steady model systematically decomposes the total force into four distinct components, each associated with a primary physical mechanism of force generation: translation, rotation, coupling, and added mass. These components are computed within the wing-bound (co-rotating) frame to ensure the local instantaneous orientation and velocity of the wing are precisely accounted for throughout the flapping cycle. By doing so, this framework enables a rigorous separation of circulatory lift, rotational pressure forces, nonlinear kinematic coupling, and fluid inertial reaction effects, all of which contribute to the net aerodynamic response, as shown in figure 4.27.

Translational Forces:

The translational force component captures the aerodynamic lift and drag produced by the wing as it moves through the fluid. Following the approach outlined by Wang et al. [56], the quasi-steady model applies a modified lifting line theory adapted to unsteady flapping kinematics. The underlying principle is that the instantaneous aerodynamic

force coefficients depend primarily on the effective angle of attack (AoA), which is derived from the local instantaneous velocity components of the wing in the co-rotating frame.

The effective AoA, denoted as $\tilde{\alpha}$, is defined based on the angular velocity components normal to the wing chord. Specifically, using the local angular velocity components ω_y^c and ω_z^c, where the subscript c indicates the chord-wise coordinate frame, the effective AoA is computed as:

$$\tilde{\alpha} = \arccos\left(\left|\frac{\omega_y^c}{\sqrt{(\omega_y^c)^2 + (\omega_z^c)^2}}\right|\right). \tag{4.1}$$

Here, ω_y^c and ω_z^c represent the instantaneous angular velocities about the spanwise (y) and normal (z) axes of the wing, respectively. The absolute value ensures a positive angle measurement independent of direction.

The maximum lift coefficient $C_{L,\max}$ is determined from the wing's aspect ratio (AR) according to the empirical relation:

$$C_{L,\max} = \pi \cdot \frac{AR}{2 + \sqrt{AR^2 + 4}}, \tag{4.2}$$

which captures the finite-wing effects on lift generation in subcritical regimes.

Using this maximum lift coefficient and the calculated effective AoA, the instantaneous translational lift coefficient, denoted C_L^{trans}, is expressed as:

$$C_L^{\text{trans}} = C_{L,\max} \cdot \sin(2\tilde{\alpha}), \tag{4.3}$$

reflecting the sinusoidal dependence of lift on AoA commonly observed in thin airfoil theory and modified here for flapping wing conditions.

Assuming that the resulting aerodynamic force acts perpendicular to the wing chord, the corresponding drag coefficient due to translational motion is modeled as proportional to the lift coefficient and the tangent of the effective AoA:

$$C_D^{\text{trans}} = C_L^{\text{trans}} \cdot \tan(\tilde{\alpha}). \tag{4.4}$$

Accordingly, the total chord-normal force coefficient, which combines both lift and drag components resolved normal to the chord, is given by:

$$C_{F_{yc}}^{\text{trans}} = \frac{C_L^{\text{trans}}}{\cos(\tilde{\alpha})}. \tag{4.5}$$

To obtain the net translational force in the y_c direction, corresponding to the velocity-normal force component in the co-rotating chord frame, an integration is performed across the span of the wing. The local chord length is denoted by $c(x)$ at the radial spanwise coordinate x, and ρ is the fluid density. The translational force magnitude accounts for the square of the local angular velocity orthogonal to the chord:

$$F_{y_c}^{\text{trans}} = -\frac{1}{2} \cdot \text{sgn}(\omega_z^c) \cdot \rho \cdot \left((\omega_y^c)^2 + (\omega_z^c)^2 \right) \cdot C_{F_{y_c}}^{\text{trans}} \cdot \int_0^R x^2 c(x), dx. \tag{4.6}$$

The sign function $\text{sgn}(\omega_z^c)$ accounts for directional dependence related to wing rotation about the z-axis. The radial weighting by $x^2 c(x)$ arises from the lifting line integral adapted for the wing's geometric and kinematic distribution along the span. Numerical evaluation of this integral is performed using trapezoidal integration over discretized spanwise elements r_i, capturing the variation in chord distribution and velocity along the wing.

Thus, these expressions quantify the instantaneous aerodynamic force produced by the wing's translational motion, incorporating geometric effects via the aspect ratio and chord distribution, and kinematic effects via the effective angle of attack derived from local angular velocities. This component forms a fundamental part of the overall quasi-steady force model, enabling accurate representation of circulatory lift and induced drag during flapping.

Rotational Forces:

The rotational force component accounts for aerodynamic effects arising due to pitching motion of the wing, specifically rotation about the local chordwise axis denoted as x_c. These forces primarily result from pressure asymmetries induced by centrifugal effects as the wing undergoes angular acceleration about this axis. Following the formulation presented by Wang et al. [56], the model treats these effects as a distributed damping force acting along the wing chord.

The rotational drag coefficient, C_D^{rot}, quantifies the aerodynamic resistance due to pure rotational motion of the wing section. It is derived through an extension of lifting-line theory and analogized to the drag experienced by a flat plate at a 90° angle of attack, expressed as:

$$C_D^{\text{rot}} = 2\pi \cdot \frac{AR}{2 + \sqrt{AR^2 + 4}}, \tag{4.7}$$

where AR denotes the wing's aspect ratio. This coefficient captures the enhanced drag associated with flow separation and pressure differentials during pitching.

To compute the total rotational force, the wing is discretized spanwise along the radial coordinate x from root (0) to tip (R). At each spanwise station, the wing chord is further

discretized chordwise between the trailing edge and leading edge locations, denoted by $c_{\min}(x)$ and $c_{\max}(x)$ respectively. These limits are functions of the local chord length and wing geometry, with $c_{\max}(x)$ obtained from the leading edge vector, and $c_{\min}(x) = c_{\max}(x) - c(x)$ representing the trailing edge.

The local chordwise coordinate relative to the pitching axis is denoted by z_c, varying between $c_{\min}(x)$ and $c_{\max}(x)$. The distributed rotational force contribution at each chordwise element is modeled via the integrand $z_c \cdot |z_c|$, which reflects the spatial weighting of centrifugal pressure loads across the chord.

Therefore, the rotational force component in the y_c direction (normal to the chord) is given by the double integral expression:

$$F_{y_c}^{\text{rot}} = \frac{1}{2}\rho \cdot \omega_x^c \cdot |\omega_x^c| \cdot C_D^{\text{rot}} \cdot \int_0^R \left(\int_{c_{\min}(x)}^{c_{\max}(x)} z_c \cdot |z_c|, dz_c \right) dx, \tag{4.8}$$

where ρ is the fluid density, and ω_x^c represents the instantaneous angular velocity about the chordwise axis. The factor $\omega_x^c \cdot |\omega_x^c|$ preserves the sign and magnitude of rotational velocity squared, ensuring the force acts in the physically correct direction with appropriate magnitude scaling.

The inner integral evaluates the chordwise distribution of pressure-induced rotational forces at each spanwise station, while the outer integral numerically sums these contributions along the wing span. The integrals are computed using trapezoidal numerical integration over discretized segment vectors, accurately capturing wing geometry and kinematics.

This rotational force component captures fluid dynamic effects associated with wing pitching motions, complementing the translational force calculations and contributing to the comprehensive determination of instantaneous aerodynamic forces in the quasi-steady framework.

Coupling Forces:

The coupling force component arises from nonlinear aerodynamic interactions between translational and rotational motions of the wing. Specifically, this effect accounts for the shift in the local aerodynamic centre of pressure (CP) caused by the sign and magnitude of the spanwise angular velocity, ω_y^c. This shift alters the distribution of aerodynamic loading along the wing and consequently introduces an additional force component not captured by purely translational or rotational terms alone.

Physically, the sign of ω_y^c indicates the wing's pitching direction relative to the flow:

- For $\omega_y^c < 0$ (leading-edge-down motion), the centre of pressure moves toward the leading edge of the wing, causing a forward shift in aerodynamic loading.
- For $\omega_y^c > 0$ (leading-edge-up motion), the centre of pressure shifts aft, toward the

trailing edge.

Mathematically, the total coupling force in the chord-normal direction y_c is expressed as a piecewise function dependent on the sign of ω_y^c:

$$F_{y_c}^{\text{coup}} = \begin{cases} \pi\rho\,\omega_x^c\omega_y^c \left[\int_0^R \left(\left(0.75 - \hat{d}(x)\right) c(x)^2 x \right) dx + \int_0^R \left(0.25\, c(x)^2 x\right) dx \right], & \omega_y^c \le 0 \\ \pi\rho\,\omega_x^c\omega_y^c \left[\int_0^R \left(\left(\hat{d}(x) - 0.25\right) c(x)^2 x \right) dx + \int_0^R \left(0.25\, c(x)^2 x\right) dx \right], & \omega_y^c > 0 \end{cases} \tag{4.9}$$

where the normalized pitching axis location $\hat{d}(x)$ is defined as:

$$\hat{d}(x) = \frac{\text{LE offset at } x}{c(x)},$$

with $c(x)$ denoting the local chord length at spanwise position x. This normalization quantifies the relative position of the pitching axis with respect to the chord length, influencing the lever arm of aerodynamic moments and the resulting force distribution.

The two integral terms within each bracket have distinct physical interpretations:

1. The first integral captures the asymmetry in rotational circulation induced by the shifted centre of pressure, which depends on the relative pitching axis offset and varies with spanwise position. This term modulates the force contribution according to the instantaneous kinematic coupling of angular velocities.

2. The second integral represents the Coriolis-induced pressure contribution, symmetric with respect to stroke direction, reflecting inertial coupling effects between rotational and translational velocities.

Both integrals are evaluated numerically using trapezoidal integration over discretized spanwise elements, ensuring precise incorporation of chord geometry and pitching axis variation along the wing.

In summary, the coupling force component models the subtle, yet significant, nonlinear aerodynamic effects generated by the interaction between the wing's pitching and spanwise rotation, enriching the quasi-steady model's capacity to capture realistic unsteady aerodynamic loading beyond isolated translational and rotational terms.

Added-Mass Forces:

The added-mass effect arises from the acceleration or deceleration of the fluid surrounding a flapping wing, which in turn exerts a reactive force opposing the wing's motion. This effect is particularly significant during rapid changes in wing velocity, such as stroke reversals. To model the added-mass force, the wing is discretized into two-dimensional chordwise strips, and potential flow theory results for simple 2-D bodies are applied. For a wing strip with chord length c and a pitching axis located at a normalized distance $\hat{d}$ from the leading edge, the added-mass coefficients are expressed as a matrix M,

which relates the translational and rotational accelerations to the corresponding force and torque components. The matrix is given by:

$$M = \begin{bmatrix} m_{22} & m_{24} \\ m_{42} & m_{44} \end{bmatrix} = \frac{\pi}{4}\rho_f c^2 \begin{bmatrix} 1 & c\left(\frac{1}{2} - \hat{d}\right) \\ c\left(\frac{1}{2} - \hat{d}\right) & \frac{1}{32}c^2 + c^2\left(\frac{1}{2} - \hat{d}\right)^2 \end{bmatrix}, \tag{4.10}$$

where ρ_f is the fluid density. The terms m_{22} and m_{44} represent the added-mass coefficients associated with translational and rotational accelerations, respectively, while m_{24} and m_{42} account for the coupling between these motions due to the pitching axis offset. The resulting added-mass force F_{yc}^{am} and torque τ_{xc}^{am} are calculated by integrating the product of the coefficient matrix M and the acceleration vector $\left[a_{yc}, \alpha_{xc}\right]^T$ along the wing span:

$$\begin{bmatrix} F_{yc}^{am} \\ \tau_{xc}^{am} \end{bmatrix} = -\int_0^R M \begin{bmatrix} a_{yc} \\ \alpha_{xc} \end{bmatrix} dx_c, \tag{4.11}$$

where a_{yc} and α_{xc} are the translational and rotational accelerations in the co-rotating frame, respectively, and R is the wing span. This formulation captures the inertial reaction of the fluid in both translation and rotation, incorporating effects of wing geometry and pitching axis location.

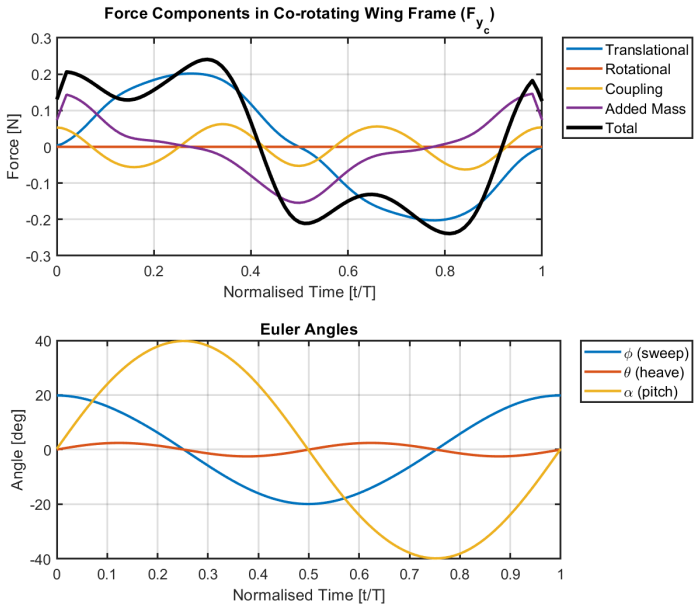

Figure 4.27: Force Components in the Co-rotating Wing Frame, derived from the Quasi-steady model, plotted against Time and Euler Angles, for a representative case with a wing deviation angle of 2.5°.

The contributions of each quasi-steady aerodynamic force component - translational,

rotational, coupling, and added-mass - to the total computed force are illustrated in the figure 4.27 for a representative case with a wing deviation angle of 2.5°. The upper panel of the figure presents the time-resolved evolution of each force component and their summation throughout a normalized flapping cycle. The lower panel displays the corresponding Euler angles (sweep, deviation, and pitch) that define the imposed wing kinematics for this condition. This visualization enables direct comparison of the temporal phasing and relative magnitudes of each aerodynamic contribution and highlights how the combined aerodynamic response evolves with the underlying prescribed kinematics. The figure thereby demonstrates the ability of the quasi-steady framework to decompose the total force into physically interpretable components, providing insight into the dynamic interplay between flapping motion and force generation.

A notable feature in the figure 4.27 is the presence of a pronounced "kink" at the beginning and end of the added mass force profile, which in turn appears in the computed total force. This discontinuity is most likely attributable to numerical artifacts inherent in the quasi-steady governing equations and their discrete implementation within the MATLAB code. Specifically, added mass forces depend directly on the accelerations of both linear and angular kinematic variables, which are typically computed via finite differences of discretely sampled velocity and angular velocity time series. At the boundaries of the flapping cycle - corresponding to the initial and final timepoints - finite difference schemes can introduce abrupt changes or spurious transients. These discontinuities often arise from imperfect periodicity or mismatch between the boundary conditions implicitly assumed in the governing equations and the actual discretized data. As a result, the differentiation process can yield artificially large or mismatched values at the cycle endpoints, especially if the kinematic profiles, though periodic in theory, are not perfectly matched at their start and end due to data processing or Fourier series truncation. Consequently, the kinks observed are best interpreted as numerical artifacts rather than reflections of underlying physical dynamics.

4.4.3. FORCE TRANSFORMATION AND VISUALIZATION

The final stage of the quasi-steady model translates wing-bound aerodynamic forces into the global coordinate system and generates comprehensive visualizations to interpret results. This process ensures aerodynamic forces align with the insect's body frame, enabling analysis of flight-relevant metrics like lift, drag, and side forces.

COORDINATE SYSTEM TRANSFORMATION: ROTATIONAL MATRICES AND FORCE PROJECTION

The transformation of aerodynamic forces from the wing-bound to the global coordinate system is governed by three sequential rotational matrices, each corresponding to a fundamental Euler angle: stroke (Φ), deviation (Θ), and pitch (α). These matrices mathematically represent the physical reorientation of the wing as it moves through its flapping cycle.

1. **Stroke Rotation (Φ about the global ζ-axis)**
   The stroke matrix, R_Φ, rotates the wing about the insect's vertical axis (ζ), aligning

the motion with the horizontal stroke plane. This rotation defines the back-and-forth sweeping motion of the wing, converting the global ξ–η plane into a stroke-oriented frame.

2. **Deviation Rotation (Θ about the intermediate η-axis)**
The deviation matrix, R_Θ, tilts the wing vertically about the new η-axis (perpendicular to the stroke plane). This rotation accounts for upward/downward deviations during stroke reversals, adjusting the wing's elevation relative to the stroke plane.

3. **Pitch Rotation (α about the wing-bound x-axis)**
The pitch matrix, R_α, rotates the wing about its own leading edge (x-axis), altering the angle of attack. This final rotation aligns the wing's chordwise orientation with the instantaneous flow, critical for lift generation.

The composite transformation matrix $R_{\text{all}} = R_\Phi \cdot R_\Theta \cdot R_\alpha$ sequentially applies these rotations, mapping forces from the wing-bound frame (x_c, y_c, z_c) to the global insect frame (ξ, η, ζ) as shown in the Appendix code A.2. The wing's normal force (acting along y_c) is projected onto the global axes through matrix multiplication as:

$$F_{\text{global}} = R_{\text{all}} \cdot \begin{bmatrix} 0 \\ F_{y_c} \\ 0 \end{bmatrix}$$

This decomposes the wing-normal force into three biologically meaningful components:

- **Side force (F_ξ):** Lateral force perpendicular to the forward thrust direction, in the stroke plane
- **Drag (F_η):** Rearward horizontal force opposing forward thrust
- **Lift (F_ζ):** Vertical force supporting weight

This transformation is applied individually to each force mechanism - translational, rotational, coupling, and added mass - to preserve their distinct contributions. By isolating these components, the model enables precise analysis of how specific aerodynamic phenomena (e.g., rotational pressure gradients or added-mass effects) influence overall flight dynamics. The sequential rotation order ensures kinematic consistency with biological wing motion, where stroke establishes the primary motion plane, deviation introduces vertical adjustments, and pitch fine-tunes angle of attack for optimal force generation.

FORCE SYNTHESIS AND VISUALIZATION

The model generates two parallel sets of plots: one in the global frame showing flight-relevant forces, and another in the wing-bound frame illustrating aerodynamic mechanisms. Global plots decompose total forces into side, drag, and lift components, overlaying individual contributions from translational, rotational, coupling, and added-mass

effects as shown in figure 4.28. Wing-bound plots reveal how normal forces evolve relative to the wing's orientation, with subplots comparing force magnitudes against Euler angle trajectories. Additional figures track lift coefficients over time and validate component-wise force superposition.

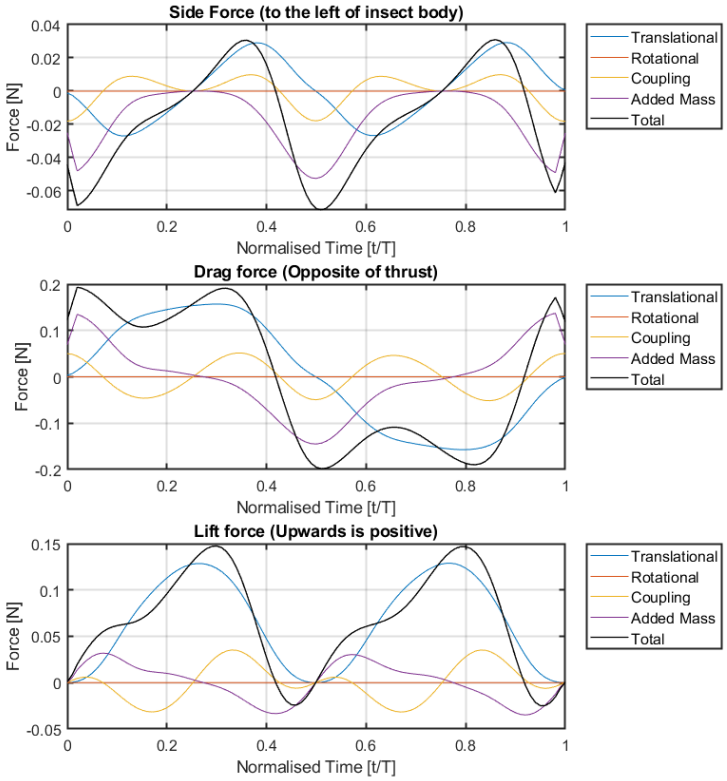

Figure 4.28: Transformed Global Forces along with the force decomposition, obtained from the QS Model, for a representative case with a wing deviation angle of 2.5°.

Visualizations highlight phase relationships between kinematic events (e.g., stroke reversals) and force peaks, exposing how pitch adjustments modulate lift generation. The side force profile captures lateral accelerations during asymmetric strokes, while drag components indicate thrust/drag trade-offs. By preserving mechanism-specific force traces, the plots enable identification of dominant effects at different flight stages - translational forces typically dominate mid-stroke, while added-mass effects peak during rapid pitch changes. These outputs facilitate both qualitative validation against biological observations and quantitative comparison with experimental force measurements.

5

ASSUMPTIONS, ABSTRACTIONS AND LIMITATIONS

In this study, several approximations and assumptions are made to simplify the experimental setup and focus on the primary research objectives. While these simplifications may limit the scope of certain aerodynamic phenomena, they provide a practical starting point for understanding the effect of deviation angle on wake capture forces, during mosquito-like hovering flight. The key assumptions, abstractions and limitations in this study are as follows:

5.1. WING FLEXIBILITY

This study adopts the assumption of rigid wing structure, employing Stainless Steel plates (shown in figure 4.4) to represent mosquito wings instead of replicating their naturally flexible and deformable morphology. This simplification intrinsically excludes the aerodynamic influence of structural flexibility, which in biological insect flight contributes to dynamic force modulation through passive deformation [21][23]. In real mosquitoes, wing flexibility can facilitate spanwise and chordwise bending in response to unsteady aerodynamic loads, thereby modifying the effective angle of attack and temporal force development. Such aeroelastic responses might enhance lift generation, delay flow separation, and promote flight stability, particularly under transient or perturbed conditions.

The use of rigid wings in this experimental setup allows the isolation and analysis of parameters directly associated with prescribed kinematics, such as deviation angle, without introducing the additional variables and nonlinearities inherent to fluid-structure interaction models, as well as the additional modeling complexities it imposes. While this assumption does limit the biological fidelity of the results, it ensures that observed aerodynamic effects can be unambiguously attributed to kinematic variation rather than structural coupling. This approach provides a controlled baseline for evaluating unsteady aerodynamic mechanisms in simplified conditions, against which future studies

incorporating wing flexibility can be benchmarked.

5.2. SIMPLIFIED KINEMATICS

As explained in section 4.3.2, the wing motion used in this study is derived from idealized kinematic profiles rather than directly implementing the complex, time-resolved kinematics observed in actual mosquito flight.

To inform this simplification, high-resolution kinematic data from mosquito flight were analyzed to observe that the sweep and deviation angles exhibit nearly sinusoidal trends, while the pitch angle shows a quasi-sinusoidal profile with more irregularity, as shown in figure 4.14. To translate these observed patterns into a form suitable for experimental implementation, a Fourier decomposition was applied to the measured trajectories. The dominant frequency components were retained to construct sinusoidal approximations for each Euler angle.

This simplification is adopted to enable precise control over parameters such as sweep, deviation, and pitch angles, which is essential for conducting systematic parametric studies. This reduced-order representation preserves the essential temporal features of the wing motion while facilitating repeatability and controlled variation in the experimental setup. Although it does not capture the full intricacies of real insect wing motion [58, 19], this approach provides a practical framework for investigating the aerodynamic consequences of specific kinematic variations, such as the effect of deviation angle on wake capture forces.

5.3. ABSTRACTION TO A RECTANGULAR WING PROFILE: RATIONALE AND IMPLICATIONS

As briefly discussed in section 4.1.2, the wing assembly to be mounted on the robot arm was intially planned to be a dynamically scaled model of an Aedes aegypti mosquito wing. This wing profile was sourced from Prof. Dr. A. J. L. L. Buchner, by imaging a number of Aedes mosquito wings under a microscope and using edge detection method to determine the outline and thereafter scaling and averaging the profile, as shown in figure 4.3. Once the wing profile was finalized, it was planned to be laser-cut from a 4 mm thick steel plate at the mechanical engineering student workshop, ensuring precision and structural integrity.

5.3.1. REYNOLDS NUMBER AND WING PROFILE SCALING

To accurately replicate the aerodynamic characteristics of a hovering mosquito's wing flapping, the wing profile was scaled up using AutoCAD software, shown in figure 5.1. This scaling involved adjusting both the chord length and the span length of the wing to match the Reynolds number corresponding to the natural wing motion. It is important to note that the scaling process was not limited to geometric dimensions alone; rather, it involved a combined adjustment of the wing dimensions and the fluid viscosity to ensure dynamic similarity in terms of the Reynolds number.

Literature review [27] indicates that the Reynolds number for hovering mosquitoes is ap-

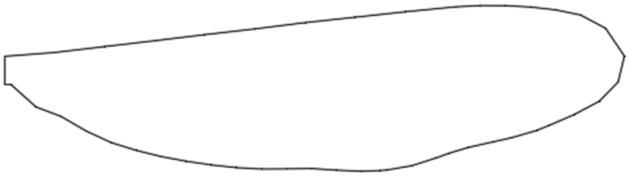

Figure 5.1: The scaled Wing Profile for Laser Cutting. This profile was generated by digitizing the original geometry in CAD software, followed by smoothing and upscaling to match the required dimensions for fabrication.

proximately 120, which serves as the target value for the scaled experimental model. The Reynolds number is fundamentally a function of three key parameters: the flapping frequency, the kinematic viscosity of the fluid medium, and the characteristic dimension of the wing, specifically the mean chord length. This relationship necessitates careful consideration of the experimental constraints and systematic optimization of the wing dimensions and fluid properties to achieve the desired Reynolds number while maintaining practical feasibility within the experimental setup.

The experimental setup imposes several dimensional constraints that must be considered in the wing design process. These constraints include the physical dimensions of the fluid tank, the operational reach and workspace limitations of the robotic arm, and critical safety considerations to prevent interaction between the robot sensors and the experimental fluid. Given these limitations, it became essential to develop a systematic approach for determining the optimal range of wing dimensions and fluid viscosity levels that would maintain the required Reynolds number while satisfying all operational constraints. To address these challenges, a mathematical framework was established based on the fundamental expression for Reynolds number. The Reynolds number is defined as:

$$\mathrm{Re} = \frac{V_{\mathrm{tip}} \times C_m}{\nu} \tag{5.1}$$

where Re represents the Reynolds number, V_{tip} denotes the wing tip velocity, C_m is the mean chord length, and ν is the kinematic viscosity of the fluid. Rearranging this expression to solve for the kinematic viscosity yields:

$$\nu = \frac{V_{\mathrm{tip}} \times C_m}{\mathrm{Re}} \tag{5.2}$$

which provides the foundation for the optimization process.

Mathematical Framework for Wing Design

The wing tip velocity can be expressed in terms of the kinematic parameters of the flapping motion as:

$$V_{\text{tip}} = \frac{2 \times \text{stroke amplitude} \times R}{\text{Time period}}.$$

For mosquito hovering flight, the stroke amplitude is approximately 40 degrees, which must be converted to radians for mathematical calculations. The wing length R is related to the mean chord length through the aspect ratio relationship:

$$R = AR \times C_m,$$

where AR represents the aspect ratio of the wing. The time period is simply the reciprocal of the flapping frequency, expressed as:

$$\text{Time period} = \frac{1}{\text{Frequency}}.$$

Substituting these relationships into the Reynolds number expression and solving for the kinematic viscosity yields a quadratic equation that relates the kinematic viscosity ν to the mean chord length C_m. This relationship can be expressed as:

$$\nu = \left(\frac{80 \times \pi}{180 \times Re}\right) \times \left(\frac{AR}{\text{Time Period}}\right) \times C_m^2 \tag{5.3}$$

This equation demonstrates that the kinematic viscosity varies quadratically with the mean chord length, providing a clear mathematical framework for optimizing the wing dimensions and fluid properties.

A Python program was developed to systematically sweep through a range of possible kinematic viscosity levels and mean chord lengths that would satisfy the dimensional constraints of the experimental setup, as shown in figure 5.2. This computational approach enabled the identification of optimal parameter combinations that achieve the target Reynolds number while remaining within the practical limitations of the experimental apparatus. The optimization process involved plotting the relationship between these parameters to visualize the feasible design space and identify the optimal operating point.

Based on these calculations, the optimal wing mean chord length was determined, and the corresponding wing length was calculated using the predefined aspect ratio of 5.3 [33], inorder to scale up the actual mosquito wing profile. This scaling process ensured that the geometric proportions of the biological wing were maintained while achieving the required size for the required Reynolds number.

5.3.2. RECTANGULAR WING ABSTRACTION

Despite all the above calculations and planning, for the final experimental configuration, it was decided to use a simplified rectangular stainless steel plate, originally employed during intermediate water trials to validate system performance and force measurement

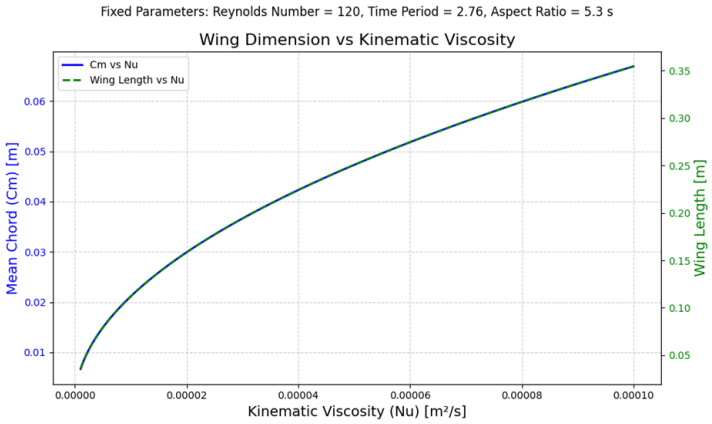

Figure 5.2: Result from the Python program developed to systematically sweep through a range of possible kinematic viscosity levels and mean chord lengths that would satisfy the dimensional constraints of the experimental setup.

5

protocols as explained in section 4.1.2. This decision was based on the fact that a rectangular wing configuration provided a geometrically straightforward platform for initial system calibration, enabling verification of kinematic programming, force measurement reliability, and vibration characteristics before transitioning to more complex wing morphologies.

Importantly, the use of a rectangular plate represents a deliberate abstraction of the biological problem, facilitating a broader generalization of the findings beyond the specific case of mosquito flight. By employing a simplified planform, the study aims to isolate and clarify the role of deviation angle in modulating wing–wake interaction forces under controlled and repeatable conditions. This abstraction minimizes the influence of species-specific morphological nuances, such as leading-edge taper, trailing-edge curvature, and spanwise chord variation, thereby ensuring that the conclusions drawn regarding the relationship between kinematics and unsteady aerodynamic force generation are broadly applicable to a wider class of insect-like flapping systems, including those relevant for the design of bioinspired micro air vehicles. The symmetry and uniformity of the simple rectangular profile also promotes predictable force distributions and streamlines numerical integration in the quasi-steady framework.

Nevertheless, this geometric simplification constitutes a notable approximation. The omitted features found in natural insect wings are known to affect local flow dynamics: for example, leading-edge taper can influence LEV attachment by promoting vortex stability along the span [50]; trailing-edge curvature and spanwise chord variation alter the spanwise pressure gradients, affecting both the distribution of lift and the onset and characteristics of vortex shedding [50]. Such features also modulate tip vortex strength and influence spanwise flow, with implications for overall aerodynamic performance and efficiency [42]. By omitting these complexities, potential effects related to

wing planform-induced flow structures are suppressed, and the experimental results are rendered primarily attributable to temporal and spatial modulations of the prescribed deviation motion.

5.4. FLUID VISCOSITY AND REYNOLDS NUMBER

The original objective of the experimental design was to achieve dynamic similarity with mosquito hovering flight by matching the Reynolds number to approximately 120 [27]. This was to be accomplished by selecting wing dimensions within the spatial constraints of the experimental tank as explained in section 5.3. From the Reynolds number scaling analysis explained in figure 5.2, the optimized kinematic viscosity was identified, and accordingly, it was decided to use a water–glycerol mixture to control the fluid's kinematic viscosity. By adjusting the mixture concentration, the effective viscosity could be increased, thereby enabling Reynolds number scaling without having to significantly alter the geometric or kinematic parameters. However, during preliminary water-based validation trials, several practical challenges with system calibration were identified, such as structural vibrations (explained in Appendix A.6), sensor baseline shifts (explained in Appendix B.2), and alignment issues, all of which required substantial tuning and iterative testing (explained in A.6).

Given the time and resource intensity of preparing and maintaining glycerol mixtures and the operational burden of successive fluid replacement, each involving long drainage, cleaning, and refilling cycles, the experimental protocol was modified. A practical and well-justified decision was made to conduct the final trials in water alone, accepting a moderate departure from the target Reynolds number.

To quantify the resulting Reynolds number after switching from a glycerol mixture to pure water, we compute:

$$\mathrm{Re} = \frac{\rho\, v\, D}{\mu} \tag{5.4}$$

where

$\rho = 1000\,\mathrm{kg/m^3}$	(density of water)
$D = 0.06\,\mathrm{m}$	(characteristic length – wing chord)
$\mu = 0.001002\,\mathrm{kg/(m{\cdot}s)}$	(dynamic viscosity of water at 20°C)

and the velocity v of the wing tip is given by:

$$v = \frac{2 \cdot R \cdot (\theta \cdot \pi / 180)}{T} \tag{5.5}$$

with

$R = 0.24\,\text{m}$	(wing length)
$\theta = 40^\circ$	(sweep amplitude)
$T = 2.76\,\text{s}$	(stroke period)

Substituting the values:

$$v = \frac{2 \cdot 0.24 \cdot \left(\frac{40 \cdot \pi}{180}\right)}{2.7} \approx 0.121\,\text{m/s}$$

Now computing the Reynolds number:

$$\text{Re} = \frac{1000 \cdot 0.121 \cdot 0.06}{0.001002} \approx 7270 \tag{5.6}$$

Although this results in an effective Reynolds number significantly higher than the typical range encountered in mosquito hovering, the unsteady aerodynamic mechanisms under investigation, such as wake capture during stroke reversals, remain qualitatively relevant. Prior studies have shown that, while viscous dominance diminishes at higher Reynolds numbers, key flow structures such as leading-edge vortices, rotational lift, and unsteady wake interactions persist across a broad range of Reynolds conditions [15, 47, 56]. At this moderately high Reynolds number, inertial effects become more pronounced, facilitating the formation of sharper, more coherent vortex cores due to reduced viscous diffusion. Concurrently, stronger convective transport arises, whereby these vortices are advected more efficiently throughout the flapping cycle, enabling them to influence aerodynamic forces over greater distances and timescales.

Quantitative differences in vortex strength, spatial development, and boundary layer characteristics are thus expected at this high Reynolds number. However, conducting the experiment at the biologically relevant Reynolds number of approximately 120 would necessitate much slower wing velocities, resulting in significantly smaller aerodynamic forces, as the aerodynamic forces scale approximately with the square of velocity. By instead operating at a higher Reynolds number of about ~7000, corresponding to increased wing velocity, larger forces are produced that improve the signal-to-noise ratio and measurement fidelity. This approach enhances experimental robustness while maintaining the validity of the key unsteady aerodynamic phenomena under investigation, allowing preservation of the essential physics relevant to mosquito-like flapping flight.

Furthermore, continuing with water alone simplified operational logistics. Unlike glycerol mixtures, which are more expensive, viscous, and prone to potential degradation through mechanisms such as moisture absorption altering concentration and viscosity, microbial contamination, and chemical instability over repeated uses, water allowed

repeated experimental cycles without raising concerns about fluid integrity, sensor fouling, or long-term equipment wear.

Since the primary aim of this study is not to measure absolute force magnitudes but rather to determine how wake capture forces vary with changes in deviation angle, preserving relative trends becomes more critical than exact Reynolds number fidelity. Given that these aerodynamic trends are governed more by flow topology and wake interaction timing than by fine-scale viscous diffusion, the deviation from strict Reynolds number matching can be assumed to not compromise the validity of key findings.

5.5. SHAFT EFFECTS AND FROUDE NUMBER

As discussed in section 4.3.3, the mounting shaft used to support the wing introduces additional hydrodynamic and inertial effects that may influence the measured forces during the experiment. And a series of dry and wet runs were conducted with and without the wing attached, for the decomposition of the total measured forces into contributions from the shaft alone and those resulting from the aerodynamic interaction of the wing with the flow.

Given that the experiment is conducted in a submerged flow environment, it is necessary to consider the role of gravitational forces relative to inertial forces through the dimensionless Froude number, defined as

$$Fr = \frac{v}{\sqrt{gL}}, \tag{5.7}$$

where v is the local flow velocity, g is the gravitational acceleration, and L is a characteristic length scale. In this case, the local flow velocity, v, is estimated by scaling the wing tip velocity by the ratio of the submerged shaft length to the wing length (root to tip). This serves to approximate the characteristic velocity of the fluid near the shaft, acknowledging that only the submerged portion of the shaft interacts hydrodynamically with the surrounding fluid. Thus, the velocity scale is computed as:

$$v = 0.121 \text{ m/s} \times \frac{160}{240} = 0.0807 \text{ m/s}, \tag{5.8}$$

where 160 mm and 240 mm represent the length of the submerged shaft and wing respectively, as shown in figure 4.10.

Note that here $g = 9.81$ m/s^2 and L is defined as the shaft diameter, $L = 0.015$ m. Substituting into the Froude number expression gives:

$$Fr = \frac{0.0807}{\sqrt{9.81 \times 0.015}} \approx 0.208. \tag{5.9}$$

This value is significantly less than unity ($Fr \ll 1$), indicating a subcritical flow regime where gravitational forces dominate over inertial forces. As a result, free-surface effects

are minimal, and the generation of surface waves is expected to be negligible. Consequently, the flow remains relatively stable, and the shaft-induced disturbances are unlikely to introduce significant wave-related artifacts in the force measurements.

Although the free-surface effects from the shaft are negligible, the shaft motion may still induce minor bulk flow disturbances within the interior of the fluid domain. These could include weak, localized vortical structures or low-amplitude oscillatory flows shed from the shaft surface. However, such effects are expected to be extremely small in magnitude, as confirmed by the wet runs conducted with the shaft alone, which showed negligible force signatures beyond the baseline measurement noise (See Appendix B.1.1 and B.1.2). Consequently, any shaft-induced bulk flow influence on the aerodynamic loading of the wing can be considered insignificant for the present study.

5.6. DOMINANCE OF PRESSURE FORCES OVER VISCOUS SHEAR FORCES

In the quasi-steady aerodynamic model employed in this study, the entire force estimation framework is built upon the assumption that the dominant contribution to the aerodynamic loading on the wing arises from the pressure-induced normal force. This modeling simplification neglects viscous shear stresses along the wing surface, based on prior computational and experimental investigations which have demonstrated that viscous forces typically constitute less than 5% of the total aerodynamic force in comparable flapping-wing regimes [19, 18, 33]. Consequently, aerodynamic forces are treated as acting normal to the instantaneous wing surface, reflecting the predominance of unsteady pressure fields in driving force generation at moderate to high Reynolds numbers. This assumption simplifies the force decomposition in the co-rotating wing-fixed reference frame and facilitates transformation into the global coordinate system, where only the resolved normal components contribute to the net lift and drag calculations. The same assumption is extended to the experimental analysis: total force measurements acquired from the load cell are projected onto the local normal direction of the wing during transformation, under the premise that shear-driven tangential forces are negligible. While this introduces a minor approximation, it remains justified within the operating Reynolds number regime of the experiment and aligns with established aerodynamic behavior of thin, rigid wings undergoing unsteady flapping [49].

Although the experimental Reynolds number in this study (Re $\approx$ 7000) is substantially higher than typical values encountered in classical insect flight regimes, the assumption of negligible viscous forces remains appropriate for two key reasons. First, as Reynolds number increases, the relative influence of viscous shear stresses on the overall aerodynamic force diminishes because the boundary layer thickness decreases and inertial (pressure) forces become increasingly dominant [24]. Second, the experimental wing is a rigid, smooth, thin-profile surface operating in an unsteady, oscillatory flow regime, conditions under which unsteady pressure gradients, including added mass and rotational effects, are the primary contributors to force production. While viscous dissipation may influence fine-scale near-wall phenomena such as separation onset or boundary layer development, its contribution to the net aerodynamic force, particularly in lift and thrust directions, is minimal [56].

In terms of direct evidence from the present measurements, viscous effects can be indirectly inferred as minimal by the consistency and repeatability of the force signals projected onto the normal direction, as well as by the appreciable agreement between experimentally measured forces and quasi-steady model predictions based predominantly on pressure force components. Notably, tangential force components (denoted as F_y) were recorded during the experiments and were found to be very small - close to zero - and exhibited negligible variation across the range of deviation angles tested. This observation substantiates the assumption that viscous shear forces, which manifest as tangential stresses, contribute insignificantly to the overall aerodynamic force compared to pressure-induced normal forces.

5.7. TREATMENT OF BUOYANCY AND SIDE FORCE IN ANALYSIS

In the present experimental setup, the wing is submerged vertically into a fluid tank with its spanwise axis oriented downward. This orientation causes the buoyant force, resulting from hydrostatic pressure, to act upward along the spanwise direction. When the measured forces are resolved into the global coordinate frame, this buoyant contribution is primarily reflected in the side force component, which aligns with the wing's span. Notably, this effect is not present in the quasi-steady aerodynamic model, which neglects hydrostatic influences and only accounts for pressure-driven aerodynamic forces.

To maintain consistency between experimental and modeled results, and to focus on the primary aerodynamic quantities of interest, which is the lift and drag forces, the buoyancy effect was not corrected in post-processing. Empirical observations, discussed in Appendix B.1, confirmed that the buoyant offset had negligible influence on the time-varying chordwise and normal force components - those directly contributing to aerodynamic lift and thrust. Its influence was limited to the spanwise (side force) direction, as expected from the flapping orientation.

This simplification allows for a cleaner comparison between experimental and quasi-steady model results by focusing on components that are theoretically meaningful for this study. Furthermore, excluding the side force is consistent with the assumption of pressure-dominated normal loading and avoids introducing unnecessary corrections for hydrostatic forces that do not influence the core aerodynamic mechanisms under investigation. As such, buoyancy is acknowledged as a secondary effect in this configuration and is excluded from the present aerodynamic force analysis.

5.8. STROKE-SYMMETRY AND AVERAGING OF FORCE PROFILES

During this study, each experimental recording captures the aerodynamic force profile corresponding to a complete flapping cycle, defined as one downstroke followed by one upstroke. Detailed examination of the time-resolved force data revealed that the force profiles exhibit pronounced symmetry between the downstroke and upstroke phases. Specifically, the drag force during the upstroke appears as a sign-inverted mirror image of the downstroke drag force, while the lift forces in both phases display nearly identical trends with respect to magnitude and temporal evolution. The symmetry in the drag

force profiles is especially significant in the context of hovering flight. For true hovering, the net drag force over a complete cycle should be zero; otherwise, a net thrust would be generated, contradicting the hovering condition. The experimental data confirm this expectation, as the drag forces are nearly symmetric but of opposite sign across the two halfcycles. This outcome aligns well with theoretical predictions and serves as a validation of both the experimental kinematics and the force measurement methodology.

This empirical symmetry can be traced to the underlying kinematic protocol: the prescribed wing motion is governed by pure sinusoidal variation in the Euler angles (sweep, deviation, and pitch), imparting temporal and spatial symmetry to the wing trajectories within each cycle. For sinusoidal kinematics, the geometric and velocity conditions traversed during the downstroke are retraced during the upstroke, albeit in the opposite direction, resulting in theoretically equivalent, though sign-adjusted, aerodynamic loading. This behavior is consistent with classical unsteady aerodynamics, wherein symmetric, periodic kinematics yield force histories that are likewise temporally symmetric about the cycle midpoint [21][15][49], except for direction-dependent components such as drag.

Given this strong symmetry, the decision was made to utilize both the upstroke and downstroke data in the analysis, treating them as statistically equivalent and averaging their respective force profiles at each corresponding phase of the cycle. This approach is grounded in established statistical and experimental methodology, wherein pooling symmetric data effectively doubles the sample size and thus reduces random experimental variation through averaging [5][39]. By incorporating data from both halves of the flapping cycle, the resultant force trends exhibit improved signal-to-noise ratio and enhanced statistical reliability, minimizing the impact of cycle-to-cycle fluctuations or transient disturbances.

5.9. SECONDARY UNSTEADY EFFECTS DURING HYDRODYNAMIC FORCE ISOLATION

In isolating the hydrodynamic forces acting solely on the wing, the methodology relies on systematically subtracting force measurements obtained from a series of dry and wet runs, as described in Section 4.3.3. This procedure sequentially removes contributions from the shaft and inertial effects common to all configurations, so that the residual signal represents primarily the net hydrodynamic loads generated by the wing during flapping.

However, this subtraction procedure, while practical, may inadvertently encapsulate additional complex unsteady or nonlinear phenomena that are not strictly part of the ideal hydrodynamic force on the wing. For instance, small-scale background turbulence generated by the shaft, or coupled fluid–structure vibrations might exert subtle influences which, although present in both the wing and shaft-alone cases, are not perfectly replicated across all runs due to slight variations in flow history or apparatus dynamics. Transient wake–shaft interactions, minute asymmetries in mounting, or imperfect repeatability in shaft immersion could also introduce nonlinear artifacts that are algebraically

trapped within the isolated force signal following subtraction. Furthermore, any slight mismatches in synchronization between wet and dry runs, especially for low-magnitude or high-frequency forces, could allow residual sensor drift, vibrational noise, or system hysteresis to project onto the final hydrodynamic force traces.

Despite these possibilities, subtraction-based isolation remains the most rigorous and experimentally tractable method available within the constraints of the present setup. The experimental design - incorporating repeated trials, rigorous pre- and post-trial baseline corrections, and averaging across multiple cycles - substantially suppresses non-hydrodynamic artefacts and minimises both random and systematic errors. Accordingly, while the potential inclusion of minor unsteady or nonlinear effects should be recognised in interpreting absolute force magnitudes, the method provides reliable and physically meaningful comparative metrics for analysing hydrodynamic force generation across tested conditions.

5.10. UNCERTAINTY IN FORCE SENSOR MEASUREMENTS

During post-processing of the wake capture force data, substantial scatter and anomalous peaks were observed across various deviation angles, prompting a detailed uncertainty analysis to assess the robustness of the measurements. Static runs of the force-torque sensor also indicated a baseline noise of approximately 0.3 N, accompanied by low-frequency drift as shown in figure 5.3 (explained further in Appendix B.2).

Accordingly, individual uncertainty levels (RMS Standard deviation / $\sqrt{5}$) for each deviation angle were quantified for the wet and dry experimental conditions, namely, Air+Wing+Shaft, Air+Shaft, Water+Wing+Shaft, and Water+Shaft, as illustrated in figure 5.4. The typical uncertainty ranged between 0.1 N and 0.2 N, with a pronounced spike near 3.5° deviation angle in the Air+Shaft case.

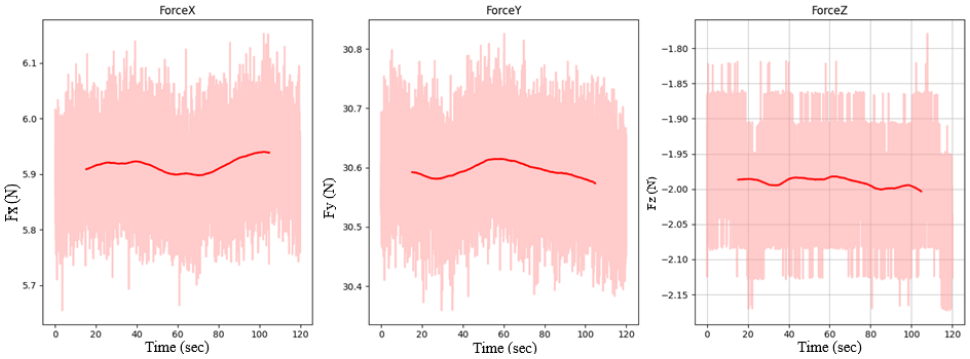

Figure 5.3: Variation of force reading during a 120 second static trials. Here we see a baseline noise of approximately 0.3 N, accompanied by low-frequency drift.

To estimate the combined experimental uncertainty for each deviation, the root-sum-square (RSS) of the uncertainties from these four independent runs was computed using

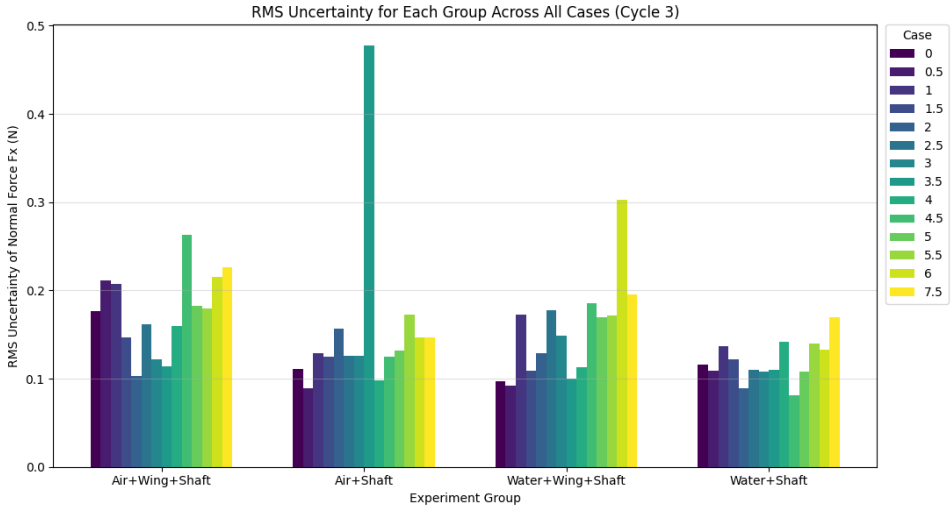

Figure 5.4: RMS uncertainty of the Fx (normal force on the wing) for each experimental group across all tested deviation angle cases during the middle cycle. The grouped bar chart compares uncertainty in Fx for four setups: Air+Wing+Shaft, Air+Shaft, Water+Wing+Shaft, and Water+Shaft, while each color represents a different deviation angle case, ranging from 0° to 7.5°. The typical RMS uncertainty ranged between 0.1 N and 0.2 N, with a pronounced spike near 3.5° in the Air+Shaft case

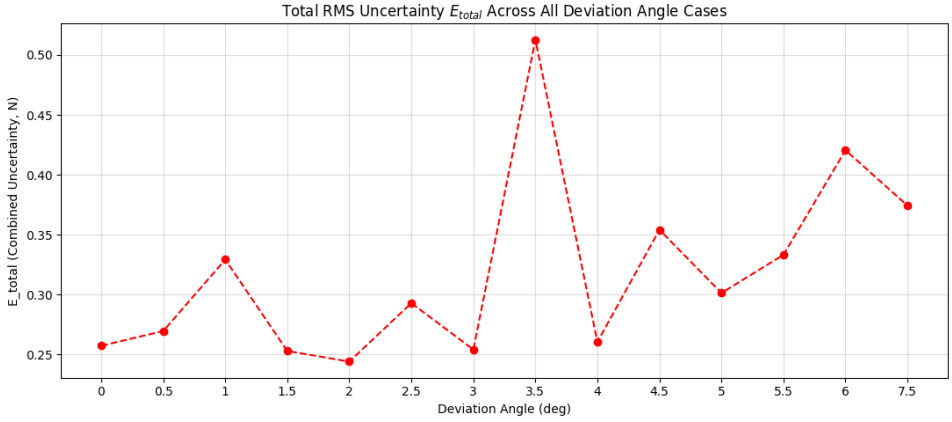

Figure 5.5: Total RMS uncertainty E_{total} in wake capture force measurement as a function of deviation angle. The plot quantifies combined experimental uncertainty (in newtons) across the tested range, highlighting a pronounced peak near 3.5°, which denotes increased uncertainty in the results at this deviation angle.

the equation 5.10, yielding the total RMS error profile shown in figure 5.5.

$$E_{\text{total}} = \sqrt{E_1^2 + E_2^2 + E_3^2 + E_4^2} \tag{5.10}$$

where

E_1 = uncertainty from the experimental case: Air + Wing
E_2 = uncertainty from the experimental case: Air + Shaft
E_3 = uncertainty from the experimental case: Water + Wing
E_4 = uncertainty from the experimental case: Water + Shaft

Notably, in figure 5.5, the aggregate uncertainty was found to be ~0.3 N at lower deviation angles and shows an increasing trend above 4.5°, with the 3.5° case exhibiting a dominant outlier. This pronounced outlier at 3.5° implies that we can expect a spurious result in the wake capture plot corresponding to the 3.5° deviation angle, and any interpretation of this point should be made with caution due to the elevated measurement uncertainty.

The uncertainty levels identified in this analysis represent a slight overestimation and can be considered upper bounds. This overestimation arises because the analysis is based on a sample size of five trials, while the actual dataset includes multiple cycles per trial and averages over second half-cycles, effectively increasing the effective sample size. Additionally, the application of filtering during data processing further reduces noise and uncertainty. Therefore, the reported uncertainty values are somewhat overstated relative to the true measurement variability; however, this does not justify disregarding the uncertainty present.

Thus, these findings indicate that some apparent force variations and peak phenomena in the wake capture data may arise in part from high measurement uncertainty rather than purely physical effects. As replacing the force sensor was not feasible within the experimental schedule, it is necessary to explicitly acknowledge this sensor-induced uncertainty when interpreting trends and drawing conclusions from the hydrodynamic force results.

6

RESULTS AND DISCUSSIONS

6.1. EXPERIMENTAL RESULTS

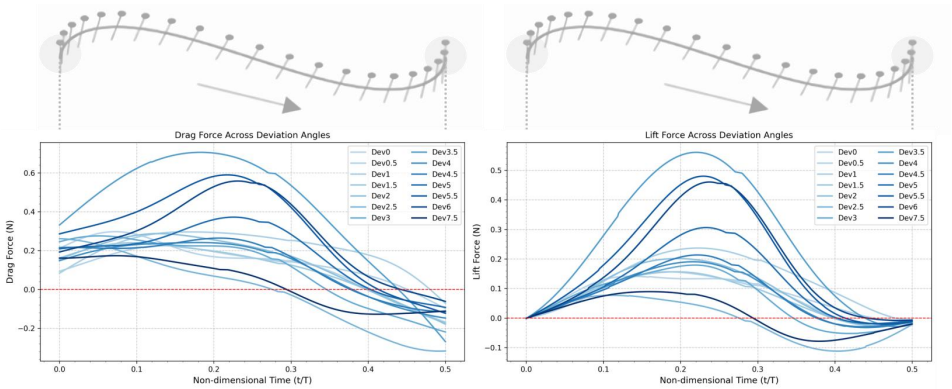

Figure 6.1: Variation of the Transformed Drag (left) and Lift Forces (right) from experiments across a flapping half cycle for different deviation angles, with lighter colours indicating lower deviation angles and darker colours indicating higher deviation angles; the line-and-dot schematic above the plots illustrates the corresponding wing motion and rotation during the half cycle, where the line represents the wing chord and the dot marks the position of the leading edge. The schematic is illustrative; angles are not to scale.

An examination of the experimentally measured Drag and Lift force profiles, as depicted in Figure 6.1, indicates that both force components exhibit broadly similar temporal patterns across all tested deviation angles, although the magnitude and amplitude of the forces vary between cases. The underlying cause of this shared qualitative behaviour is presumably associated with the inherent symmetry and repeatability imposed by the controlled sinusoidal figure-eight kinematics of the experiment. Nevertheless, notable quantitative differences in force responses are evident as the deviation angle is systematically varied.

Small *kinks* are observed in the drag and lift force curves at $t/T \approx 0.26$. These artifacts arise due to gaps or irregularities in the raw experimental time data, which cause minor misalignments in the processed force signals after filtering and transformation (explained in Appendix A.5).

In this section, the physical mechanisms underlying the evolution of Drag and Lift are discussed in turn, with reference to pertinent unsteady aerodynamic theory.

6.1.1. ANALYSIS OF DRAG AND LIFT FORCE ACROSS DEVIATION ANGLES

DRAG FORCE EVOLUTION

A common feature across all deviation angles is the observation that Drag force at the onset of the half-stroke ($t/T \approx 0$) initiates from a small but positive, non-zero value. This could plausibly be attributed primarily to unsteady inertial effects. Specifically, as the wing commences flapping from rest, it must instantaneously accelerate the surrounding fluid, giving rise to an added mass (virtual mass) reaction force [24, 18, 49]:

$$F_{\text{added mass}} = -m_a \frac{dU}{dt}, \tag{6.1}$$

where m_a denotes the added mass associated with the displaced fluid, and $\frac{dU}{dt}$ the instantaneous acceleration of the wing. The immediate establishment of a pressure gradient as the wing begins moving, combined with possible slight residual flows remaining from prior cycles, could also contribute to this initial offset. While this is consistent with unsteady aerodynamic principles, alternative minor sources such as sensor offset or unresolved baseline drift cannot be ruled out, though these are considered to be controlled in the present setup (see Appendix B.2).

As the stroke progresses, Drag force consistently increases for most deviation cases, with a pronounced peak located near $t/T \approx 0.25$. The physical causes for this behaviour are likely multifactorial. At approximately mid-stroke, the kinematics result in the highest translational velocity reached by the wing, such that the quadratic velocity dependence of aerodynamic forces becomes significant:

$$F_D \propto \frac{1}{2}\rho U^2 C_D, \tag{6.2}$$

where F_D is the Drag, ρ is the fluid density, U is local velocity, and C_D is the drag coefficient [48, 56]. Greater deviation angles introduce a stronger out-of-plane (vertical) component of this velocity, which increases the effective angle of attack and the frontal area exposed to the incoming flow. This may augment C_D due to the increased pressure differential across the wing [27, 33]. Unsteady inertial effects, particularly those arising from nonlinear accelerations and the geometrical coupling between pitching and deviating motions, are also expected to be amplified at large deviation amplitudes, thereby further increasing the total drag force [18].

For cases with smaller deviation angles ($\theta \lesssim 1°$), the drag profile tends to remain relatively flat until about $t/T \approx 0.3$. This phenomenology could be accounted for by the near-planar kinematics, meaning that out-of-plane effects are midly expressed: the orientation of the wing remains close to the stroke plane, moderation changes in effective angle of attack, and frontal area, resulting in drag being more stable and dominated by steady translational effects, with unsteady amplifications less apparent.

Towards the termination of the half-stroke ($t/T \to 0.5$), all profiles display a transition of drag force into negative values. This reversal is most likely related to inertial (added mass) and possibly pressure recovery effects as the wing rapidly decelerates. As the wing slows at the end of the stroke, the entrained fluid, possessing inertia, may act on the rear of the wing, generating a force in the direction opposite to its previous motion [48, 24]. This is qualitatively consistent with the expected dynamics of fluid-structure interaction in unsteady flapping — a scenario where the added mass force changes sign upon deceleration:

$$F_{\text{added mass}} = -m_a \frac{dU}{dt} \xrightarrow[\text{deceleration}]{} \text{negative}, \tag{6.3}$$

Such a response is expected to be more pronounced for higher deviation angles, where out-of-plane velocities and accelerations are greater. While this explanation follows from well-established theory, alternative or complementary contributions from pressure recovery, transient vortex shedding, or measurement uncertainty cannot be absolutely excluded.

LIFT FORCE EVOLUTION

At the outset of the half-stroke ($t/T = 0$), the lift force for all deviation angles initiates at or near zero. This behavior is physically plausible because, at this particular instant, the wing's chord is nearly aligned with the instantaneous trajectory of motion, and the wing velocity is minimal as a result of sinusoidal kinematics. Under such circumstances, the effective angle of attack, defined by the geometric relationship between the wing chord and the local flow velocity, is very small, causing bound circulation around the wing to be minimal and suppressing the generation of pressure differentials that would otherwise produce lift [19, 56]. Additionally, the quasi-stasis at stroke reversal means that any inertial (added mass) contributions to the lift component are also close to zero, given that the net acceleration along the lift direction is momentarily balanced.

As the cycle progresses from $t/T = 0$, the lift force rises rapidly, reaching a pronounced peak at approximately $t/T \approx 0.25$. This increase coincides with the wing accelerating to its maximum translational velocity at mid-stroke, a direct result of the sinusoidal variation of the stroke and deviation angles. According to fundamental aerodynamic theory, the instantaneous lift force generated by a moving wing section is proportional to the square of the local velocity component normal to the chord, and to the effective coefficient of lift, C_L (see [15, 23]):

$$L(t) = \frac{1}{2}\rho U^2(t) S C_L(t) \tag{6.4}$$

where $U(t)$ denotes the instantaneous velocity of the wing relative to the fluid, S is the effective wing area, and $C_L(t)$ is the time-dependent lift coefficient. Thus, at mid-stroke, where $U(t)$ is maximized, the lift force correspondingly peaks.

The sharp increase in C_L arises from the combined effect of the translational component and the effective angle of attack. When the effective angle of attack becomes sufficiently large (as can result from both the upsurge in velocity and deviation angle), the formation and stabilization of a leading-edge vortex (LEV) may occur. The LEV has been shown, both in classical experiments and contemporary computational models, to enhance the bound circulation around the wing by sustaining a low-pressure region above the wing surface [19, 47]. This sustained circulation, associated with the LEV, directly augments the lift force in accordance with the Kutta–Joukowski theorem:

$$L' = \rho U \Gamma \tag{6.5}$$

where L' is the sectional lift per unit span, U is the local velocity, and Γ is the bound circulation about the wing.

For higher deviation angles, the three-dimensionality of the wing trajectory can further influence both the development and stability of the LEV and the overall bound circulation, potentially modulating the timing and amplitude of the lift force peak. For moderate deviation angles, these effects may enhance lift by stabilizing the LEV and preserving favourable spanwise flow patterns [27, 33]. However, to conclusively verify these aerodynamic behaviors, detailed flow visualization techniques such as particle image velocimetry (PIV) are necessary to directly observe and quantify the flow interactions involved.

Beyond the peak at mid-stroke, the lift force typically exhibits a steady decline. This reduction is primarily a consequence of two related effects: as the wing approaches the end of the half-stroke, its translational velocity diminishes due to sinusoidal reversal, lowering the U^2 term that governs dynamic pressure. Concurrently, the effective angle of attack may also decrease or become less favourably aligned with the velocity vector, further diminishing both C_L and the net bound circulation. In some regimes, the progressive growth of the trailing-edge vortex and eventual detachment (or shedding) of the LEV, known from experimental studies, might also reduces the lift-producing circulation [19, 16, 47].

An additional feature observed in the experimental lift profiles is the brief excursion to negative values just before the end of the half-stroke, typically between $t/T \approx 0.4$ and $t/T \approx 0.5$. Several mechanisms could plausibly explain this negative peak. First, as the wing decelerates in preparation for stroke reversal, the added mass (or fluid-inertia) forces may become negative, contributing a transient downward force [48, 15]. This effect is expressed equation 6.3, where the sign reversal as $dU/dt < 0$ during deceleration momentarily opposes the direction of lift. Second, as the wing decelerates, it may

encounter adverse flow fields—for example, the induced downwash from the wake or residual vortex structures produced earlier in the stroke [34, 47]. These interactions can reduce the effective angle of attack (sometimes even rendering it negative), leading to the observed downward force at this late stage of the stroke [47].

Finally, as the cycle completes, velocity and acceleration return to zero, and the lift force profile resets in anticipation of the next half-stroke. This symmetry across half-strokes is a generic consequence of the prescribed sinusoidal kinematics and the quasi-periodicity of the force generating mechanisms.

DRAG AND LIFT AS A FUNCTION OF DEVIATION ANGLE

In order to facilitate a systematic comparison across different wing deviation angles, the experimentally measured force profiles, specifically drag and lift, were condensed into single representative values for each case. This was accomplished by computing the mean value of the force profile over the flapping cycle for both drag and lift components.

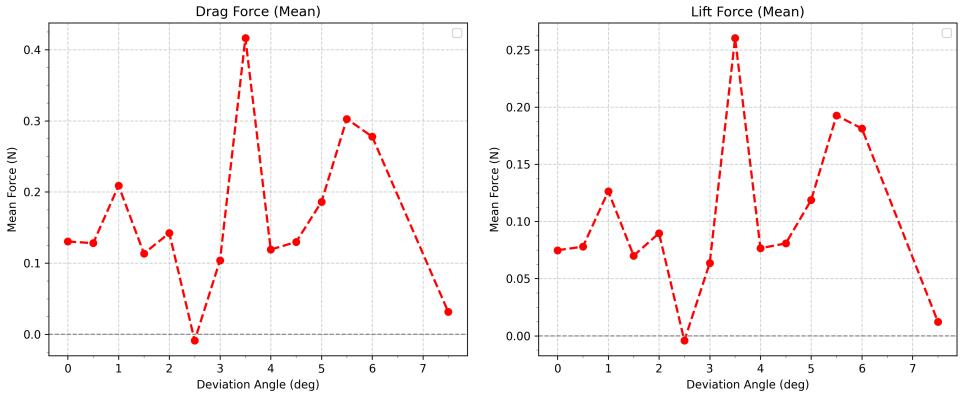

Figure 6.2: Variation of mean experimental drag force (left) and lift force (right), as functions of deviation angle.

The mean drag and lift forces measured across a range of deviation angles, as depicted in the provided figure 6.2, exhibit a distinctly non-monotonic and nonlinear response that resists simple characterization. Both force components generally follow similar trends with deviation angle, which is unsurprising given their shared dependence on instantaneous wing kinematics and local flow structures during the flapping cycle.

At lower deviation angles ($\theta \approx 0°$–$2°$), both forces remain relatively steady, fluctuating minimally around a baseline value, which may be indicative of primarily planar kinematics where the wing's trajectory maintains close proximity to its previous wake. The minimal sensitivity of the mean forces in this region aligns with previous findings [27], that for moderate or small out-of-plane excursions, the primary aerodynamic mechanisms remain dominated by classical leading-edge vortex (LEV) formation and quasi-steady translational contributions, with wake capture serving as a secondary modulator.

A pronounced drop in both drag and lift at about $\theta \approx 2.5°$ deviation likely marks a transition in wake interaction. An apparent phase mismatch between the orientation of the wing and the wake-vortex might diminish wake-induced force enhancement, suppressing lift and drag peaks. However, given the elevated measurement uncertainty in the measured data, this observed reduction may partly reflect experimental variability and should be cautiously interpreted.

Following this dip, the data reveal an immediate and substantial peak at $\theta \approx 3.5°$, with both drag and lift momentarily reaching their highest measured mean values. This spike could plausibly be linked to a constructive synchronization between the increased out-of-plane motion and the spatial evolution of the wake, wherein the wing re-engages with a region of high-circulation vortices at an opportune phase of the stroke. Contemporary studies in unsteady flapping flight point to such phase-dependent enhancements, especially when trajectory variables (like deviation or phase lag between stroke and deviation) promote optimal overlap between the wing and its own wake [32]. However, the narrowness and immediacy of this peak actually reflect the extreme measurement uncertainty at $\theta = 3.5°$ as pointed out earlier in the section 5.10; thus, this apparent peak is likely an artifact of experimental noise/vibration rather than a true physical effect.

Beyond this isolated maximum, a period of relative force quiescence appears until $\theta \approx 4°$, suggesting that the system traverses another transitional interval—possibly one where the spatial or temporal offsets between the wing and its shed wake minimize their aerodynamic coupling. Notably, starting from $\theta \approx 4°$, both drag and lift again begin to climb, now following a more consistent upward trajectory until $\theta \approx 6°$. This renewed increase might be attributed to a threshold effect in three-dimensional wake topology: as deviation angle grows, the wing's path becomes increasingly non-planar, potentially intersecting regions of the wake previously unexploited at lower deviation values. Such behavior has been noted in high-amplitude heaving, where larger vertical excursions convect the wake further from the stroke plane [27]; with continued deviation increase, the wing may eventually re-cross the wake, enabling further interactions. However, again due to the high uncertainty, this trend may simply be an artifact.

Furthermore, the pronounced drop in both forces immediately after the peak at $\theta \approx 6°$ could reflect either a true aerodynamic phenomenon, such as the wing's deviation exceeding the optimal range for effective wake interaction, or the onset of adverse 3D flow effects like vortex detachment, or simply arise from increased measurement uncertainty and system limitations near the robot's operating extremes.

It is, however, essential to consider the experimental context, particularly the high Reynolds number (Re ≈ 7,000) used in these trials, significantly above the biologically typical regime for mosquito flight (Re ≈ 120). At elevated Reynolds numbers, viscous effects are diminished and inertial effects dominate, leading to sharper, more coherent vortical structures with less pronounced dissipation between cycles. Such conditions may facilitate stronger, more persistent wake structures, which could explain the magnitude and abrupt-

ness of the observed lift and drag events. Conversely, it is important to recognize that the observed local maxima and minima in force signals may also be influenced by factors related to measurement uncertainty, persistent noise and vibration in the sensor data, and subtle misalignments or mechanical inconsistencies within the robotic apparatus.

In summary, while some features in the observed trends, such as periodic enhancements and suppressions, can be theoretically rationalized as consequences of phase-dependent wake capture and three-dimensional vortex–wing interplay, it is equally plausible that the observed peaks and trends are more strongly influenced by the relatively high uncertainty inherent in the force measurements, apart from the high reynolds number regime that the experimented is operating in. Thus, while fluid dynamic phenomena may provide a partial explanation for the behavior, caution is warranted in interpreting these results. Therefore, robust conclusions require further validation through more controlled studies, including advanced flow visualization (e.g., PIV), the use of a more robust apparatus designed to minimize noise and vibration, and careful tuning of the experimental setup to accurately match the relevant Reynolds number regime, to fully disentangle physical effects from experimental uncertainties.

6.2. QUASI-STEADY MODEL RESULTS

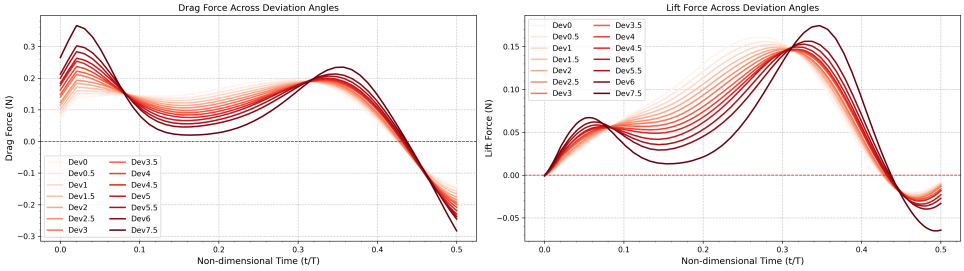

Figure 6.3: Variation of the Transformed Drag (Left) and Lift (Right) Forces from QS Model, across a flapping half cycle, for different deviation angles. Lighter Shades correspond to lower deviation angles and the darker shades correspond to higher deviation angles.

The kinematic data obtained from the Staubli robot for each deviation angle was input into the quasi-steady (QS) model to compute the transformed aerodynamic forces shown in the attached figure. While the QS model predictions exhibit notable differences from the experimentally measured forces, a key similarity remains: both the lift and drag forces display symmetry across the two half-strokes, which lends credibility to the modeled results. To gain a deeper understanding of the underlying force behavior, it became essential to examine the individual force components, namely translational, added mass, rotational, and coupling forces, that collectively contribute to the total aerodynamic force.

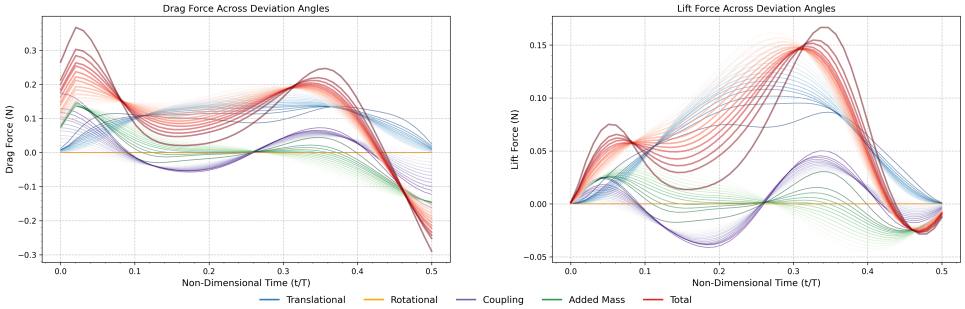

Figure 6.4: Force Composition of the Drag Force (Left) and the Lift Force (Right) from QS Model. Here the lighter colours correspond to the lower deviation angles and darker colours correspond to higher deviation angles.

6.2.1. FORCE COMPOSITION AND ANALYSIS

Figure 6.4 illustrates the variation of different force components - namely, translational, rotational, coupling, and added mass forces - across a range of deviation angles during a flapping half cycle, as predicted by the quasi-steady (QS) model. An immediate observation from both the drag and lift subplots is that the rotational force component (yellow) is nearly zero throughout the cycle for all deviation angles. This is physically expected: for perfectly sinusoidal pitch kinematics, angular acceleration is symmetric about the stroke midpoint, and as a result, the net rotational contribution cancels out across the cycle, confirming that the model is faithfully representing the inertial forces induced by pitching. A notable feature in the figure 6.4 is the "kink" at the start and end of the added mass force profile, propagating into the total force. As mentioned before in section 4.4.2, this is most likely a numerical artifact of the quasi-steady equations and their discrete implementation in MATLAB.

Focusing on the lift force (right panel) in figure 6.4, the total lift is clearly dominated by the translational component (blue), especially at the primary peak around $t/T \approx 0.3$. As deviation angle increases, we observe a steady decrease in this translational lift contribution—which results in a reduction in the overall lift amplitude. Notably, there is also an observed inversion of this trend at t/T = 0.11 and t/T = 0.36. This pattern can be interpreted as the onset of significant contributions from unsteady inertial mechanisms, the added mass (green) and coupling (purple) terms, which start to offset the loss in translational lift at high deviation angles.

Closer inspection of the component curves reveals that both coupling and added mass forces increase in amplitude with deviation angle, peaking near $t/T \approx 0.35$, just after the translational maximum. These two forces arise from non-circulatory (inertial) effects: the added mass force is the fluid's reaction to the wing's normal acceleration, while the coupling force results from interactions between pitching and deviation (heaving) motions. In this sinusoidal flapping kinematic regime, both exhibit characteristic sinusoidal patterns: two positive and two negative peaks per stroke, corresponding to significant acceleration and deceleration phases.

The sharp positive peaks in added mass and coupling near $t/T \approx 0.35$ coincide with the wing decelerating rapidly at the end of the downstroke—here, higher deviation angles amplify normal accelerations and therefore generate larger inertial forces, boosting lift. Shortly after, both inertial components transition to pronounced negative peaks as the wing slows and reverses, transiently reducing the total lift at stroke completion.

A secondary lift peak is observed at $t/T \approx 0.05$, this time growing monotonically with increasing deviation angle. Early in the stroke, larger deviation induces greater upward accelerations and out-of-plane motion, directly amplifying both the added mass and coupling contributions. The effect is most pronounced just after stroke initiation, but rapidly diminishes as acceleration subsides, sometimes leading to negative values when the wing's acceleration reverses toward mid-stroke.

It is important to note that the QS model calculates forces based on instantaneous kinematics and does not capture wake-induced velocity fields (downwash) or the full dynamics of three-dimensional vortex formation and interaction. However, the model's predicted trends echo established aerodynamic phenomena: as deviation angle increases, one expects greater three-dimensionality and potential downwash effects, which in a real, unsteady flow would reduce the effective angle of attack and thus decrease lift, at least initially. The recovery of lift at higher deviation angles, as seen here, can therefore be attributed, in the QS model, to the growing dominance of inertial (non-circulatory) forces at high acceleration.

Thus, figure 6.4 demonstrates that, within the limitations of the quasi-steady approach, the interplay between translational and unsteady inertial (added mass and coupling) forces determines the complex, non-monotonic variation of lift with deviation angle, particularly at larger amplitudes where inertial contributions become significant.

Examining the drag force components in Figure 6.4 (left panel), we observe that the translational drag (blue) remains relatively steady and exhibits a broad, plateau-like profile for most of the half stroke. This reflects how, under quasi-steady assumptions, the drag arising from instantaneous wing velocity and angle of attack changes little during the central portion of the cycle, with modest variation as wing velocity and orientation co-evolve sinusoidally. In contrast, the coupling (purple) and added mass (green) components show marked temporal variation, each producing two distinct positive peaks, one immediately after stroke initiation ($t/T \approx 0.02$) and another before stroke reversal ($t/T \approx 0.35$), as well as two intervening negative peaks near $t/T \approx 0.12$ and at the end of the half-cycle ($t/T = 0.5$). These features arise because both inertial terms are tightly linked to the wing's acceleration: positive peaks correspond to phases where the wing is rapidly accelerating in the direction of motion, resulting in constructive addition to total drag, while the negative peaks capture periods of rapid deceleration, where inertial reactions transiently oppose the direction of motion and thus reduce or even momentarily reverse drag. This cycling of added mass and coupling contributions, strongest near the start and end of the half-stroke, not only modulates the total drag force magnitude but also reflects the fundamental dynamics of flapping propulsion, where fluid inertia plays an outsized role during rapid directional changes.

6.3. WAKE CAPTURE

The figure 6.5 presents the transformed experimental force data overlaid with the predictions from the quasi-steady (QS) model. A noticeable discrepancy is observed between the two, which is attributed to the presence of wake capture effects in the experimental results, phenomena that the QS model inherently does not account for.

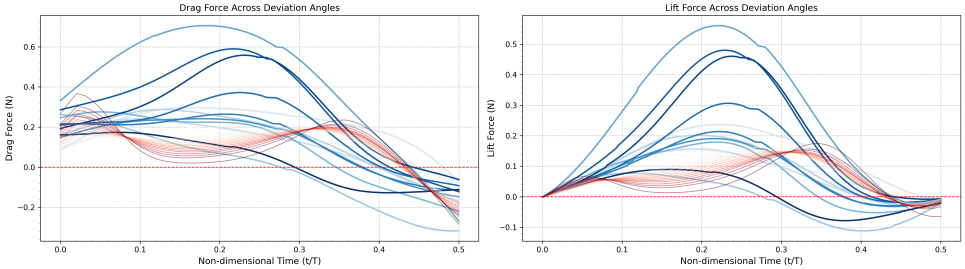

Figure 6.5: Comparison of Experimental Forces (Blue) against the QS Model Forces (Red) across a flapping half cycle, for different deviation angles. Here, the lighter shades correspond to the lower deviation angles and the darker shades correspond to higher deviation angles.

The figure 6.6 illustrates the wake capture forces, defined as the difference between the experimental data and the quasi-steady (QS) model predictions, for a range of deviation angles over the stroke halfcycle.

Upon analysing the wake capture lift forces shown in the right panel of Figure 6.6 (as well as the 3D surface plot in Figure 6.7), a pronounced positive peak in wake capture is observed near $t/T = 0.21$, approximately mid-downstroke. This coincides with the instant of peak translational velocity, when the wing's trajectory possibly intersects the convected vortical structures shed during the previous cycle. The resulting vortex-wing interaction locally enhances the effective angle of attack, transiently boosting lift beyond quasi-steady predictions.

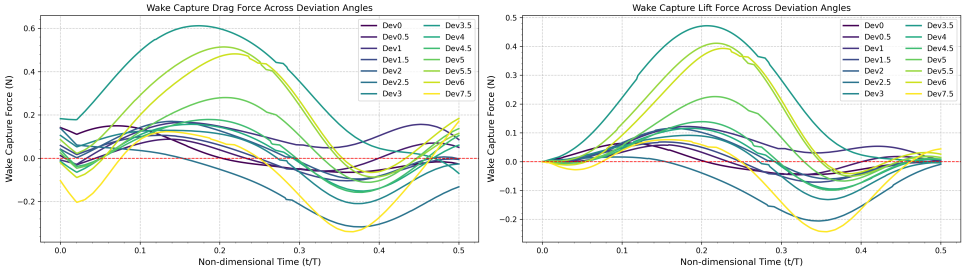

Figure 6.6: Wake Capture Drag (left) and Lift (Right) Forces, across a flapping half cycle for different deviation angles, obtained by subtracting the QS Model forces from the Experimental Forces

A smaller negative peak occurs near $t/T \approx 0.35$, just before stroke reversal. This fea-

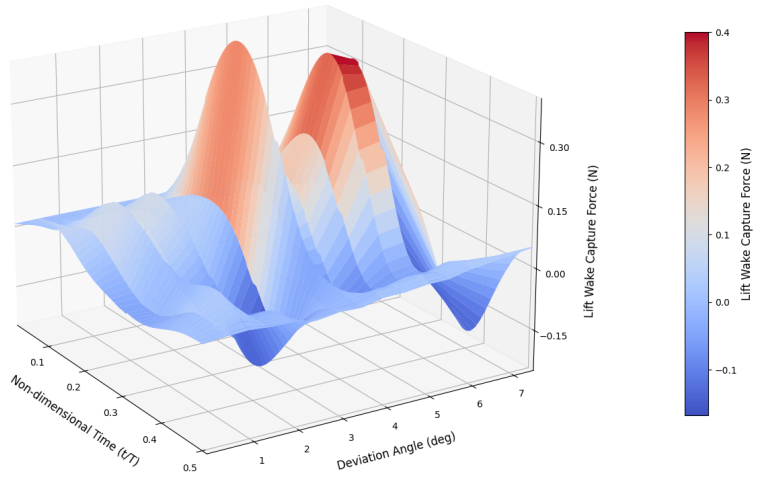

(a) Lift Wake Capture Forces as functions of non-dimensionalised time (t/T) and deviation angle (degrees)

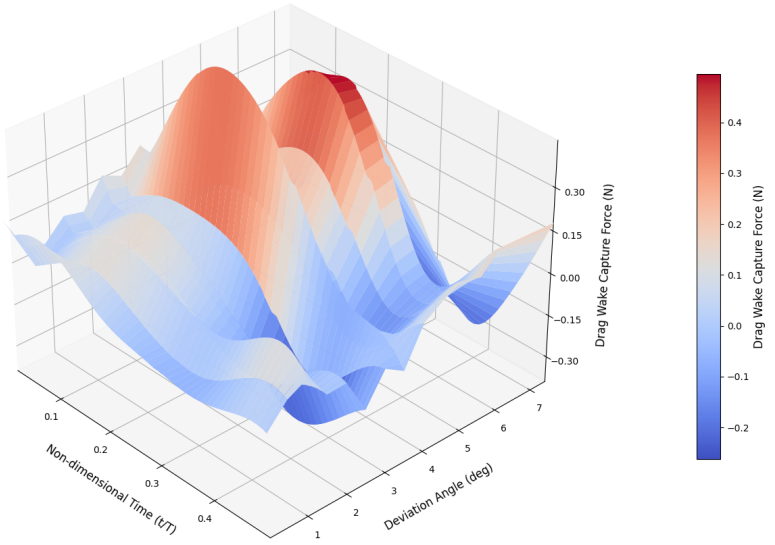

(b) Drag Wake Capture Forces as functions of non-dimensionalised time (t/T) and deviation angle (degrees)

Figure 6.7: 3D surface plots of wake capture forces (N) as functions of non-dimensionalised time (t/T) and deviation angle (degrees). Colour contours indicate the instantaneous force amplitudes, with pronounced maxima at specific stroke phases and deviation angles, highlighting the phase-dependent nature of wake capture effects in flapping flight.(a) Lift wake capture forces. (b) Drag wake capture forces.

ture could be attributed to unsteady wing–wake interactions that are not captured by the quasi-steady model. As the wing rapidly decelerates, it re-enters the region influenced by its own shed wake, encountering localized downwash and vortex-induced flow structures. These unsteady wake effects act against the bound circulation by reducing the effective angle of attack, thereby diminishing the aerodynamic lift force. This highlights the role of phase-dependent vortex-wing interactions during deceleration, where the timing and spatial arrangement of the shed vortices relative to the wing modulate the instantaneous aerodynamic forces.

Turning to the wake capture drag forces shown in the left panel of Figure 6.6 (as well as figure 6.7), a broadly similar temporal pattern is apparent, but with notable distinctions in the details of the force evolution. The drag wake capture curves also exhibit a substantial positive peak near $t/T = 0.14$–0.21, which broadly coincides with the lift peak and corresponds to the period where the wing is moving at high speed through regions of previously shed vorticity. During this phase, the assumed constructive vortex-wing interaction enhances not only lift but also increases the effective relative flow opposing the wing's motion, thereby amplifying the instantaneous drag force relative to quasi-steady predictions.

As the stroke progresses toward $t/T \approx 0.32$–0.40, the drag curves for higher deviation angles develop a marked negative dip (≈ -0.05 to -0.3N), with a minimum typically centered just before stroke reversal. This negative peak could be primarily from the interaction of the wing with its own convected wake during deceleration as seen in the case of lift forces. As the wing slows before changing direction, adverse vortex structures and rapid deceleration cause the direction of net fluid reaction to oppose the traditional drag direction, creating a temporary reduction or reversal in the wake capture drag component, producing a transient thrust-like (negative drag) effect.

6.4. EFFECT OF DEVIATION ANGLE

To quantify the influence of deviation angle on wake capture lift forces, it became essential to distill the temporally varying force signals into a single representative metric for each deviation case. Taking the mean of the force signals over the stroke cycle is a well-established approach in unsteady aerodynamics to achieve this simplification, as it captures the net aerodynamic contribution - the effective force that supports the weight of the insect, flapping drone, or other flapping-wing system - while smoothing transient fluctuations and effectively reduces the force profiles to a scalar quantity that facilitates direct comparison across varying deviation angles.

6.4.1. MEAN OF WAKE CAPTURE FORCES

The attached figure 6.8 presents the variation of mean wake capture forces for both drag (left panel) and lift (right panel) as a function of deviation angle. Across the full range of tested deviation angles, the trends for both force components appear generally similar, yet exhibit notable non-monotonicity and localized extrema, resisting a simple linear interpretation. However, it is important to recognize the level of measurement uncertainty inherent in the experiments, which significantly affects the interpretation of

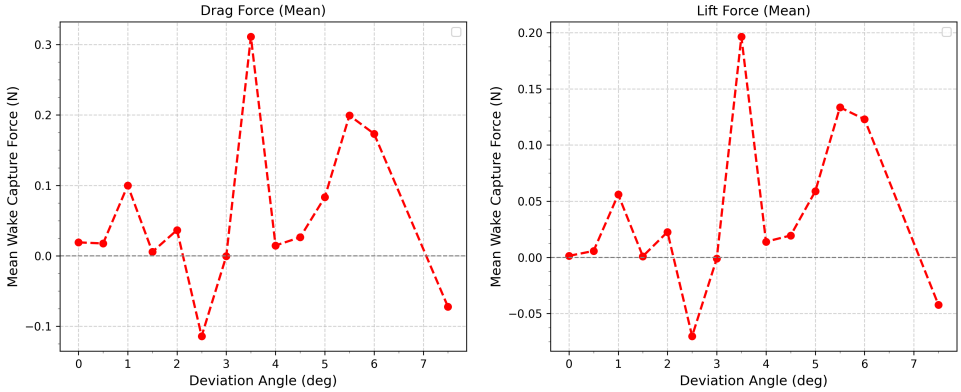

Figure 6.8: Variation of Mean Wake Capture Drag (left) and Lift (Right) Forces with Deviation angles.

these variations. Given that the fundamental structure of the wake and the character of wing-wake interactions are not expected to vary dramatically within the relatively narrow range of tested deviation angles, much of the observed non-monotonic behavior likely arises from experimental noise and uncertainty rather than true physical changes in the flow dynamics. The measured forces, while impressive in aligning with the correct order of magnitude and producing temporal wake capture patterns qualitatively similar across cases, display mean values fluctuating with sufficient sharpness and irregularity to warrant caution against over-interpretation as physical effects.

In the figure 6.8, the observed variation of the mean wake capture drag and lift forces, especially the negative peaks at $\theta \approx 2.5^\circ$ and $\theta \approx 7.5^\circ$ as well as the major positive peak at $\theta \approx 3.5^\circ$ are predominantly attributable to experimental uncertainties and measurement noise, rather than definitive aerodynamic effects. Despite this noise, the forces generally remain slightly above the zero line, indicating a modest net enhancement in both drag and lift due to wake capture.

This modest increase can be rationalized by considering the structure of the wake created by the flapping wing. The shed vortices induce localized flow fields, including regions of induced velocity with components aligned opposite to the wing's motion, effectively increasing the relative velocity at the wing and enhancing aerodynamic forces. Specifically, the downward flow induced by the wake can augment the wing's effective angle of attack, contributing to increased lift. Simultaneously, flow induced in the direction roughly opposing the wing's translational motion leads to an elevated drag. Thus, the induced velocities from the wake tend to add both lift and drag to the wing's aerodynamic forces. Furthermore, from the plots one can assume a slightly increasing trend in these forces from around 2.5° upward (excluding the 7.5° outlier). This increase can be attributed to a threshold effect in three-dimensional wake topology, as discussed before: as the deviation angle grows, the wing's path becomes increasingly non-planar, potentially intersecting regions of the wake previously unexploited at lower deviation values

[27, 56, 47, 33, 16]. While at lower deviation angles ($\theta \approx 0°$–$2°$), forces remain near baseline with minimal fluctuation, possibly because of the primarily planar kinematics and relatively slower velocities, thus dominated by relatively stable LEV formation and quasi-steady translation, while wake capture playing a secondary modulating role.

It should be emphasized that, while these interpretations are grounded in established aerodynamic theory and consistent with trends reported in the literature, the actual spatial and temporal structure of the wake, and thus the detailed mechanisms governing the observed force variations, are likely to be highly system-dependent and sensitive to the precision of the kinematics, uncertainty in measurements, and the Reynolds number regime employed. Experimental approximations and noise or vibration issues in the setup contribute to the observed non-monotonicity in the data. Nonetheless, the overall modestly positive nature of the wake capture suggests that optimal exploitation of wake capture for aerodynamic augmentation is tightly coupled to the careful adjustment of deviation angle, and that the relationship is best described as highly phase and flow-regime dependent rather than monotonic.

6.4.2. LIFT TO DRAG RATIO

With a comprehensive understanding of the temporal behaviour of the wake capture lift and drag forces, it becomes meaningful to evaluate their ratio of these force profiles, namely the lift-to-drag (L/D) ratio, under wake capture conditions. This ratio serves as a direct measure of the aerodynamic efficiency of the flapping motion, capturing how effectively the wing converts unsteady flow interactions into useful vertical (lift-producing) force relative to the horizontal (drag-inducing) resistance encountered. In the context of flapping flight, particularly during wake capture phases, a high L/D ratio indicates that the wing is harnessing the unsteady flow field to generate beneficial lift with minimal energetic penalty in the form of drag. By examining how this ratio varies with deviation angle, one can identify the kinematic regimes that maximize aerodynamic utility during the stroke reversal.

The attached figure 6.9 presents the variation of the ratio of mean lift force to mean drag force ($\overline{L}/\overline{D}$) as a function of deviation angle, with separate curves for the experimental data and the predictions of the quasi-steady (QS) model.

In the QS model, the mean lift-to-drag ratio, as seen in figure 6.9, displays a smooth and gradually decreasing trend with increasing deviation angle, with a maximum value of ~0.652 at 0° deviation. This behavior arises because the QS approach determines aerodynamic forces solely from instantaneous, prescribed kinematics - the wing's geometric trajectory, velocity, and angle of attack at each point in the cycle. As the deviation angle increases, the out-of-plane motion alters the geometric configuration of the wing's trajectory, which in turn reduces the time-averaged angle of attack and modifies the orientation and magnitude of the velocity components contributing to lift and drag. These geometric and kinematic effects, computed directly from the imposed motion, lead to a predictable monotonic reduction in mean lift and a relatively less pronounced change in mean drag, resulting in the observed decline in $\overline{L}/\overline{D}$. Importantly, the QS model can-

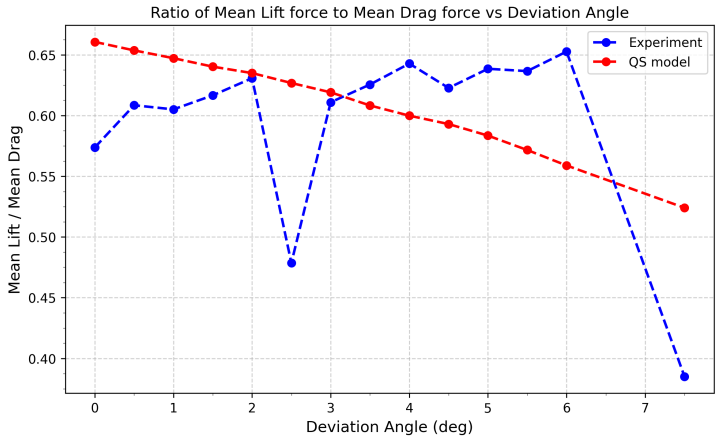

Figure 6.9: Variation of the ratio of mean lift force to mean drag force ($\overline{L}/\overline{D}$) as a function of deviation angle, with separate curves for the experimental data and the predictions of the quasi-steady (QS) model. This lift-to-drag ratio is a critical metric in flapping wing aerodynamics, as it fundamentally characterizes the aerodynamic efficiency - higher values indicate more effective lift generation relative to drag, which is desirable for sustained hovering or maneuvering in insect flight.

not account for additional modifications to the effective angle of attack or local velocity orientation resulting from unsteady, history-dependent phenomena such as vortex-induced downwash or upwash, wake capture effects, or three-dimensional flow separations. Consequently, its predictions are characteristically smoother, lacking the pronounced non-monotonicity and abrupt variations that arise from possible vortex–wing interactions.

Unlike the quasi-steady (QS) model, the experimental lift-to-drag ratio starts at a relatively low value of approximately 0.555 and exhibits a slight increasing trend thereafter. At lower deviation angles ($\theta < 3°$), the experimental ratio remains just below the QS predictions. This difference arises because, in near-planar kinematics, the wing motion closely follows a flat stroke plane where the primary aerodynamic mechanism is the stabilized leading-edge vortex (LEV), which provides consistent lift. However, the drag remains relatively elevated in this regime due to prolonged exposure of the wing to viscous shear and pressure drag forces associated with sustained interaction with the fluid in the stroke plane. Additionally, the limited out-of-plane motion restricts effective engagement with the energetic structures in the wake, reducing opportunities for wake capture to augment lift or mitigate drag.

Above $\theta \approx 3°$, the experimental lift-to-drag ratio marginally exceeds the QS model's prediction over a narrow interval. This can be rationalized by the heightened significance of out-of-plane motion and associated three-dimensional effects, which augment the wing's ability to constructively interact with its own wake. In this regime, the wing could be encountering previously shed vortices at favorable phases of the stroke cycle, which elevates the effective angle of attack and significantly boosts bound circulation dur-

ing wake capture events. This transient alignment amplifies lift production without an equivalent rise in drag, thus raising the lift-to-drag efficiency beyond what is predicted by quasi-steady theory.

It is also important to note the pronounced dips in the experimental ratio at deviation angles near 2.5° and 7.5°. As discussed in Section 5.10, these sharp extrema are most likely artefacts caused by increased uncertainty and scatter in the force measurements, rather than genuine physical effects.

Collectively, the contrasting trends between experimental observations and QS model predictions highlight the fundamental role of unsteady, phase-dependent aerodynamic mechanisms in real flapping wings, particularly wake capture and instantaneous vortex-induced velocity effects, that differentially amplify or blunt lift and drag as the deviation angle varies.

From this analysis, it could be concluded that Wake capture does not produce a uniformly positive or negative effect. At intermediate deviation angles (approximately 3.5–6 degrees), experimental results reveal a beneficial lift-to-drag ratio, suggesting that wake capture events are most constructive here, temporarily enhancing aerodynamic efficiency through favorable vortex–wing interactions. However, at low deviation angles, wake capture effects may be less beneficial or even detrimental, as indicated by the lower lift-to-drag ratios. In summary, wake capture can augment aerodynamic performance, but only within a narrow range of deviation angles where the kinematic and wake-phase conditions are favorably aligned; outside this range, its effect diminishes or reverses.

6.4.3. POWER UTILIZATION

Having established a preliminary understanding of the aerodynamic efficiency of the flapping motion, particularly through metrics like the lift-to-drag ratio, it becomes important to complement this analysis by examining the associated power consumption for each deviation angle. This added dimension of power analysis helps in identifying configurations that strike a balance between aerodynamic performance and energetic cost, thereby offering a more holistic assessment of the flapping wing physics.

Power can be computed as:

$$P = T \cdot \omega = (F_x \cdot \text{Radius of Gyration}) \cdot \omega = F_x \cdot \text{velocity} \tag{6.6}$$

Here:

- P = Power
- T = Torque
- ω = Angular velocity
- F_x = Normal force on the wing

The figures 6.10 and 6.11 below illustrate the temporal variation of the normal force and wingtip velocity during the half-stroke for each deviation angle, for both the experiment and QS Model seperately. Using these two signals, instantaneous power was computed as the product of force and velocity, and the results were subsequently averaged over time to obtain the mean power corresponding to each deviation angle. The bottom panel of the figures 6.10 and 6.11 show how this mean power varies with deviation angle.

Focusing on the experimental results first, shown in figure 6.10, the mean power plot reveals a distinctly non-monotonic dependence: at low deviation angles, the mean power remains comparatively low with moderate fluctuations (centering around 0.035 to 0.04 W), followed by a marked rise leading to a sharp local maximum near $\theta \approx 6^\circ$, and then a pronounced decline at the highest tested deviation angle.

This trend can be interpreted in light of the interplay between aerodynamic force-production mechanisms and kinematic effects as deviation angle increases. At small deviation angles ($< 3^\circ$), the wing trajectory remains nearly planar, where minimal wake interaction is expected due to the previously discussed stabilization of the leading-edge vortex (LEV). This results in relatively modest force and velocity amplitudes, leading to a correspondingly low mechanical power requirement for flapping. As the deviation angle increases, out-of-plane wing motion becomes more pronounced, enhancing the wing's interaction with shed vortices. This increased interaction can amplify both the magnitude and variability of the normal force and wing-tip velocity, thereby elevating the mean power demand. The sharp local maximum and the subsequent abrupt fall-off in power at the higher deviation angles (6° and 7.5° respectively) can be attributed primarily to high measurement uncertainty rather than actual physical phenomena. Nevertheless, it can be reasonably concluded that power utilization tends to be marginally higher at larger deviation angles compared to smaller ones.

Now, analyzing the variation of mean power with deviation angle for the QS Model (see Figure 6.11), it is apparent that the trend follows a broadly parabolic profile: mean power starts relatively high at zero deviation, decreases steadily as deviation angle increases, and reaches a clear minimum between 4° and 5°, before rising again at the largest deviation angles.

At smaller deviation angles, the QS model predicts relatively high mean power values (~0.039 W at 0°), consistent in the order of magnitude with the experimental results in this regime. This agreement between the experimental and QS model magnitudes, is expected, as wake interactions in the experimental data are minimal for near-planar flapping due to the previously discussed LEV stabilization in this range of low deviation angles. Thus, the purely kinematic approach used in quasi-steady model, sufficiently captures the relevant aerodynamics in this regime. Here, the wing motion is dominated by planar kinematics with higher instantaneous drag forces and velocities resulting in relatively high power.

As the deviation angle increases beyond 3°, the QS model predicts a continued reduction

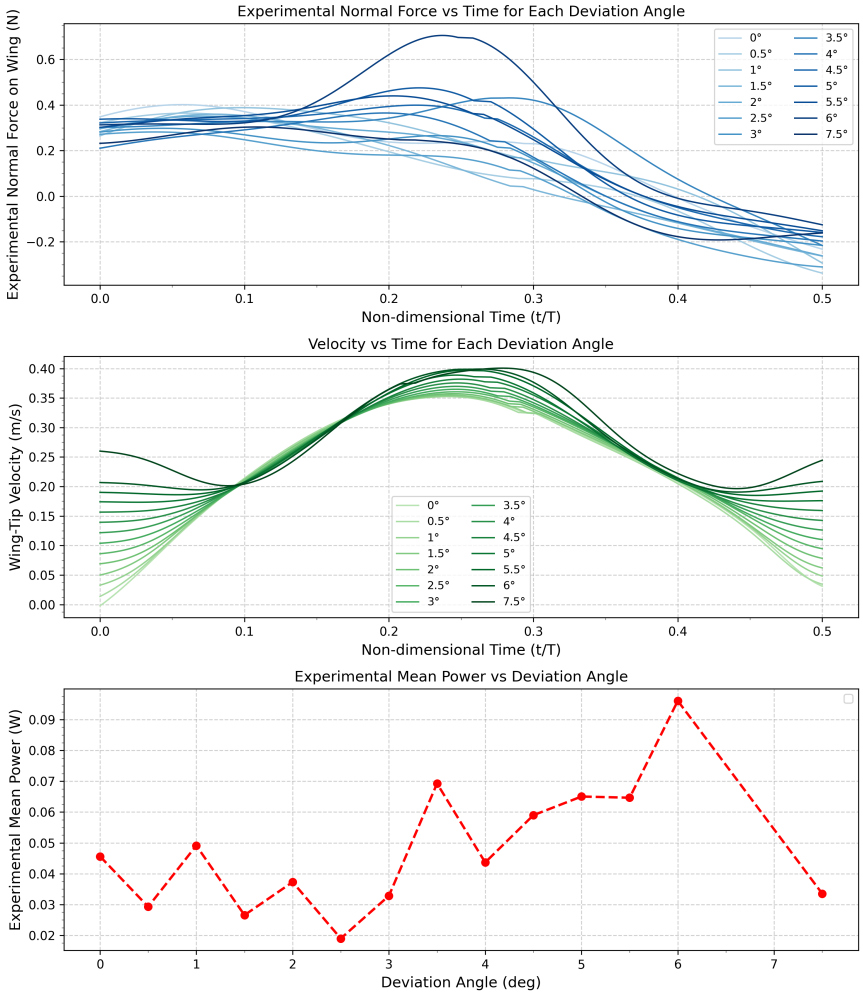

Figure 6.10: Overview of experimentally measured aerodynamic force, wing-tip velocity, and power consumption as functions of deviation angle and stroke phase. **Top:** Experimental normal force profiles on the wing as a function of non-dimensionalized time (t/T) for a range of deviation angles, demonstrating the temporal evolution and sensitivity of force generation to kinematic envelope. **Middle:** Corresponding wing-tip velocity profiles for each deviation angle, illustrating how the magnitude and timing of peak velocities shift across the tested kinematic space. **Bottom:** Mean aerodynamic power, calculated as the time-average of the product of instantaneous normal force and wing-tip velocity, plotted as a function of deviation angle.

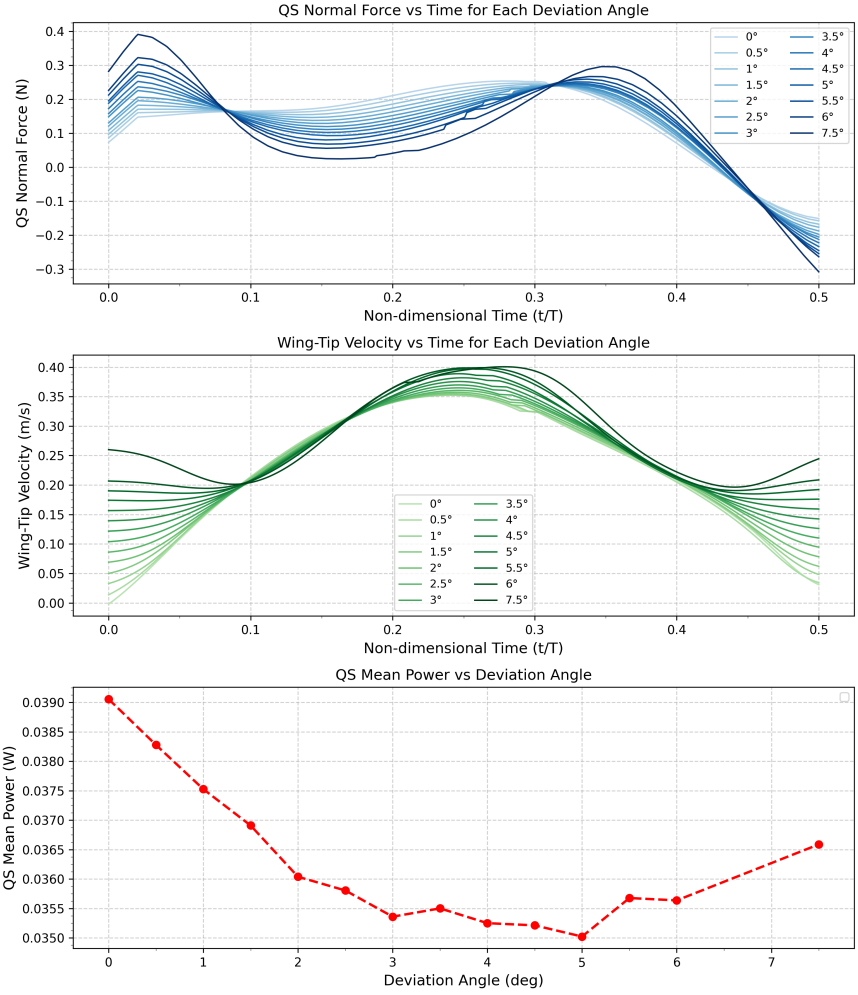

Figure 6.11: Overview of quasi-steady (QS) model predictions for aerodynamic force, wing-tip velocity, and power consumption as functions of deviation angle and stroke phase. **Top:** Predicted normal force profiles per the QS model, plotted over non-dimensional time (t/T) for a series of deviation angles, illustrating the temporal evolution and attenuation of force generation as the out-of-plane motion is varied. **Middle:** QS model wing-tip velocity profiles as a function of stroke phase for each deviation angle, highlighting systematic changes in peak velocity magnitude and timing imposed by the kinematic envelope. **Bottom:** Mean aerodynamic power, computed as the cycle-average of the product of QS-predicted normal force and wing-tip velocity, plotted against deviation angle.

in mean power, reaching its minimum at 4° to 5°. This trend is in stark contrast to the experimental data, which show increased power utilization in this range. This opposite behavior and the observed minimum in the QS curve can be attributed to the model's inability to incorporate wake–structure interactions and the resulting aerodynamic forces that become significant at larger deviation angles.

In conclusion, the mean power from the experimental data exhibits a non-monotonic relationship with deviation angle, driven by increasing wing-wake interactions and resulting in elevated power demand at moderate to high deviation angles. In contrast, the QS model predicts a smooth, parabolic trend reflecting purely kinematic effects and lacking the wake-structure interactions as expected.

6.4.4. FLAPPING EFFICIENCY

Now that both the lift generated and the corresponding power utilization have been quantified, it becomes meaningful to assess the flapping efficiency - a measure of how effectively the input power is converted into useful aerodynamic lift force. To evaluate this, the **Rankine–Froude Momentum Theory** provides a suitable framework [4]. According to this theory, flapping efficiency (η) can be defined as the ratio of the minimum power theoretically required to generate a given lift (P_{min}) to the actual mean power expended during motion (P), i.e.,

$$\eta = \frac{P_{\text{min}}}{P}. \tag{6.7}$$

In this formulation, P is calculated directly from experimental data as the time-averaged product of the normal force and the wingtip velocity:

$$P = \langle F_x(t) \cdot U(t) \rangle, \tag{6.8}$$

It is important to acknowledge that using the wingtip velocity as the velocity scale can lead to an overestimation of P. This is because the aerodynamic force is, on average, applied closer to the wing root, where the local velocity is smaller than at the tip. Furthermore, this method assumes that the center of pressure, the point on the wing through which the aerodynamic force effectively acts, remains fixed across different deviation angles. While this assumption serves as a reasonable first-order approximation, in reality the center of pressure may shift with changing kinematics, introducing additional variability.

P_{min} represents the idealized minimum power required to produce the observed mean lift under inviscid, quasi-steady momentum principles. The expression for P_{min} is derived from the classical Rankine–Froude momentum theory, which models the actuator disk (or propeller) as an idealized surface imparting momentum to a continuous stream of fluid. In this framework, the minimum power required to maintain a given mean lift L is equivalent to the rate at which kinetic energy is imparted to the fluid to generate a downward momentum flux equal to L. Assuming inviscid, steady, and quasi-one-

dimensional flow through an actuator disk immersed in an infinite fluid (with no losses due to viscosity or turbulence), the induced velocity at the disk necessary to support lift L is:

$$w = \sqrt{\frac{L}{2\rho A}} \tag{6.9}$$

The rate of work done on the fluid - corresponding to the minimum aerodynamic power input - is then given by the product of the lift force and the induced velocity:

$$P_{\min} = L \cdot w = L \cdot \sqrt{\frac{L}{2\rho A}} \tag{6.10}$$

where:

- L is the mean lift corresponding to each deviation angle,
- ρ is the fluid density (taken as 1000 kg/m^3 for water),
- A is the effective area swept by the wing, estimated as $A = \theta \cdot \frac{b^2}{2}$,
- θ is the sweep amplitude in radians, and
- b is the wingspan in meters.

This represents the lowest possible power expenditure for a given mean lift, under the idealized conditions of momentum jet theory. In practical terms, $P_{\min}$ serves as a theoretical lower bound for aerodynamic power consumption, as it neglects viscous, unsteady, and three-dimensional effects present in real biological or mechanical flapping systems. As such, the ratio $\eta = P_{\min}/P$ provides a normalized measure of how efficiently the aerodynamic power exerted is converted into useful lift, relative to this idealized minimum.

Figure 6.12 displays the variation of flapping efficiency, $\eta = P_{\min}/P$, computed using the Rankine-Froude momentum theory, as a function of deviation angle for both the experimental data and the quasi-steady (QS) model.

The experimental flapping efficiency curve demonstrates that, across most deviation angles, efficiency values are similar to, or only marginally higher than, those predicted by the QS model. The most notable exceptions are the pronounced peaks at deviation angles of 2.5° and 7.5°, where experimental efficiency drops below the quasi-steady estimate, and at 3.5° where the experimental efficiency rises sharply above the quasi-steady estimate. These isolated spikes are likely artifacts arising from elevated measurement uncertainty rather than genuine aerodynamic phenomena.

Excluding these anomalous points, the efficiency trend shows a marginal increase at moderate to higher deviation angles (particularly between 5° and 6°) compared to the

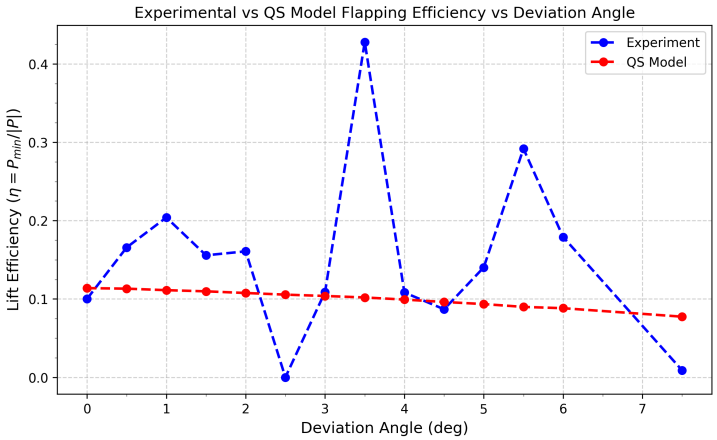

Figure 6.12: Comparison of Flapping Efficiency for different deviation angles, separately for Experiment (Blue) and QS Model (Red).

lower deviation range. This can be understood as a consequence of the underlying wing kinematics. At low deviation angles, the trajectory is nearly planar, resulting in lower, more stable velocities and effective stabilization of the leading-edge vortex (LEV), and thereby minimal interaction with shed vortices. Consequently, the forces generated, and thus energetic efficiency, remain relatively low. In contrast, at higher deviation angles, the wing experiences significant out-of-plane motion, traverses at higher instantaneous velocities, and likely experiences less LEV stabilization. Under these circumstances, stronger interactions between the wing and shed vortices can increase aerodynamic force production, modestly boosting lift efficiency relative to the power input.

However, it is important to exercise caution when interpreting these trends, as measurement uncertainty may play a significant role in shaping the observed efficiency profile - including the minor enhancement seen at higher deviation angles.

In contrast, the QS model predicts a smoothly decreasing efficiency with increasing deviation angle, lacking the pronounced maximum seen in the experiments. This outcome is a direct consequence of the model's reliance on instantaneous, kinematics-based force computations that omit history-dependent and unsteady flow effects. As the deviation angle increases, the kinematically imposed reduction in effective angle of attack and altered velocity orientation reduce the model's predicted lift relative to power consumption in a gradual, monotonic fashion. Without the contribution from dynamic phenomena such as wake capture, the QS model inherently underestimates the possibility of peak efficiency at intermediate deviations and provides a more conservative, smoothed baseline trend.

In summary, the experimental results demonstrate that flapping efficiency reaches a maximum at intermediate deviation angles (approximately 5°– 6°), highlighting the sig-

nificance of optimally tuned wing kinematics and unsteady aerodynamic mechanisms, such as wake capture and constructive vortex–wing interactions, in maximizing aerodynamic performance. Nevertheless, it is important to recognize that the observed trends may be influenced by limitations inherent to the experimental setup, such as the variations in force measurement accuracy, and the influence of tank-wall effects or background turbulence in the flow environment. Furthermore, assumptions such as the estimation of swept area, the use of time-averaged forces, and the presumption of idealized flow for the Rankine–Froude efficiency metric may all introduce approximations that affect the quantitative interpretation of efficiency. As such, while the presented data strongly suggest that intermediate deviation angles are energetically favorable under the tested conditions, these conclusions should be viewed within the context of the underlying experimental constraints and model simplifications. Future studies employing refined measurement techniques and advanced flow diagnostics may further clarify the extent and robustness of these efficiency trends in natural and engineered flapping systems.

CONCLUSION

This study set out to investigate the aerodynamic influence of deviation angle - representing the vertical (heaving) component of three-dimensional figure-of-eight wingtip kinematics - on wake capture forces during hovering flight. Using an abstracted mosquito-inspired kinematic model executed on a dynamically scaled robotic flapping wing, and a comparative quasi-steady (QS) aerodynamic framework, the objective was to quantify how varying deviation influences unsteady wing–wake interaction forces, aerodynamic efficiency, power consumption, and overall flapping performance.

Studies were performed across a range of deviation angles $0° - 6°$ (including an outlier at $7.5°$). The results unambiguously confirm that deviation angle exerts a non-monotonic influence on wake capture forces in real, unsteady flows, whereas the quasi-steady (QS) model predicts smooth, monotonic trends governed purely by kinematic geometry. However, it is critical to acknowledge the significant measurement uncertainty inherent in the experiments, which substantially impacts the interpretation of observed variations. Thus, much of the non-monotonic behavior observed is likely attributable to experimental noise and uncertainty rather than to true physical changes in flow dynamics. While the measured wake capture forces align with the correct order of magnitude and reproduce qualitatively consistent temporal patterns across cases, the mean values fluctuate with sufficient sharpness and irregularity to warrant caution against over-interpretation as definitive physical phenomena.

Across the tested deviation range, the wake capture lift and drag forces exhibit pronounced localized peaks at $\theta \approx 2.5°$, $3.5°$, and $6°$. It is noteworthy that the narrowness and immediacy of these peaks reveal the elevated measurement uncertainty highlighted before; hence, these peaks are likely artifacts of sensor noise or vibration rather than a true aerodynamic effects. Excluding these localized peaks, wake capture forces were generally positive, with relatively elevated values observed in the range $\theta \approx 5° - 6°$, suggesting enhanced aerodynamic interaction within this interval.

The lift-to-drag ratio exhibited contrasting trends between experimental observations and quasi-steady (QS) model predictions. While both experiments and the QS model showed similar orders of magnitude, the QS model predicted a monotonic decrease with increasing deviation angle, whereas the experimental data revealed a slight increasing trend. Notably, in the mid-to-high deviation range (approximately $3.5°$ to $6°$), the experimental lift-to-drag ratio marginally exceeded the QS predictions, indicating a beneficial aerodynamic contribution from unsteady wake interactions in this regime. Conversely, at lower deviation angles ($0°$ to $3°$), wake capture provided little to no improvement, and in some cases a slightly negative effect on aerodynamic efficiency.

The energetic analysis shows further contrast between the experimental data and the quasi-steady (QS) model within the deviation angle range of approximately 3.5° to 6°. The experimental data indicate increased power utilization in this mid-to-high deviation range, whereas the QS model predicts a decreasing power trend. When power consumption is related to useful lift output using the Rankine–Froude flapping efficiency metric, and excluding outliers caused by measurement uncertainty, the experimental flapping efficiency is generally marginally higher than the QS model predictions, especially between 5° and 6°. This deviation range also corresponds to a favourable range in the lift-to-drag ratio, demonstrating that unsteady wake effects are consistently seen to be aerodynamically beneficial within this particular range of deviation angles.

The observed aerodynamic benefits at mid-to-high deviation angles is understood to be arising from the pronounced out-of-plane wing motion associated with increased deviation, which elevates local kinematic velocities and introduces complex three-dimensional flow dynamics. Unlike at lower deviation angles, where leading-edge vortex (LEV) stabilization predominates, these intensified three-dimensional kinematics disrupt LEV stability, resulting in the generation of more intricate vortical wake structures. The wing's subsequent interaction with this enriched wake region enhances aerodynamic force production.

Collectively, these findings indicate that wake capture in hovering flapping wings is neither uniformly beneficial nor detrimental. Instead, its aerodynamic contribution depends critically on deviation angle and the precise phasing between the wing trajectory and the convected wake topology. The study quantitatively demonstrates that: (i) maximum constructive wake capture occurs within a broader intermediate deviation range ($\theta \approx 5° - 6°$), where lift, lift-to-drag ratio, and flapping efficiency are enhanced above quasi-steady predictions despite pronounced measurement uncertainty; (ii) low deviations (below $\sim 3°$) produce minimal wake interaction and little to no aerodynamic benefit, sometimes even slightly reducing efficiency relative to quasi-steady predictions; These results highlight the importance of finely tuning wing kinematics to optimize aerodynamic performance by exploiting favorable wake interactions during hovering flight

It is important to view these conclusions in the context of the study's experimental constraints and modelling approximations. The scaled experiments were conducted at Re ≈ 7270, considerably higher than the Re ≈ 120 characteristic of mosquito flight. While this facilitated force measurement with decent signal to noise ratio, and preserved the qualitative physics of unsteady phenomena such as leading-edge vortex formation and wake capture, quantitative scaling to insect flight may differ due to viscosity–inertia balance. The rigid rectangular wing planform used here omits morphological features of natural mosquito wings, intentionally isolating kinematic effects but neglecting potential spanwise flow and tip-vortex influences of real planforms. Kinematics were implemented as sinusoidal approximations derived from Fourier fits to biological data, enabling controlled parametric variation but not capturing finer asymmetries of real motion. The Reynolds–Froude based efficiency metric assumes inviscid, axisymmetric induced flow and may slightly misrepresent power–lift coupling for strongly three-dimensional wakes.

Additional experimental limitations include potential tank-wall influences, small residual baseline drift in force measurement, and finite differentiation errors in QS force computation, with all these concerns greatly overshadowed by the extremely high uncertainty in the force measurements caused by persistent sensor noise and vibration issues.

Despite the outlined constraints, approximations, and limitations, this study successfully established an experimental setup with a high degree of kinematic precision and fidelity for examining the impact of deviation angle on wake capture phenomena. The investigation systematically identified the principal limitation of the setup as the elevated noise and uncertainty originating from the inbuilt force sensor; an issue that can only be fully resolved by replacing the sensor, which was beyond the scope of this project timeline. Nevertheless, within these boundaries, the experiment yielded valuable insights with direct implications for both the fundamental understanding of biological flight and the kinematic optimization of bio-inspired micro aerial vehicles (MAVs), where deliberate tuning of deviation motion could enhance hovering efficiency without significant energetic penalties.

FUTURE RECOMMENDATIONS

The next phase of this project should prioritize upgrading the force sensor and reinforcing the wing-shaft assembly to address the persistent noise and vibration issues identified in the current setup, which have led to elevated uncertainty in the aerodynamic force measurements. Future experiments should utilize a more viscous fluid mixture, such as a glycerol-water blend, to match the biologically relevant Reynolds number regime for mosquitoes. This approach will then accurately replicate the flow conditions experienced in their natural environment and enable a more precise capture of the relevant fluid dynamics. Importantly, integrating advanced flow visualization tools such as Particle Image Velocimetry (PIV) will yield direct insight into the formation and evolution of wake vortices, enabling robust validation of the hypotheses regarding wing–wake interactions established in this study. While factors such as precise biological wing profiles and wing flexibility are valuable, they are best reserved for subsequent stages, once core measurement fidelity and dynamic similarity have been achieved, as these refinements will allow a more nuanced exploration of morphological and structural effects on unsteady aerodynamic phenomena. Ultimately, this work lays the foundation for a more rigorous and biologically relevant characterization of wake capture aerodynamics, providing both a validated experimental framework and a clear roadmap for advancing the fidelity of future investigations.

REFERENCES

[1] In: (2024). URL: https://www.ecdc.europa.eu/en/publications-data/mosquito-borne-diseases-emerging-threat.

[2] In: (2024). URL: https://ui.adsabs.harvard.edu/abs/2024PhFl...36b1907L/abstract.

[3] In: (2024). URL: https://www.gavi.org/vaccineswork/genetically-modified-mosquitoes-and-malaria-africa-top-scientist-shares-latest.

[4] T.E.J. Arends. "Investigation of wing kinematics influence on the aerodynamic flight of mosquitoes". In: (2024).

[5] Julius S. Bendat and Allan G. Piersol. *Random Data: Analysis and Measurement Procedures*. 4th. Hoboken, NJ: John Wiley & Sons, 2010. ISBN: 9780470248775. DOI: 10.1002/9781118032428.

[6] L. Bennett. "Insect flight: lift and the rate of change of incidence". In: *Science* 167 (1970), pp. 177–179.

[7] Richard Bomphrey. "Smart wing rotation and trailing-edge vortices enable high frequency mosquito flight". In: *Nature* (2017).

[8] D.O. Carvalho et al. "Supression of a field population of Aedes aegypti in Brazil by sustained release of transgenic male mosquitoes". In: *PLoS Neglected Tropical Diseases* 9.7 (2015), pp. 1–15.

[9] Bo Cheng. "Flying of insects from Part III - Natural phenomena". In: *Chinese Journal of Theoretical and Applied Mechanics* 52.6 (2020), pp. 1525–1534. DOI: 10.6052/0459-1879-19-413.

[10] Dee Chin. "Flapping wing aerodynamics". In: (2016). No formal journal located; may be thesis or internal report.

[11] Haoran Chu and H. Liu. "Aerodynamics of a wing under figure-of-eight flapping motion". In: *Physics of Fluids* 33.10 (2021). DOI: 10.1063/5.0061434.

[12] John O. Dabiri. "Optimal vortex formation as a unifying principle in biological propulsion". In: *Annual Review of Fluid Mechanics* 41 (2009), pp. 17–33. DOI: 10.1146/annurev.fluid.010908.165232.

[13] S. Dalton et al. "Borne on the Wind". In: *Reader's Digest Press, New York* (1975).

[14] TU Delft. "The Delfly Project". In: 1 (2025). Accessed: 2025-08-26. URL: https://www.delfly.nl/home/.

[15] M. H. Dickinson. "The effects of wing rotation on unsteady aerodynamic performance at low Reynolds numbers". In: *J. Exp. Biol.* 192 (1994), pp. 179–206.

[16] M. H. Dickinson and K. G. G"otz. “Unsteady aerodynamic performance of model wings at low Reynolds numbers”. In: *J. Exp. Biol.* 174 (1993), pp. 45–64.

[17] M. H. Dickinson, F.-O. Lehmann, and K. G. G"otz. “The active control of wing rotation by Drosophila”. In: *J. Exp. Biol.* 182 (1993), pp. 173–189.

[18] M. H. Dickinson, F.-O. Lehmann, and S. P. Sane. “Wing rotation and the aerodynamic basis of insect flight”. In: *Science* 284 (1999), pp. 1954–1960.

[19] C. P. Ellington. “The aerodynamics of hovering insect flight. I. The quasi-steady analysis”. In: *Phil. Trans. R. Soc. Lond. B* 305 (1984), pp. 1–15.

[20] C. P. Ellington. “The aerodynamics of hovering insect flight. II. Morphological parameters”. In: *Phil. Trans. R. Soc. Lond. B* 305 (1984), pp. 17–40.

[21] C. P. Ellington. “The aerodynamics of hovering insect flight. III. Kinematics”. In: *Phil. Trans. R. Soc. Lond. B* 305 (1984), pp. 41–78.

[22] C. P. Ellington. “The aerodynamics of hovering insect flight. IV. Aerodynamic mechanisms”. In: *Phil. Trans. R. Soc. Lond. B* 305 (1984), pp. 79–113.

[23] C. P. Ellington. “The aerodynamics of hovering insect flight. VI. Lift and power requirements”. In: *Phil. Trans. R. Soc. Lond. B* 305 (1984), pp. 145–181.

[24] C. P. Ellington. “The novel aerodynamics of insect flight: applications to micro-air vehicles”. In: *J. Exp. Biol.* 202 (1999), pp. 3439–3448.

[25] Thomas Engels et al. “Helical vortices generated by flapping wings of bumblebees”. In: *Fluid Dyn. Res.* 50.1 (2018). Published 16 January 2018. DOI: 10.1088/1873-7005/aa908f.

[26] S. Gorle et al. “Hydrodynamics of Octagonal Culture Tanks with Cornell Inlet Layout: Numerical and Experimental Investigations”. In: *Aquacultural Engineering* 82 (2018), pp. 59–73. DOI: 10.1016/j.aquaeng.2018.03.003.

[27] Hyunwoo Jung. “Role of the deviation motion on the aerodynamic performance of a mosquito wing in hover”. In: (2024). Conference or thesis work; no DOI or journal located.

[28] Christopher Koehler et al. “Vortex visualization in ultra low Reynolds number insect flight”. In: *Visualization and Data Analysis 2011* 7868 (2011). SPIE Conference Proceedings. DOI: 10.1117/12.873366.

[29] M.U.G. Kraemer et al. “Past and future spread of the arbovirus vectors Aedes aegypti and Aedes Albopictus”. In: *Nature Microbiology* 4 (2019), pp. 854–863.

[30] A. M. Kuethe and J. D. Schetzer. *Foundations of Aerodynamics*. 2nd. John Wiley & Sons, 1959.

[31] Fritz-Olaf Lehmann and Simon Pick. “The aerodynamic benefit of wing–wing interaction depends on stroke trajectory”. In: *Journal of Experimental Biology* 210.8 (2007), pp. 1362–1377. DOI: 10.1242/jeb.02761.

[32] Hao Li and Mostafa Nabawy. “Detachment of leading-edge vortex enhances wake capture force production”. In: (2024).

[33] Long-Gui Liu, Gang Du, and Mao Sun. “Aerodynamic-force production mechanisms in hovering mosquitoes”. In: *Journal of Fluid Mechanics* 898.A19 (2020). DOI: 10.1017/jfm.2020.386.

[34] N. Liu. “Insecticide resistance in mosquitoes: impact, mechanisms, and research directions”. In: *Annual Review of Entomology* 60 (2015), pp. 537–559.

[35] Guoyu Luo and Mao Sun. “Effects of stroke deviation on aerodynamic force production of a flapping wing”. In: *Bioinspiration Biomimetics* 13.5 (2018). DOI: 10.1088/1748-3190/aacf0b.

[36] Yu Zhu Lyu, Min Hao, and Mao Sun. “Flapping-mode changes and aerodynamic mechanisms in miniature insects”. In: *Bioinspiration Biomimetics* 14.5 (2019). DOI: 10.1088/1748-3190/ab2cfa.

[37] Alexander Mathis et al. “DeepLabCut: markerless pose estimation of user-defined body parts with deep learning”. In: *Nature Neuroscience* 21.9 (2018), pp. 1281–1289. DOI: 10.1038/s41593-018-0209-y.

[38] T. Maxworthy. “Experiments on the Weis-Fogh mechanism of lift generation by insects in hovering flight. Part 1. Dynamics of the ’fling’”. In: *J. Fluid Mech.* 93 (1979), pp. 47–63.

[39] Douglas C. Montgomery and George C. Runger. *Applied Statistics and Probability for Engineers*. 6th. Hoboken, NJ: John Wiley & Sons, 2014. ISBN: 9781118539712.

[40] World Health Organization. “Vector-born diseases”. In: (2020).

[41] Nathan Phillips and Kevin Knowles. “Formation of the leading-edge vortex and spanwise flow on an insect-like flapping-wing throughout a flapping half cycle”. In: *AIAA Journal* 46.5 (2008), pp. 1130–1140. DOI: 10.2514/1.29104.

[42] Thomas Rakotomamonjy, Mustapha Ouladsine, and Thierry Le Moing. “Kinematics optimization for a flapping-wing micro air vehicle”. In: *IFAC Proceedings Volumes (First European MAV Conference)* 38-1.13 (2005), pp. 217–221. DOI: 10.1016/S1474-6670(17)63417-5.

[43] M. Researcher and L. Engineer. “Residence Time Distribution of an Irregular Octagonal Tank under Hydrodynamic Sloshing Effects”. In: *Chemical Engineering Science* 256 (2023). DOI: 10.1016/j.ces.2022.117694.

[44] S.A. Ritchie et al. “Application of wMelPop Wolbachia strain to crash local populations of Aedes aegypti”. In: *PLoS Neglected Tropical Diseases* 9.7 (2015), pp. 1–17.

[45] Stäubli Industrial Robots. “TX2-140/160 Datasheet”. In: (2025). Accessed: 2025-08-26. URL: https://www.staubli.com/content/dam/robotics/products/robots/tx2/TX2-140-160-datasheet-EN.pdf.

[46] G. V. Lauder S. A. Chandorkar Y. Najafabadi. “Analysis of flow field and forces on a deforming wing in a water tank: effects of confinement”. In: *Exp. Fluids* 39.2 (2005), pp. 287–297. DOI: 10.1007/s00348-005-0963-2.

[47] S. P. Sane. “The aerodynamics of insect flight”. In: *Journal of Experimental Biology* (2003), pp. 4191–4208.

[48] S. P. Sane and M. H. Dickinson. “The aerodynamic effects of wing rotation and a revised quasi-steady model of flapping flight”. In: *J. Exp. Biol.* 205 (2002), pp. 1087–1096.

[49] S. P. Sane and M. H. Dickinson. “The control of flight force by a flapping wing: lift and drag production”. In: *J. Exp. Biol.* 204 (2001), pp. 2607–2626.

[50] Aamer Shahzad et al. “Effects of wing shape, aspect ratio and deviation angle on aerodynamic performance of flapping wings in hover”. In: *Physics of Fluids* 28.11 (2016). DOI: 10.1063/1.4964928.

[51] Balbir Singh et al. “Quasi-steady aerodynamic modeling and dynamic stability of mosquito-inspired flapping wing pico aerial vehicle”. In: *Frontiers in Robotics and AI* (2024).

[52] Jitendra Singh et al. “Robotic Bees”. In: *International Journal of Applied Engineering Research* (2014).

[53] M. Sun and J. Tang. “Unsteady aerodynamic force generation by a model fruit fly wing in flapping motion”. In: *J. Exp. Biol.* 205 (2002), pp. 55–70.

[54] Mohammed B. Trabia. “Flight characteristics of flapping wing miniature air vehicles with “Figure-8” spherical motion”. In: (2009). Likely unpublished or thesis-based; unable to locate formal journal.

[55] H. Wagner. “"Uber die Entstehung des dynamischen "Auftriebes von Tragfl"ugeln”. In: *Z. Angew. Math. Mech.* 5 (1925), pp. 17–35.

[56] Q. Wang, J. F. L. Goosen, and F. van Keulen. “A predictive quasi-steady model of aerodynamic loads on flapping wings”. In: *Journal of Fluid Mechanics* 800 (2016), pp. 688–719. DOI: 10.1017/jfm.2016.413.

[57] T. Weis-Fogh. “Quick estimates of flight fitness in hovering animals, including novel mechanisms for lift production”. In: *J. Exp. Biol.* 59 (1973), pp. 169–230.

[58] R. J. Wootton. “Palaeozoic insects”. In: *Annu. Rev. Ent.* 26 (1981), pp. 319–344.

[59] K. K. Zabello et al. “Self-consistent numerical model of mosquito dynamics with specified kinematic parameters of wing movement”. In: *Communications in Nonlinear Science and Numerical Simulation* 135 (2024). DOI: 10.1016/j.cnsns.2024.108032.

A

APPENDIX-A: EXPERIMENTAL IMPLEMENTATION CHALLENGES

Experimental Implementation Challenges

A.1. STATIONARY SHOULDER POINT CONSTRAINT

One of the main technical challenges in the early experimental phase was ensuring the *shoulder point* of the wing assembly (the junction between the wing model and the 400 mm cylindrical shaft, representing the insect's wing root) remained fixed in space throughout the kinematic cycle. This stationary condition is essential for maintaining biological fidelity, as any translation of the reference point would alter the aerodynamic characteristics and compromise comparisons with mosquito flight.

The difficulty lay in meeting two competing requirements: (i) prescribing the biologically derived wing tip trajectory, and (ii) keeping the shoulder point fixed. This demanded coordinate transformation algorithms to map the wing tip motion into robot flange coordinates, using trigonometric relations to account for both the shaft geometry and the three-dimensional flapping motion.

To resolve this challenge, a custom reference frame was established at the shoulder point. By placing the coordinate system origin at this point, the need for explicit constraints during motion planning was removed. The kinematics then reduced to defining wing tip coordinates relative to the shoulder origin, directly derived from biological data. Trigonometric operations translated these coordinates into robot flange positions at the opposite end of the 400 mm shaft. This ensured the robot-executed trajectory maintained a fixed shoulder point while accurately reproducing the desired wing tip motion.

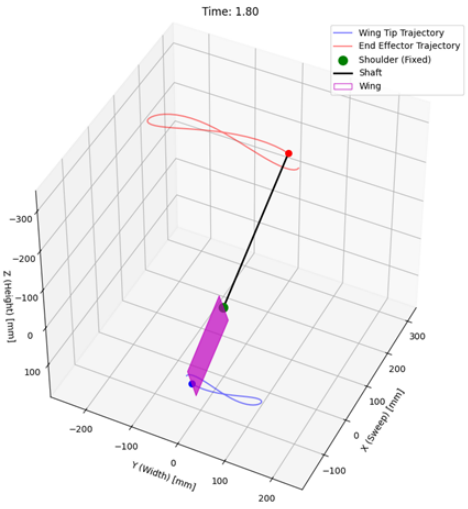

Figure A.1: The establishment of a custom reference frame coordinate system positioned at the shoulder point (Green Point). This approach fundamentally simplified the computational complexity by relocating the coordinate system origin to the shoulder point itself, thereby eliminating the need to explicitly constrain this point during motion planning. With this coordinate transformation in place, the kinematic planning process was reduced to defining the spatial coordinates of the wing tip (Blue Point) relative to the shoulder point origin, which could then be directly derived from the biological kinematic data

A.2. SMOOTH MOTION BETWEEN CYCLES

After resolving the stationary shoulder point constraint, a second challenge arose from jerky robot motion between flapping cycles. At the end of each cycle, the robot paused abruptly, disrupting the continuity of wing motion and introducing unwanted dynamic effects.

Analysis of the VAL3 input code showed the trajectory was programmed as a closed figure-eight loop, with the first and last coordinate points identical. This caused the robot to pause at the common point, creating an unnatural stop in the flapping motion. To correct this, the redundant final point was removed, allowing the controller to transition smoothly from the second-last point back to the first. This modification eliminated the jerky behaviour and ensured a continuous, biologically realistic wing motion.

A.3. TRAJECTORY MATCHING: LEAVE, REACH AND NUMBER OF POINTS OPTIMIZATION

With the robot executing the prescribed motion, the first validation step was to assess trajectory accuracy by comparing the actual path with the input coordinates. As shown in the figures, notable deviations were observed between the programmed and executed trajectories.

Analysis revealed three key parameters driving these discrepancies: the *Leave* param-

eter, the *Reach* parameter, and the number of discretization points. Together, these govern trajectory blending and spatial resolution, directly affecting the robot's ability to reproduce the intended kinematics. Identifying these parameters provided the basis for optimizing the motion profile and minimizing deviations in the wing flapping motion.

A.3.1. THE LEAVE AND REACH

Leave and Reach parameters are fundamental motion control settings in Stäubli robots that govern the blending behaviour when the robot traverses multiple waypoints in a continuous trajectory. These parameters enable the robot to create smooth, continuous motion paths rather than executing rigid point-to-point movements with complete stops at each intermediate waypoint. The blending functionality is particularly critical in applications requiring fluid motion, such as high-speed processes, where maintaining momentum and reducing cycle times are essential.

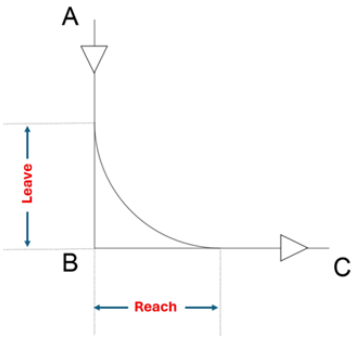

Figure A.2: Leave and Reach Parameter

TECHNICAL IMPLEMENTATION OF LEAVE PARAMETER

The *Leave* parameter defines the distance before an intermediate waypoint where the robot begins deviating from the current trajectory to blend toward the next segment. In joint blend mode, it works in conjunction with the *Reach* parameter (figure A.2). For a path from A through B to C, Leave specifies how far before B the robot curves away from AB to transition smoothly toward BC, allowing higher velocities through the waypoint.

Leave is measured along the approach trajectory (mm). A larger value initiates blending earlier, producing a wider, gradual curve; a smaller value keeps the path closer to B, yielding a tighter transition. Appropriate Leave values balance accuracy, speed, and workspace constraints.

TECHNICAL IMPLEMENTATION OF REACH PARAMETER

The *Reach* parameter complements Leave by defining how far along the departure trajectory the blending continues before fully committing to the straight-line path. In the A–B–C example (figure A.2), Reach specifies the distance along BC where the curved

transition ends and the robot settles onto the direct path to C.

Also specified in millimetres, Reach shapes the geometry of the blended path. Larger values extend the blending region, creating a smoother transition, while smaller values shorten it, leading to a quicker alignment with BC. Optimal Reach values depend on motion requirements, accuracy constraints, and overall trajectory objectives.

BLENDING ALGORITHM USING LEAVE AND REACH

The combined use of *Leave* and *Reach* parameters enables the Stäubli controller to generate blended trajectories that satisfy both kinematic and dynamic constraints. Proper configuration allows the robot to maintain higher average velocities along multi-waypoint paths by avoiding full deceleration–acceleration cycles. The controller computes smooth spline curves between straight-line segments while respecting limits on velocity, acceleration, and jerk.

The blending algorithm uses the specified Leave and Reach distances to keep deviations from waypoints within acceptable limits. This ensures accuracy in precision applications, where excessive blending could cause significant errors. If chosen values risk trajectory violations or unsafe motion, the controller automatically adjusts the parameters to maintain feasible and safe paths.

A.3.2. NUMBER OF DATA POINTS AND TRAJECTORY RESOLUTION

The number of discretization points defining a robotic trajectory strongly affects motion smoothness, accuracy, and execution. Higher point density reduces spacing between waypoints, yielding a finer representation of continuous motion, while fewer points create a coarser approximation. This is critical in applications such as mosquito wing flapping, where biological kinematics must be reproduced through discrete robot positions.

Trajectory quality follows sampling theorem principles: insufficient discretization relative to motion complexity introduces aliasing, producing jerky or discontinuous profiles. Finer discretization improves execution time and velocity smoothness by giving the optimizer more flexibility for transitions, but increases computational load and optimization time. Thus, a balance is required between motion fidelity and efficiency.

ADAPTIVE LEAVE AND REACH PARAMETER ADJUSTMENT

The *Leave* and *Reach* parameters must be adapted to changes in trajectory discretization to maintain smooth motion. With more discretization points, inter-point distances decrease, requiring smaller blending values to avoid over-blending, which could cause the path to miss critical waypoints. Conversely, with fewer points, larger blending radii are needed to avoid abrupt directional changes, though care must be taken to prevent excessive deviation or workspace violations.

For a segment of length L divided into N points, the average spacing is L/N. Leave and Reach should generally scale with this distance, typically 10%–50% of L, depending on smoothness and accuracy requirements. This proportional scaling preserves consistent blending characteristics across different point densities.

Optimizing trajectory accuracy proved one of the most demanding challenges, as motion fidelity depended on the interplay of *Leave*, *Reach*, and discretization density. To verify accuracy, a Python-based tool was developed to animate and track wing tip and robot flange trajectories from predefined kinematic inputs. The program generated interactive 3D animations for inspection before execution and processed text files output by the controller after each run (five flapping cycles). It parsed the data, separated cycles, and overlaid actual trajectories against the input profile. This enabled quantitative assessment of deviations and provided essential feedback for trajectory optimization, ensuring biological fidelity of the flapping motion.

The assessment of motion deviation was conducted using two complementary analytical approaches:

A.3.3. USING TRAJECTORY OVERLAY

The first approach utilized trajectory overlay analysis, where the robot's actual trajectory in each cycle was superimposed against the programmed input motion. The Python program incorporates an interactive three-dimensional interface that enables detailed inspection through zoom and rotation capabilities, allowing for close examination of trajectory conformance at critical points throughout the motion cycle.

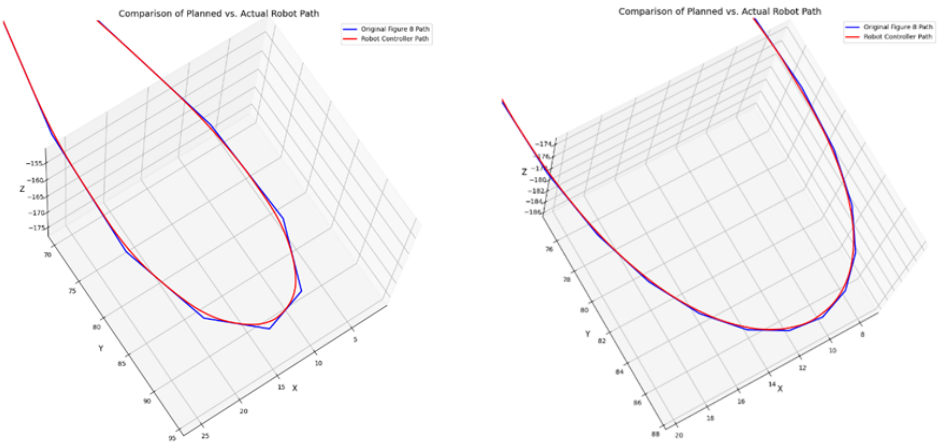

(a) 30 Points

(b) 50 Points

Figure A.3: Trajectory overlay Comparison for 30 data points and 50 data points.

A.3.4. COMPARING EULER ANGLES

A second validation approach analyzed the robot's Euler angles—Sweep, Deviation, and Pitch—since these govern trajectory execution. The analysis program generated overlay plots of actual versus input angle variations for each cycle and calculated the RMS deviation, enabling objective trajectory assessment.

Results showed notable deviations, requiring systematic optimization of motion parameters. A series of trial runs tested combinations of *Leave*, *Reach*, and discretization density. The acceptance criterion was set at an RMS deviation below 0.5°. Optimal performance was achieved with Leave and Reach both set to 10 mm, balancing smooth transitions with path accuracy.

The trials also highlighted discretization effects: too few points produced coarse curvature and large deviations, while too many overloaded the controller, causing unstable motion. An optimum of 50 discretization points was identified, offering the best trade-off between fidelity and computational efficiency, ensuring smooth and accurate reproduction of the biological flapping motion.

A.4. VELOCITY MATCHING: ACCELERATION & DECELERATION LEVELS, AND TIME PERIODS

Following the successful optimization of trajectory accuracy, the focus shifted to addressing the critical challenge of velocity matching, which directly governs the flapping frequency and, consequently, the aerodynamic fidelity of the experimental setup. The velocity of the wing motion is inherently linked to the flapping frequency through the mathematical relationship:

Velocity=2 × Stroke Amplitude × Shaft Length × Frequency.

where Frequency=1/Time Period. This equation establishes the direct proportionality between the robot's linear velocity and the wing's flapping frequency, a key parameter for replicating the dynamic scaling of mosquito flight.

The kinematic definition program, written in Python, expressed wing motion as sinusoidal variations of Sweep, Deviation, and Pitch over a predefined time period. This period also entered Reynolds number calculations, linking wing dimensions to fluid viscosity. An initial value of 2 s balanced Reynolds requirements with workspace and tank constraints.

When implemented, the robot controller autonomously set velocities along the trajectory. Although safety thresholds could be imposed, analysis showed strong deviations from the expected sinusoidal velocity, with non-physical fluctuations at critical points.

To diagnose this, the trajectory was discretized into N points. A Python algorithm computed inter-point distances and derived theoretical velocities from distance/time steps, generating a reference profile that exactly matched the 2 s period. Comparison with

robot outputs revealed significant deviations, especially at the extremes of the figure-eight trajectory where Sweep peaked at 20°. Here, abrupt transitions and offsets appeared, most pronounced during acceleration away from extremes toward the central crossing.

The issue was traced to the robot's motion planning logic, which enforces smooth acceleration/deceleration over strict temporal fidelity. While beneficial for mechanical stability, this introduced nonlinearities incompatible with the required sinusoidal behaviour. This underscored the need for explicit velocity control during trajectory definition to ensure biological fidelity in flapping motion.

A.4.1. ACCELERATION AND DECELERATION EFFECTS

A clear manifestation of velocity non-conformity appeared during initiation and transition phases of the figure-eight trajectory, particularly as the robot moved from an extreme toward the central intersection. At motion onset, the robot showed an initial velocity offset and an acceleration rate inconsistent with the sinusoidal input (figure A.4). The velocity then plateaued before the expected peak at the intersection, remaining distorted as the robot crossed the center and moved to the opposite extreme. These irregularities indicated strong dependence on internal acceleration and deceleration settings.

In the Stäubli system, acceleration defines how quickly velocity increases after departing a point. High values reach target speed faster but create abrupt, non-biological starts. By default, acceleration was set to 100%, favoring rapid attainment over smooth motion. Deceleration similarly governs how quickly the robot slows before a target. While high values ensure fast stops, smooth continuous flapping requires lower deceleration to avoid abrupt halts. The default deceleration was likewise 100%, reflecting an aggressive profile.

Recognizing the influence of these parameters, a design of experiments (DOE) approach was used to investigate maximum velocity, acceleration, and deceleration effects. Acceleration was incrementally reduced, with values down to 40%. Lower rates improved alignment of the initial velocity segment with the sinusoidal input but caused the peak velocity at the intersection to plateau below the required value (figure A.5). Increasing maximum velocity while maintaining reduced acceleration did not resolve this limitation, as peak values remained capped.

Deceleration tests showed further sensitivity. Reducing the rate to 60% degraded the profiles, as the robot slowed excessively near trajectory extremes while preparing to accelerate again. This interplay created step-like artifacts, distorting the sinusoidal shape. These results emphasized the need to finely balance acceleration and deceleration to reproduce input kinematics and preserve the biological fidelity of wing flapping motion.

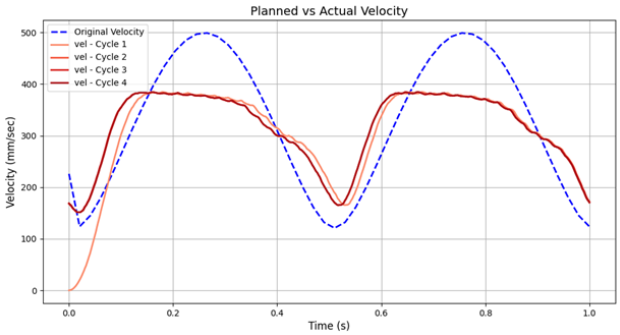

Figure A.4: 400mm shaft at 100perc Acceleration

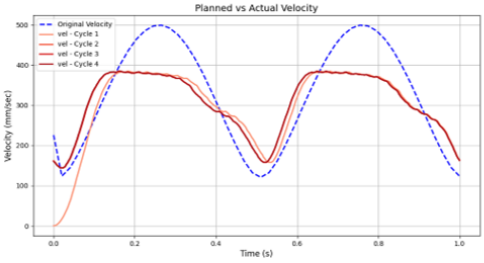

400mm shaft at 80% Acceleration

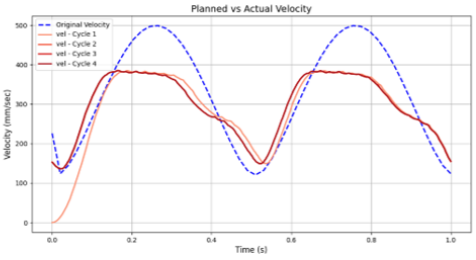

400mm shaft at 60% Acceleration

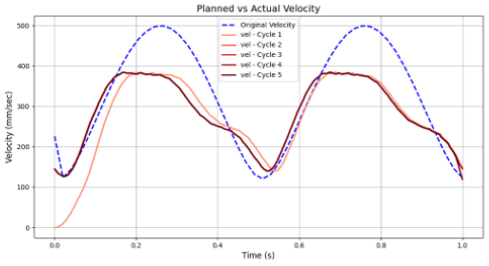

400mm shaft at 40% Acceleration

Figure A.5: Trials with 400mm Shaft

A.4.2. STRATEGIES FOR ADDRESSING ACCELERATION-DECELERATION CHALLENGES

EXTENDED SHAFT LENGTH HYPOTHESIS

The first proposed solution involved increasing the shaft length from the standard 400 mm to 500 mm. The rationale behind this modification was rooted in kinematic scaling principles: a longer shaft would theoretically increase the radius of the end-effector trajectory, thereby providing the robot with additional spatial margin to accommodate acceleration and deceleration transitions. By extending the path length between waypoints, the robot's motion planner would have more time to adjust velocity changes, potentially mitigating the abrupt acceleration-deceleration effects observed in the velocity profiles.

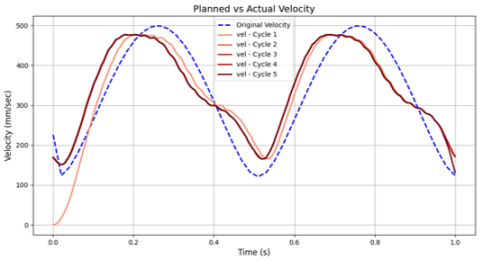

500mm shaft at 100% Acceleration

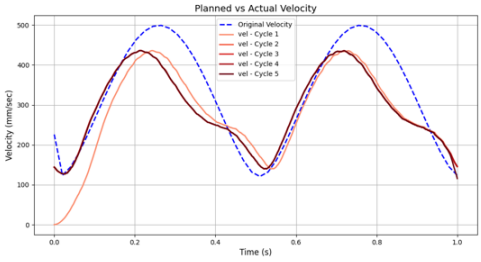

500mm shaft at 40% Acceleration

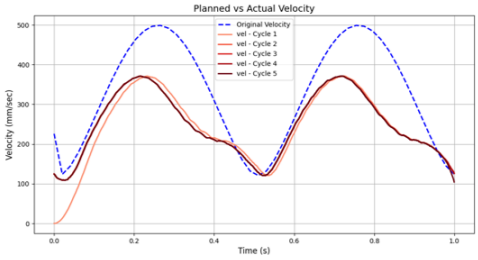

500mm shaft at 40% Acceleration and 60% Deceleration

Figure A.6: Trials with 500mm Shaft

Experimental trials with the 500 mm shaft were conducted under identical kinematic and dynamic conditions as the original 400 mm configuration. However, analysis of the resulting velocity profiles revealed no significant improvements in trajectory conformance or velocity matching. as seen in the figure A.6. The extended shaft length did not alter the fundamental relationship between acceleration settings and velocity plateauing, as the robot's motion planner continued to prioritize smooth transitions over strict adherence to temporal constraints. This outcome suggested that trajectory scaling alone could not resolve the inherent limitations of the robot's motion control algorithms in reconciling acceleration dynamics with biologically derived velocity profiles.

EXPLICIT VELOCITY DEFINITION IN VAL3 CODE

The most effective solution emerged from direct intervention in the robot's motion programming architecture. By incorporating explicit velocity definitions into the VAL3 input code, the reliance on the robot's autonomous velocity calculation was eliminated. A dedicated algorithm was developed to extract the computed velocity values between consecutive trajectory points and embed them directly into the motion program using VAL3 syntax. This approach enforced strict adherence to the predefined velocity profile, overriding the robot's default motion planning logic.

The implementation of explicit velocity commands produced transformative improvements in velocity matching. The robot's velocity profiles now aligned almost perfectly with the input reference at both trajectory extremes and maintained a near-ideal sinusoidal shape throughout the motion cycle. This precision was further validated through derivative analyses of acceleration and jerk profiles, which exhibited excellent conformance to theoretical predictions. The jerk profiles, in particular, confirmed the absence of abrupt changes in acceleration, ensuring smooth motion transitions critical for replicating natural wing kinematics.

TIME PERIOD OPTIMIZATION

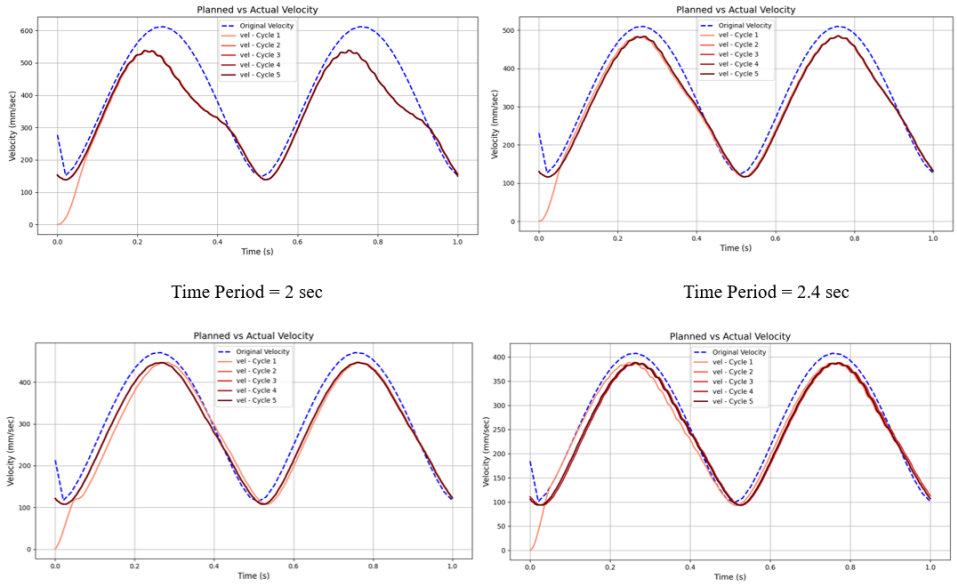

Figure A.7: Time Period Trials

The second strategy focused on increasing the overall cycle time period to reduce peak velocity demands and associated acceleration/deceleration effects. By extending the time period from 2 seconds to values between 2 and 3 seconds, the maximum veloc-

ity required to complete the trajectory decreased proportionally, as per the relationship:

$$\text{Velocity} \propto \frac{1}{\text{Time Period}}.$$

This reduction in peak velocity alleviated the strain on the robot's acceleration capabilities, enabling smoother velocity transitions and reducing the likelihood of velocity capping at trajectory extremes.

Systematic trials within this time period range demonstrated significant improvements in velocity profile fidelity, as seen in figure A.7. At a time period of 2.6 seconds, the velocity profiles exhibited near-sinusoidal behaviour, closely matching the input reference profiles. However, exceeding this optimal value introduced new instabilities, manifesting as wavy or oscillatory velocity patterns, particularly in regions of peak velocity. These oscillations were attributed to the robot's motion planner overcompensating for the reduced velocity demands, resulting in unintended fluctuations during acceleration/deceleration phases. The identification of a 2.6-second time period as the "sweet spot" represented a critical balance between velocity reduction and motion stability, though this solution alone did not fully eliminate residual deviations in the velocity profiles.

COMPREHENSIVE VALIDATION

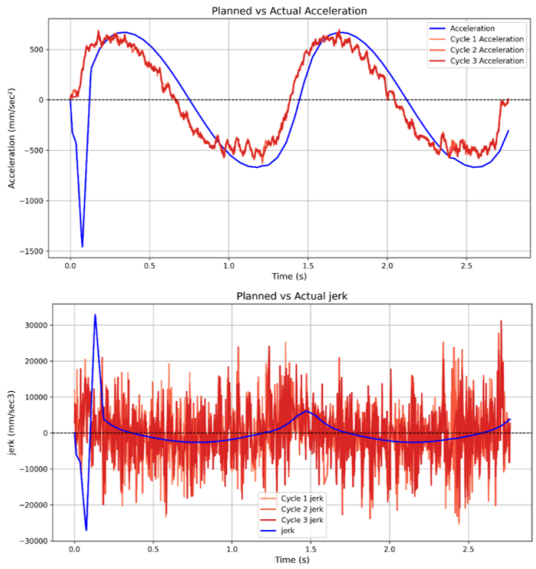

Figure A.8: Acceleration and Jerk Profiles

As a final verification, acceleration and jerk profiles from the robot motion data were compared with values derived from the input kinematics (figure A.8). The profiles showed excellent agreement, with RMS errors reduced to negligible levels. Acceleration matched the expected smooth transitions between segments, while jerk confirmed the absence of

high-frequency oscillations or discontinuities. This validation demonstrated that integrating explicit velocity definitions into the VAL3 code effectively resolved the acceleration–deceleration issues, ensuring the precision required for biologically accurate wing flapping experiments.

A.5. TIME GAP DETECTION AND DATA RECONSTRUCTION

During post-analysis of the robot's output data files, sporadic temporal discontinuities were observed in the recorded time series, manifesting as abrupt jumps or missing data points. Although these anomalies occurred infrequently (affecting less than 0.5% of total data points), their presence necessitated mitigation to ensure data integrity for subsequent analysis. These gaps were attributed to transient communication delays between the robot's motion controller and the data acquisition system, likely exacerbated by the high sampling rate (250 Hz) and computational load during simultaneous motion execution and sensor logging.

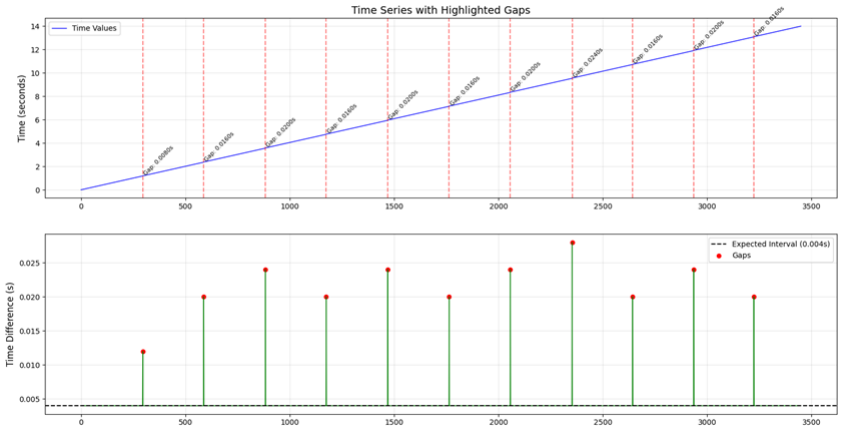

Figure A.9: Time Gap Detection Results

To address this issue, a dedicated Python algorithm was developed to systematically identify and rectify data gaps. The algorithm calculates time intervals between consecutive data points and flags intervals exceeding twice the nominal sampling period (8 ms instead of 4 ms) as potential gaps, as shown in figures A.9 and A.10. For each flagged interval, the number of missing points is computed by dividing the anomalous time difference by the nominal sampling period and subtracting one. This enables precise localization of gaps and quantification of their magnitude.

Identified gaps are reconstructed using linear interpolation between valid data points bracketing the discontinuity. For a gap spanning n missing points between recorded points t_i and t_{i+n+1}, the missing values for position, velocity, force, and torque parameters are calculated as:

$$x_{\text{interp}}(t) = x_i + \left(\frac{x_{i+n+1} - x_i}{t_{i+n+1} - t_i} \right) \cdot (t - t_i)$$

where:

- x_i = value at the start of the gap
- x_{i+n+1} = value at the end of the gap
- t_i = time at the start of the gap
- t_{i+n+1} = time at the end of the gap
- t = time of the interpolated point

This approach ensures first-order continuity in the data while avoiding introduction of artificial high-frequency components that could distort derivative-based analyses.

The reconstructed dataset is subsequently used for all post-processing tasks, including force–torque analysis and kinematic validation.

```
"C:\Users\MANUSANKAR S\AppData\Local\Programs\Python\Python311\python.exe" "D:\
Found 11 time gaps in the data

Gap Summary :
      Line    Time  Previous_Time  Gap_Size  Expected_Points_Missing
296    297   1.196          1.184     0.008                        2
588    589   2.380          2.360     0.016                        4
884    885   3.584          3.560     0.020                        5
1175  1176   4.764          4.744     0.016                        4
1470  1471   5.964          5.940     0.020                        5
1764  1765   7.156          7.136     0.016                        4
2057  2058   8.348          8.324     0.020                        5
2353  2354   9.556          9.528     0.024                        6
2643  2644  10.732         10.712     0.016                        4
2936  2937  11.924         11.900     0.020                        5
3224  3225  13.092         13.072     0.016                        4
```

Figure A.10: Time Gap identified in the staubli output file

A.6. INTERMEDIATE WATER TRIALS AND VIBRATION ANALYSIS

Prior to experiments in the water–glycerol mixture, intermediate trials were conducted in water alone to validate protocols and identify hydrodynamic challenges. This step avoided the time and cost of preparing glycerol mixtures, which require precise volumetric calculations to match target viscosities for Reynolds scaling.

During these trials, strong vibrational oscillations appeared in the wing–shaft assembly, producing high-frequency noise in the force–torque sensor. Although present in dry runs, vibrations intensified in water due to higher density and viscous damping. The effect was traced to fluid–structure interactions (FSI), where unsteady hydrodynamic loading induced shaft–wing resonance, especially during stroke reversals with peak inertial

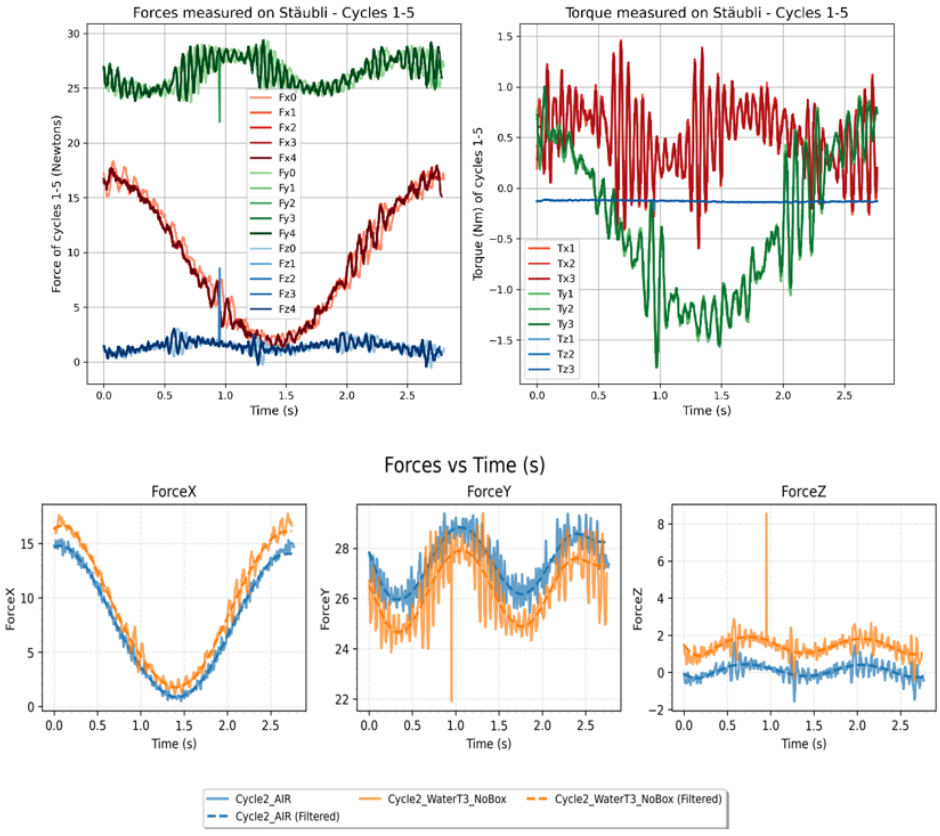

Figure A.11: Intermediate Water Trials

forces.

Force data showed degraded signal-to-noise ratio (SNR), with high-frequency oscillations superimposed on baseline forces. While low-pass filtering could suppress this noise, aggressive filtering risked removing critical high-frequency content from vortex shedding and wake–wing interactions. This created a trade-off: insufficient filtering left structural contamination, while excessive filtering obscured transient flow features vital to unsteady aerodynamic characterization.

To resolve this vibration issues, we came up with a few ideas and approaches, listed below:

A.6.1. IMPROVING THE FIT OF THE WING-SHAFT JOINT

The initial design for attaching the wing to the shaft involved inserting the wing into a U-shaped slot located at the end of the shaft, as illustrated in the accompanying figure. To improve the fit and eliminate any mechanical play, a 1 mm thick aluminium bush plate was inserted into the gap between the wing and the slot. This approach was intended to ensure a snug and stable connection, thereby minimizing unwanted movement during operation.

During intermediate water trials, the aluminium bush plate was found to react chemically with the water. Oxidation (figure A.12) gradually reduced the plate thickness, widening the gap between the wing and shaft slot. This increased mechanical play and vibration, while also causing screw misalignment during wing attachment. The resulting stress on the shaft's internal threads damaged them, requiring rethreading to restore functionality.

To address these issues, the aluminium bush plate was replaced with a stainless steel plate (figure A.13). Stainless steel, being resistant to oxidation and corrosion, preserved its thickness and maintained a tight fit between the wing and shaft slot. This modification improved alignment and eliminated the mechanical play that had contributed to vibration. However, overall noise levels remained high, indicating that while joint stability was enhanced, other factors—likely hydrodynamic forces or fluid–structure interactions—continued to drive the persistent vibrations.

A.6.2. SCREWING ORIENTATION

Initially, the M4 screws used to secure the wing-shaft assembly were inserted from the threaded side of the shaft, with the bush plate positioned on the same side as the screw heads as shown in figure A.14a. This configuration was intended to provide a firm and stable connection by ensuring that the bush plate was tightly compressed against the shaft and wing interface. However, in an effort to further enhance the rigidity of the joint, the assembly method was modified by reversing the orientation: the screws were inserted from the opposite side, and the bush plate was repositioned accordingly as shown in figure A.14b. This adjustment resulted in a noticeable improvement in the

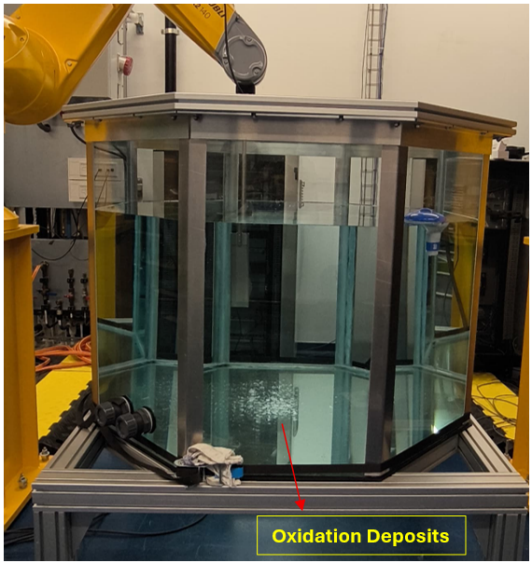

Figure A.12: Oxidation Issue

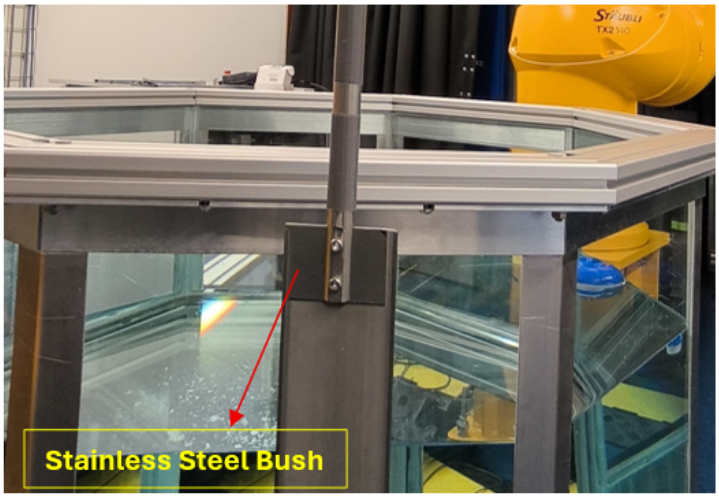

Figure A.13: Steel Bush attachment, in between the wing and the shaft slot, inorder to improve the fit of the joint

overall rigidity of the joint, suggesting a more effective mechanical fit and potentially better distribution of the fastening forces across the assembly.

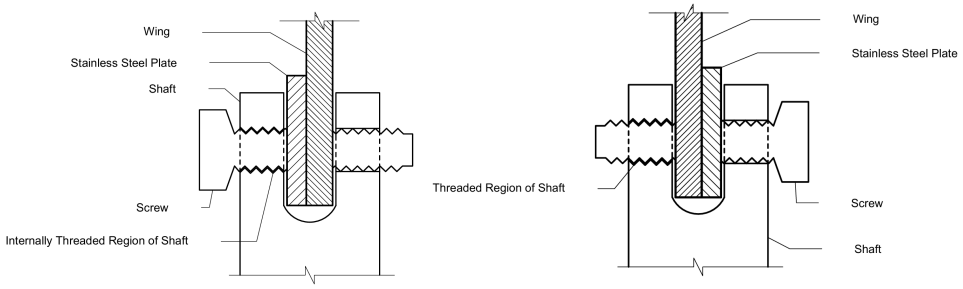

(a) Left-side screwing orientation

(b) Right-side screwing orientation

Figure A.14: Screwing orientations for both left and right sides

Despite the observed increase in structural rigidity, this change in screwing orientation did not translate into a significant reduction in the noise levels associated with vibration during operation. The persistence of vibrational noise indicated that, while the orientation of the screws can influence the mechanical stability of the joint, it is not a dominant factor in controlling the vibrational behaviour of the system.

A.6.3. SHORTER SHAFT LENGTH

To test whether vibrations were caused by the long cantilevered shaft, additional trials were conducted with a shorter 200 mm shaft. The reduced lever arm was expected to raise the natural frequency and lower vibration amplitudes from fluid–structure interactions. This change, however, required recalibration of the frame and mounting to prevent the robot flange from contacting the fluid surface due to the reduced clearance.

Despite these adjustments, the shorter shaft did not reduce vibration levels. This indicated that the oscillations were not solely dependent on shaft length, but likely arose from more complex interactions between the wing assembly and the surrounding fluid environment.

A.6.4. TAPING THE SHAFT FOR VIBRATION DAMPING

To address persistent vibrations, two taping strategies were tested (figure A.15). First, the entire shaft was wrapped with 3M adhesive tape to introduce passive damping via viscoelastic energy dissipation. This was intended to reduce vibrational amplitudes by increasing the structural damping ratio. However, force sensor data showed no measurable decrease in noise or vibration, indicating the tape's damping capacity was insufficient against the excitation forces.

Subsequently, a targeted approach was adopted, wherein tape was applied at specific axial positions along the shaft where theoretical calculations predicted peak vibrational

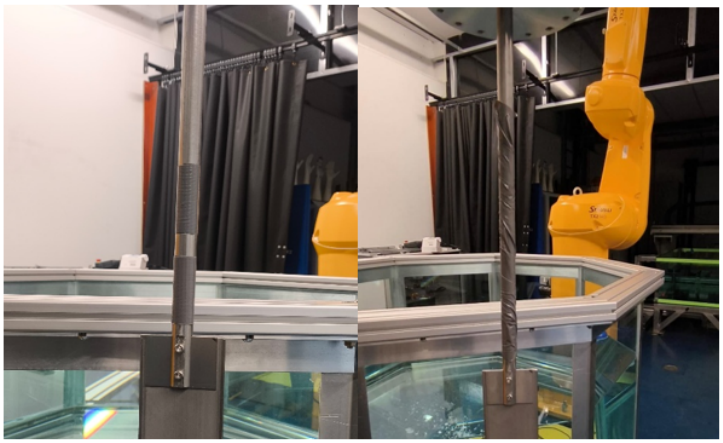

Figure A.15: Shaft Taping

amplitudes associated with the fundamental natural frequency. These positions, illustrated in the accompanying figure, corresponded to anti-nodal regions of the first bending mode. Despite precise placement guided by modal analysis principles, the modified configuration similarly failed to produce a significant reduction in noise or vibration. The lack of improvement suggested that the vibrational energy was either distributed across multiple modes or that the excitation forces—likely originating from unsteady hydrodynamic loads—exceeded the damping capacity of the tape.

A.6.5. SUPPORT STRUCTURE FOR THE SHAFT

In another approach to address the persistent vibrational oscillations observed in the shaft-wing assembly, a conical support structure, shown in figure A.16, was designed and fabricated with the help of DEMO workshop. This intervention aimed to enhance the structural rigidity of the shaft by providing additional mechanical stabilization, thereby reducing vibrational amplitudes. The support structure was engineered with stringent constraints to avoid disrupting the fluid flow around the wing and shaft. Specifically, its design ensured that it remained entirely above the water surface during experiments to prevent interference with the hydrodynamic environment. However, due to the necessity of maintaining clearance from the fluid surface and avoiding contact with the water, the structure could only stabilize a limited portion of the shaft. This partial coverage inherently restricted its ability to dampen vibrations along the entire cantilevered length of the shaft.

Post-implementation trials revealed that the conical support failed to produce a significant reduction in vibrational noise levels. This outcome underscored the limitations of purely mechanical stabilization in mitigating vibrations driven by complex fluid-structure interactions. The persistence of oscillations suggested that hydrodynamic forces—particula unsteady loads generated during wing stroke reversals—remained the dominant excitation source, necessitating alternative strategies.

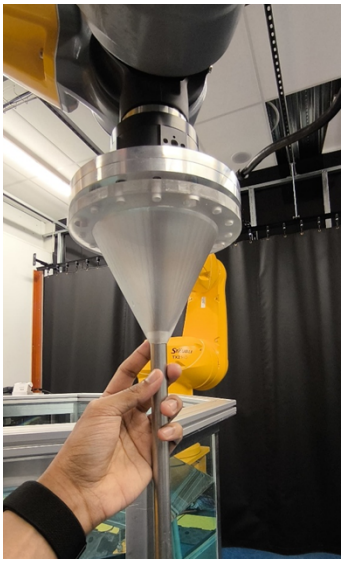

Figure A.16: Conical Support Structure

A.6.6. BOXCAR FILTER FROM STÄUBLI

To address persistent vibration and noise, Stäubli's manufacturer recommended implementing the inbuilt Boxcar filtering technique in the VAL3 environment. The Boxcar filter, a moving-average algorithm, smooths sensor data and motion feedback by averaging consecutive data points. It is effective in attenuating high-frequency noise while preserving lower-frequency signals, making it suitable for steady-state trajectories.

In straight-line trials, the filter improved noise reduction, as the uniform velocity and simple dynamics matched the averaging window. Force–torque outputs showed noticeably cleaner signals. However, during complex figure-eight kinematics with rapid reversals, variable accelerations, and overlapping frequency content, filter performance deteriorated and failed to suppress vibrations effectively.

A.6.7. ANOTHER WING ASSEMBLY

To further investigate vibration sources, an alternative wing assembly was tested (figure A.18). This setup used an aluminium shaft with an aerofoil cross-section and a circular plexiglass wing. Both components were smaller and lighter than the stainless-steel counterparts, reducing the overall mass of the assembly.

Contrary to expectations, vibration levels did not decrease significantly. Force–torque data showed dominant frequency peaks consistent with the original setup, indicating that the fundamental vibrational modes were preserved. The lighter assembly did, how-

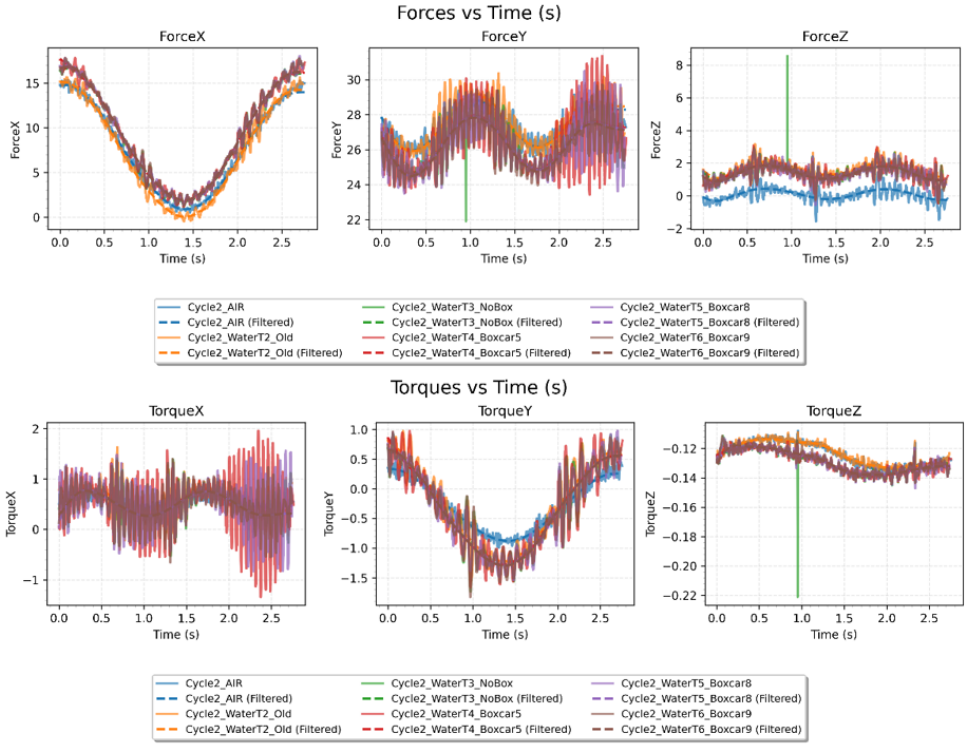

Figure A.17: Noise Level

ever, show reduced noise amplitude due to lower inertial forces.

These results suggest that while assembly mass affects vibration magnitude, the dominant excitation frequencies are driven by fluid–structure interactions, particularly periodic hydrodynamic loads during stroke reversals.

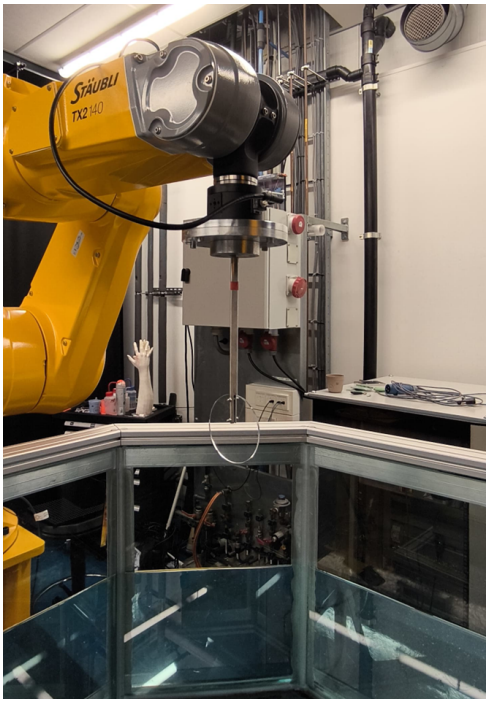

Figure A.18: Another Wing Assembly

A

Appendix-B: Data Post-Processing Challenges

Data Post-Processing Challenges

B.1. Experimental Force Anomalies

A major post-processing challenge was configuring and validating the transformation matrices required to convert forces from the wing's co-rotating system to the global frame. The difficulty arose from differences in axis definitions between the Stäubli robot and the quasi-steady aerodynamic model. In the quasi-steady model, the X-axis lies along the span, the Y-axis is normal to the wing surface, and the Z-axis runs along the chord. In contrast, the Stäubli system defines the X-axis along the span but normal to the surface, while the Y-axis aligns with the chord. This subtle yet critical difference meant the quasi-steady rotation matrices could not be applied directly. Instead, new matrices had to be derived to match the Stäubli conventions, ensuring physically consistent force projections in the global frame.

Redefining and implementing the correct transformation matrices required great care, as even small axis misalignments could cause large errors in global force components. To verify correctness, hydrodynamic normal forces (after subtracting inertial effects) were input into the transformation pipeline. Unexpectedly, the resulting global force trends differed strongly from quasi-steady model predictions, raising concerns about the transformation.

To isolate the source, wing normal force data from the quasi-steady model were processed through the Stäubli transformation program. This yielded an exact match in the global force trends, confirming that the matrices were correctly implemented and that the discrepancy originated from the Stäubli hydrodynamic input data rather than the transformation itself.

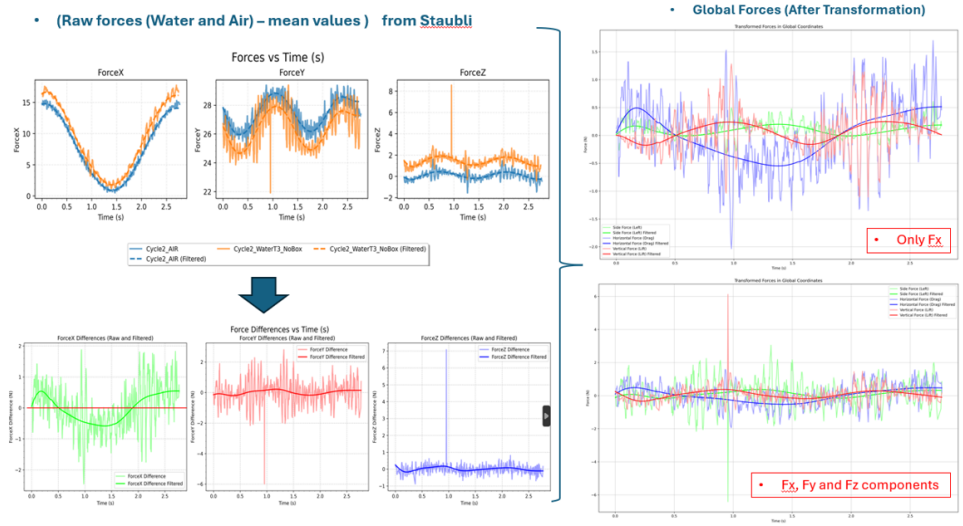

Figure A.1: Anomaly in Transformed Forces

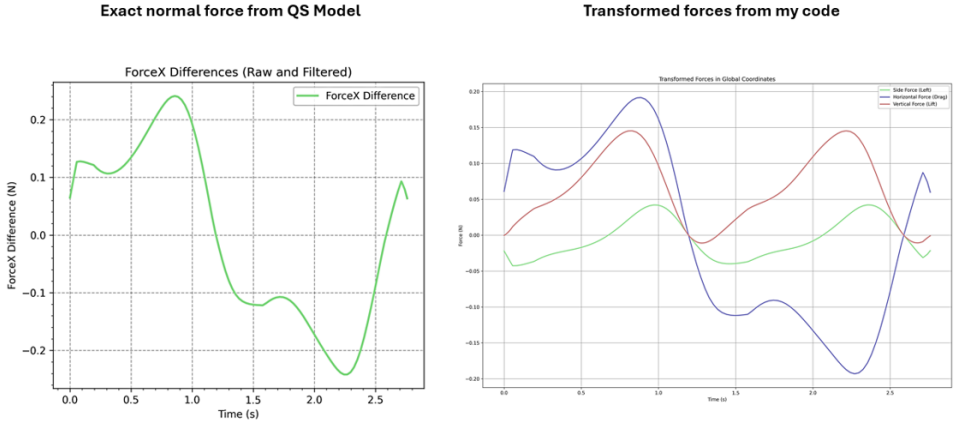

Figure A.2: Transformation of QS Normal Forces

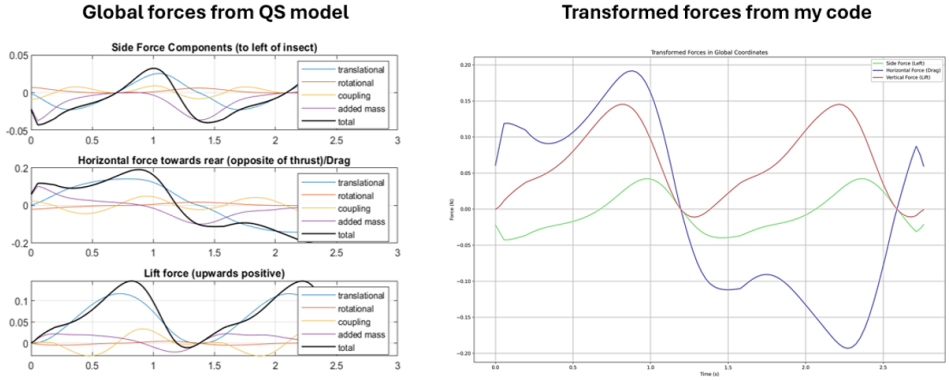

Figure A.3: Transformation Comparison

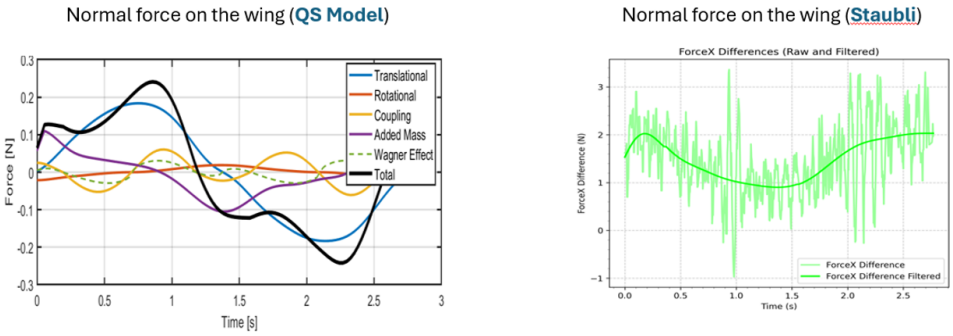

Figure A.4: Normal Force Comparison

Further analysis of the normal force data revealed strong discrepancies between quasi-steady predictions and Stäubli measurements. The quasi-steady model produced a predominantly sinusoidal profile, consistent with periodic flapping and pitching, whereas the experimental data—despite inertial corrections—showed a parabolic, U-shaped trend. Instead of oscillating between positive and negative values, the measured forces remained largely on one side of the axis, suggesting a systematic bias or unaccounted effect in measurement or processing. This anomaly was reinforced when comparing F_x normal force trends between air and water trials, where the expected oscillatory behaviour was largely absent. These findings emphasized the need to carefully reconsider how inertial and hydrodynamic contributions were being measured, separated, and interpreted.

B.1.1. EFFECT OF SUBMERGED SHAFT LENGTH

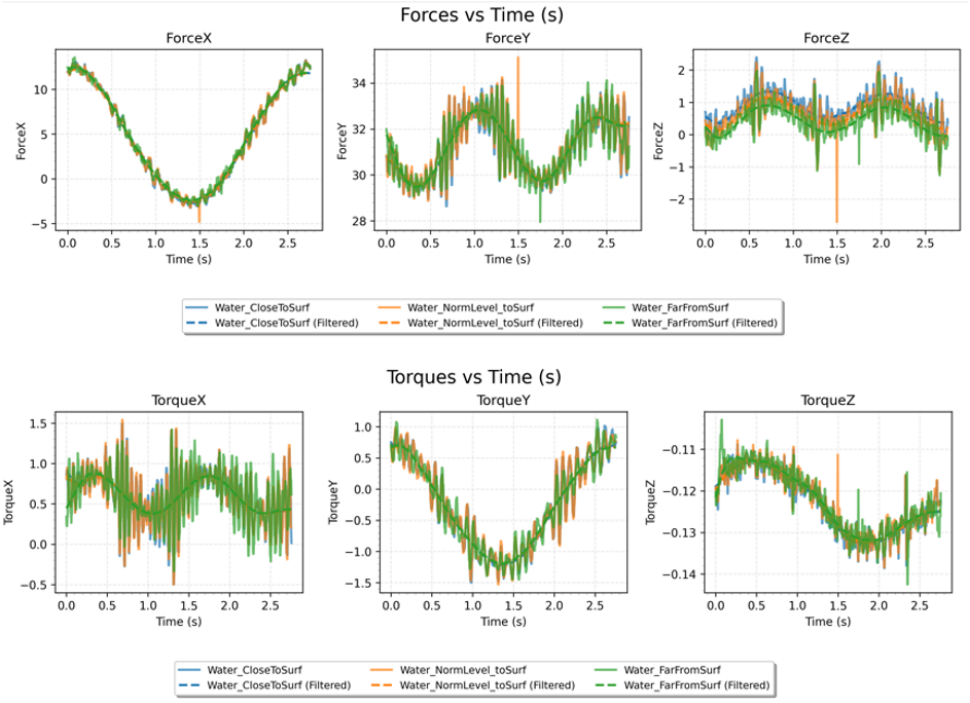

Figure A.5: Effect of Submerged Shaft Length

To examine whether submerged shaft length influenced force measurement accuracy, controlled trials were conducted under three configurations. The hypothesis was that different submerged lengths could generate counteracting hydrodynamic forces, biasing the normal force readings.

In the first configuration, the shoulder point was positioned near the water surface, submerging only ~50 mm of the shaft. The second (standard) configuration submerged 160 mm, with a 300 mm clearance between the wing tip and tank bottom. In the third, the

shaft was submerged further, leaving only 50 mm above the surface.

Force measurements were recorded for normal, chordwise, and spanwise components under each configuration. Results showed negligible differences in normal and chordwise forces, but a consistent offset of ~0.1 N in the spanwise component. Thus, submerged shaft length did not significantly affect primary aerodynamic forces but introduced a minor spanwise bias.

Across all trials, baseline force readings showed a persistent offset from zero, indicating a systematic bias in the measurement system independent of shaft depth. These findings suggest that while shaft submergence has minimal influence on main force components, careful baseline correction and further investigation of the offset source are required to ensure measurement reliability.

B.1.2. TRIALS WITH AND WITHOUT THE WING ATTACHED

To further delineate the influence of the submerged shaft on force measurements, additional trials were conducted in which the flapping kinematics were executed both with and without the wing attached to the shaft. This approach was designed to isolate and compare the contributions of the wing and shaft to the overall force readings, thereby clarifying whether the shaft itself was introducing significant hydrodynamic effects.

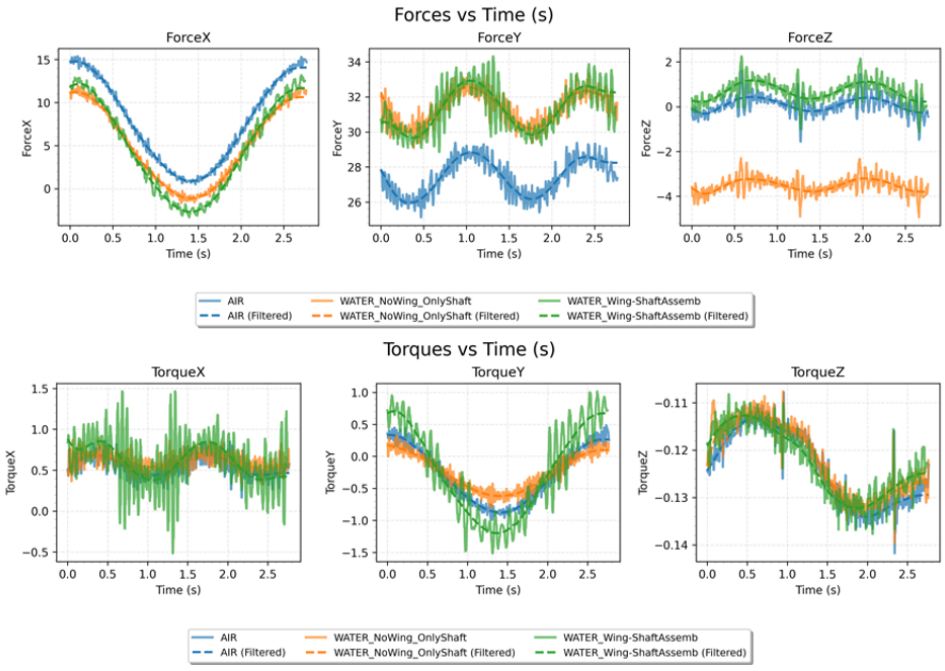

Figure A.6: Effect of Attached Wing

The analysis focused on the spanwise force component (F_z). A consistent ~4 N difference was observed between two configurations, closely matching the measured wing weight of 4.1 N. This correspondence indicated that the shaft's contribution to measured forces was negligible, with the primary effect arising from the presence or absence of the wing.

Nonetheless, a persistent fixed offset in force values appeared in all trials, independent of wing attachment. This suggests an inherent default offset in the sensor or gradual calibration drift over repeated use. The result emphasizes the need for regular verification and recalibration of the force sensor to ensure data accuracy and reliability.

B.1.3. REVERSING THE SENSOR ORIENTATION

To test whether the force offsets were intrinsic to the sensor, the wing assembly was rotated relative to the robot flange so that the normal force, previously measured along the F_x axis, aligned with F_y. The rationale was that if the offset observed in F_x arose from inherent sensor bias, an identical offset should appear in F_y after reorientation.

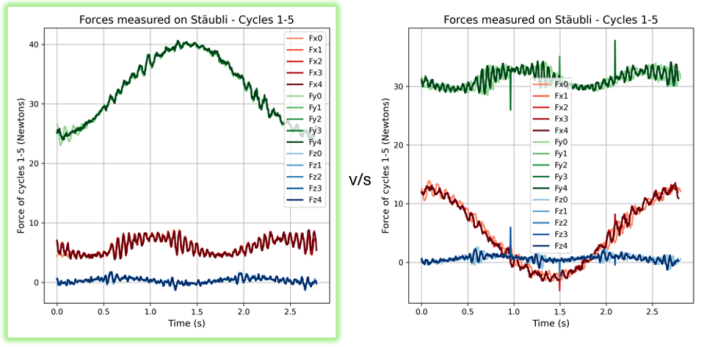

Here Fy is the normal force on Wing surface

Here Fx is the normal force on Wing surface

Figure A.7: Effect of reversing Sensor Orientation

The reversed-orientation experiment confirmed the hypothesis: the offset previously seen in F_x appeared in F_y, while F_x no longer showed the shift. This demonstrated that the persistent offset did not arise from setup, hydrodynamic effects, or processing errors, but from an intrinsic bias within the sensor.

This bias explained why measured normal forces failed to oscillate about zero as expected for periodic flapping. The offset displaced the entire force profile, making baseline correction essential to ensure that subsequent analyses reflect the true physical forces on the wing.

B.2. SENSOR OFFSET AND DRIFT

After identifying sensor offset as the source of anomalous normal force behaviour, it was necessary to characterize its magnitude and stability. Static measurements were there-

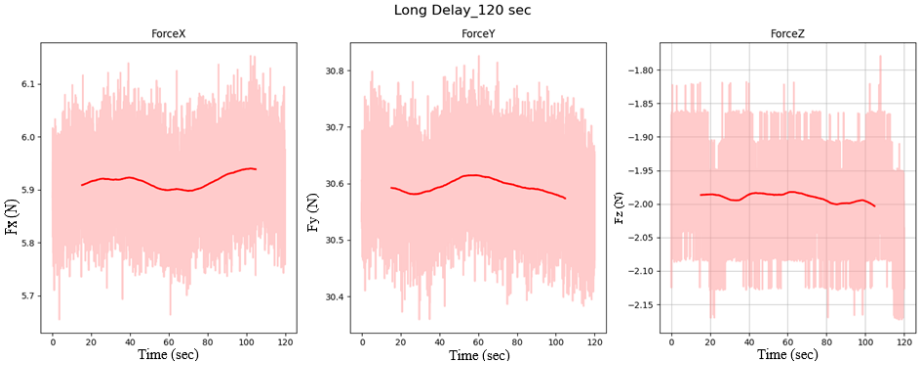

(a) Variation of force reading during a 120 second static trials. Here we see a small drift in the sensor readings with time.

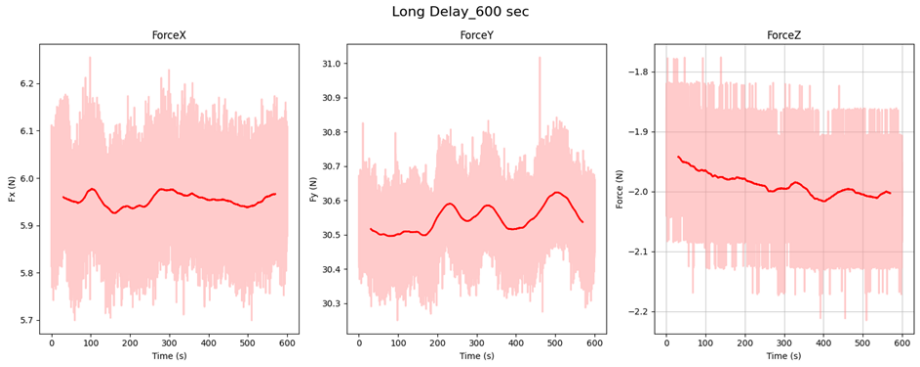

(b) Variation of force reading during a 600 second static trial. Here clearly, the drift in sensor readings with time is very evident.

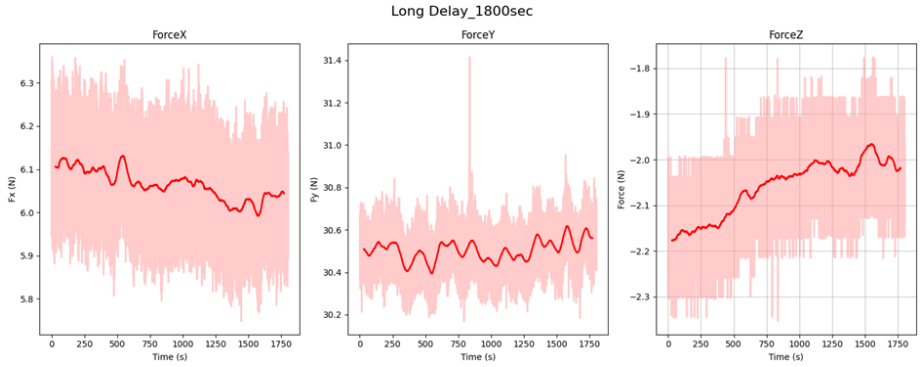

(c) Variation of force reading during a 1800 second static trials. We clearly see a significant drift in the sensor readings with time.

Figure A.8: Sensor drift across different durations of static trials.

fore conducted with the robot carrying only the shaft, with the wing removed to eliminate aerodynamic and inertial effects. The robot was kept stationary throughout, ensuring that any variations in sensor output arose solely from electronic drift or intrinsic sensor instability, as external disturbances such as airflow or vibration were negligible under controlled laboratory conditions.

Sensor readings were collected over 120, 600, and 1800 s intervals. Results confirmed a persistent baseline offset and revealed time-dependent drift (figure A.8). At 1800 s, F_z drifted by up to 0.2 N and F_x by ~0.1 N, indicating that the sensor bias was not fixed but subject to temporal fluctuations, likely from electronic drift or internal effects.

It was concluded that the force–torque sensor exhibits both a fixed offset and time-dependent drift, each capable of introducing significant error if uncorrected. To ensure accuracy, offsets must be measured immediately before and after each trial, with the mean subtracted from the experimental data. This procedure corrects both the baseline bias and interim drift, yielding a more accurate representation of true aerodynamic forces for post-processing and analysis.

B.3. SHIFT IN FORCE TIME DATA ACROSS CYCLES

During isolation of hydrodynamic forces, trials in air without the wing showed a progressive drift in measured forces, beginning from the second cycle onward. This drift was most evident at low deviation angles (0–2.5°), where forces shifted increasingly with each cycle. In contrast, trials at higher deviation angles exhibited stable kinematic profiles across cycles.

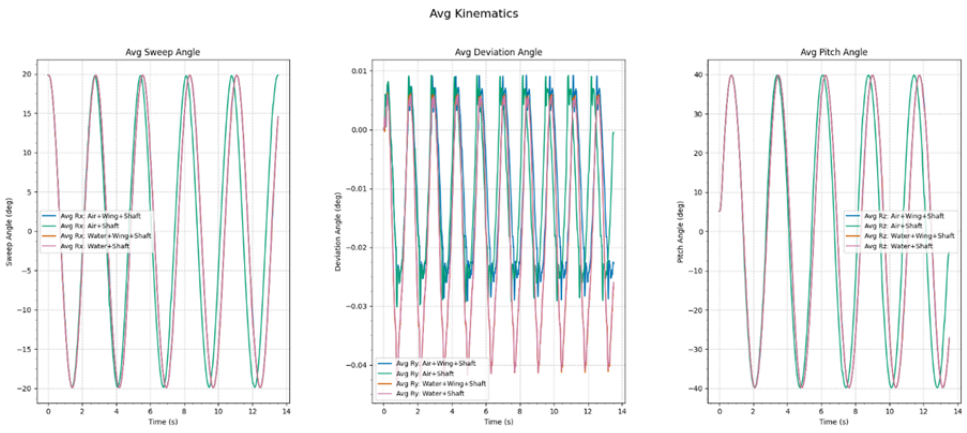

Figure A.9: Shift in Euler Angles

This cycle-dependent drift directly affected the calculation of isolated hydrodynamic force amplitudes. In the baseline Air+shaft configuration (orange line in the analysis), any drift in the measured force—subtracted from the total wing+shaft force in water—artificially

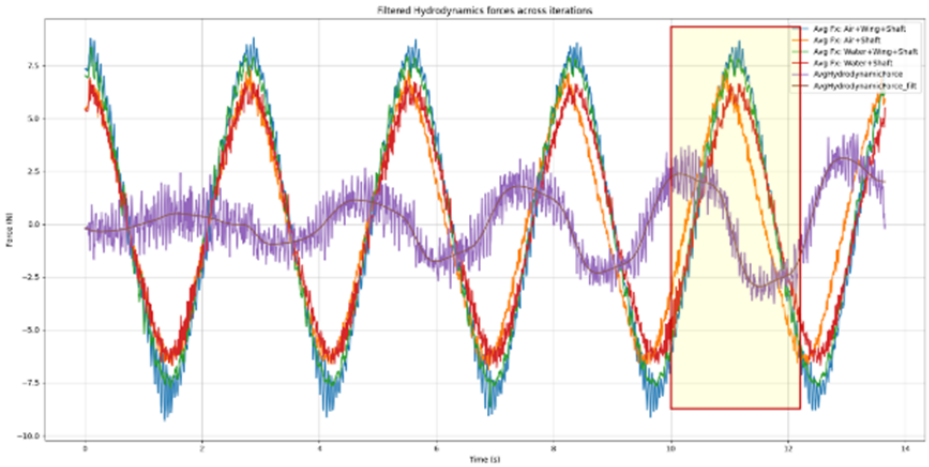

Figure A.10: Shift in Transformed Forces for the zero deviation angle case.

inflated the computed hydrodynamic contribution over successive cycles. If uncorrected, this effect introduces significant errors in interpreting aerodynamic performance.

To mitigate the influence of drift, the second cycle of the five recorded was selected as the reference for all calculations and force transformations. This choice avoided startup transients in the first cycle and the pronounced drift appearing from the third cycle onward, particularly at low deviation angles. Using the second cycle ensured that isolated hydrodynamic forces reflected the true physical response.

To validate the drift source, air-only dry runs were repeated across all deviation angles. Unlike the original dry-run data, the repeated tests showed no cycle-to-cycle drift and a stabilized offset, confirming that the earlier drift originated from inconsistencies in the initial dry runs rather than fluid–structure interaction in water. These corrected dry-run data were then adopted as the baseline for hydrodynamic force isolation, improving the accuracy of aerodynamic force estimation across deviation angles.

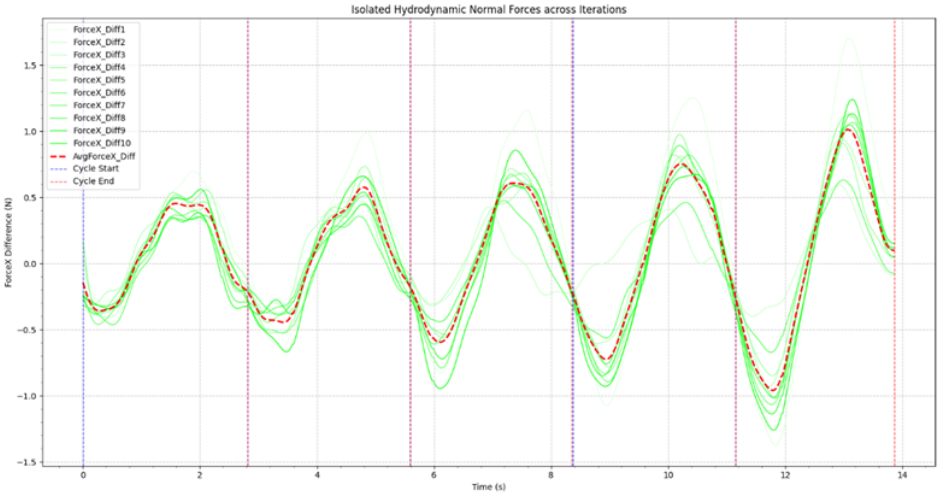

Figure A.11: Shift in Normal isolated hydrodynamic Forces across 5 cycles. we clearly see the increasing trend in the peak amplitudes, resulting from the shift/drift in the force signal.

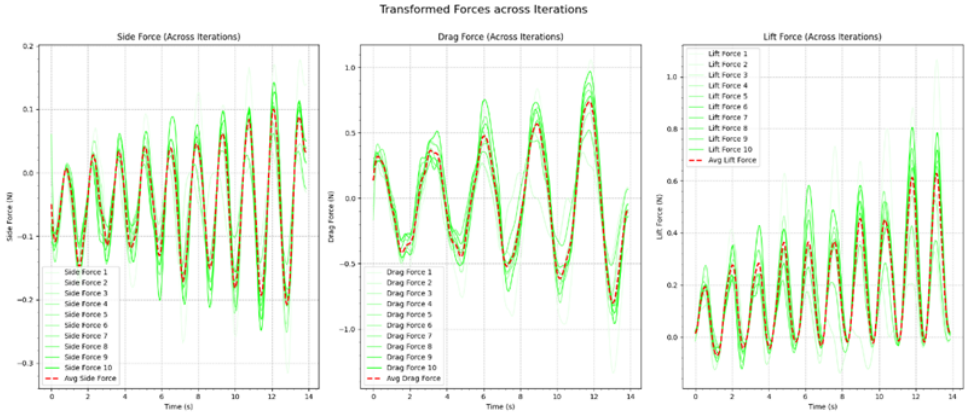

Figure A.12: Shift in Transformed Forces across 5 Cycles

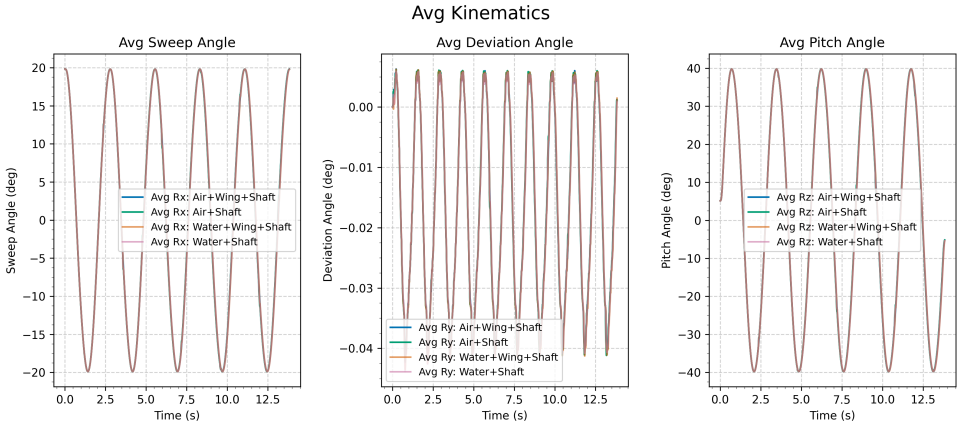

Figure A.13: Average Kinematics after the repetition of the Dry Runs. The results shows that offset/drift seen earlier did not appear anymore.

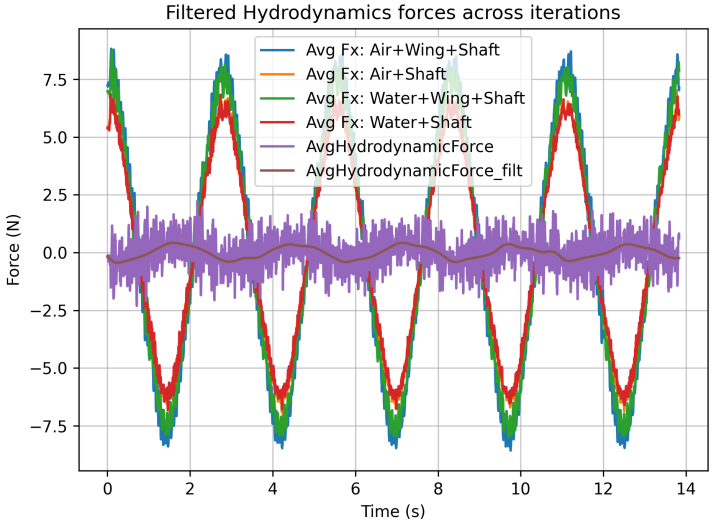

Figure A.14: Figure showing the individual forces from the Wet and Dry runs, as well as the isolated hydrodynamic forces after repetition of the dry runs, for the zero deviation case. Here again we see that we do not see the drift in forces signal across the cycle as we saw earlier. This is an evidence to the fact that repeating the dry runs rectified the drift issue.

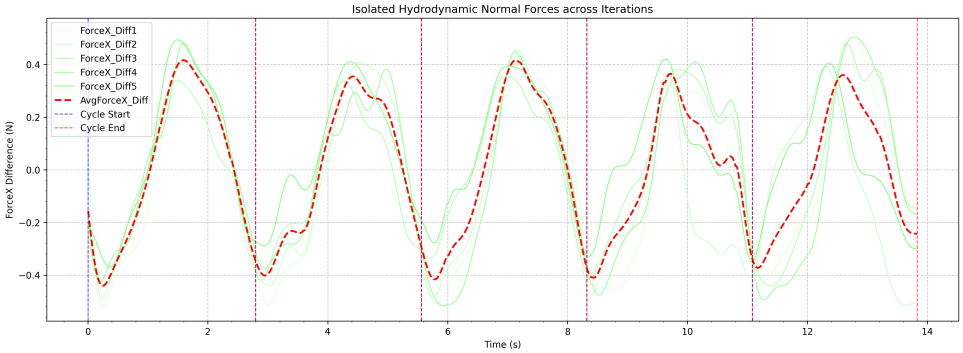

Figure A.15: This image shows the variation of the isolated hydrodynamic forces across the 5 cycles, for the zero deviation case, after incorporating the repeated dry run data. As seen, the peak amplitudes remains fairly constant throughout unlike the growing trend we saw earlier.

A

Appendix-C: Code Snippets

Python and Matlab Code Snippets

C.1. Rotational Matrices for Staubli Configuration

```
1
2
3  # Initialize arrays for transformed forces
4  F_exp_global = np.zeros((3, len(Time)))
5  F_exp_global_Filt = np.zeros((3, len(Time)))
6
7  # Apply transformation for each time step
8  for ii in range(len(Time)):
9  Phi_inst = Phi[ii]
10 Theta_inst = Theta[ii]
11 Alpha_inst = Alpha[ii]
12
13
14 # Create rotation matrices (Updated version)
15 R_phi = np.array([[np.cos(Phi_inst), -np.sin(Phi_inst), 0],
16                   [np.sin(Phi_inst), np.cos(Phi_inst), 0],
17                   [0, 0, 1]])
18
19 R_theta = np.array([[1, 0, 0],
20                     [0, np.cos(Theta_inst), -np.sin(Theta_inst)
                           ],
21                     [0, np.sin(Theta_inst), np.cos(Theta_inst)
                           ]])
22
23 R_alpha = np.array([[np.cos(Alpha_inst), 0, np.sin(Alpha_inst)
       ],
24                     [0, 1, 0],
```

```
                    [-np.sin(Alpha_inst), 0, np.cos(Alpha_inst)
                        ]])

# Combined rotation matrix
R_all = R_phi @ R_theta @ R_alpha


# Force vectors in wing coordinates (customize as needed)
F_exp_wing = np.array([ForceX_Diff[ii], 0, 0])
                                ######## Change    ##############


F_exp_wing_Filt = np.array([ForceX_Diff_Filt[ii], 0, 0])
                ######## Change    ##############


# Transform to global coordinates
F_exp_global[:, ii] = R_all @ F_exp_wing
F_exp_global_Filt[:, ii] = R_all @ F_exp_wing_Filt
```

Listing A.1: Rotational Matrices and its implementation in Python

```
% Wing kinematics in Fourier series form for MATLAB quasi-steady model
% Generated from CSV data
t = linspace(0,1/(freq_factor),101)';
% Kinematics from CSV data
phase_shift = 0;
Alpha = (pi/180)*(.............
    amp_factor*-0.00197106*cos(freq_factor*0*t + 0 + phase_shift) + ...
    amp_factor*39.99454560*cos(freq_factor*6.28318531*t + -1.56356504 + phase_shift) + ...
    amp_factor*0.18996013*cos(freq_factor*12.56637061*t + -1.59284083 + phase_shift) + ...
    amp_factor*0.44578306*cos(freq_factor*18.84955592*t + -0.77034481 + phase_shift) + ...
    amp_factor*0.07884407*cos(freq_factor*25.13274123*t + -1.52886120 + phase_shift) + ...
    amp_factor*0.13574376*cos(freq_factor*31.41592654*t + -1.84525910 + phase_shift) + ...
    amp_factor*0.05229384*cos(freq_factor*37.69911184*t + -1.56164381 + phase_shift) + ...
    amp_factor*0.03889506*cos(freq_factor*43.98229715*t + -1.74587373 + phase_shift) + ...
    amp_factor*0.03786950*cos(freq_factor*50.26548246*t + -1.57336319 + phase_shift));

%%%%%%%% -ve sign for Theta, to match robot kinematics
Theta = -1*(pi/180)*(.............
    amp_factor*-0.06086584*cos(freq_factor*0*t + 0 + phase_shift) + ...
    amp_factor*0.01219220*cos(freq_factor*6.28318531*t + -1.55824887 + phase_shift) + ...
    amp_factor*2.47761284*cos(freq_factor*12.56637061*t + 1.55864930 + phase_shift) + ...
    amp_factor*0.02135080*cos(freq_factor*18.84955592*t + 1.53391367 + phase_shift) + ...
    amp_factor*0.05033467*cos(freq_factor*25.13274123*t + 2.54231122 + phase_shift) + ...
    amp_factor*0.00874669*cos(freq_factor*31.41592654*t + 1.64271983 + phase_shift) + ...
    amp_factor*0.01559014*cos(freq_factor*37.69911184*t + 1.28936546 + phase_shift) + ...
    amp_factor*0.00591963*cos(freq_factor*43.98229715*t + 1.58594326 + phase_shift) + ...
    amp_factor*0.00471730*cos(freq_factor*50.26548246*t + 1.37183586 + phase_shift));

Phi = (pi/180)*(.....................
    amp_factor*-0.07264435*cos(freq_factor*0*t + 0 + phase_shift) + ...
    amp_factor*19.80878199*cos(freq_factor*6.28318531*t + -0.01011429 + phase_shift) + ...
    amp_factor*0.04715590*cos(freq_factor*12.56637061*t + -0.05228516 + phase_shift) + ...
    amp_factor*0.18501972*cos(freq_factor*18.84955592*t + 1.34344709 + phase_shift) + ...
    amp_factor*0.00931547*cos(freq_factor*25.13274123*t + 0.19555043 + phase_shift) + ...
    amp_factor*0.04783469*cos(freq_factor*31.41592654*t + -0.10329974 + phase_shift) + ...
    amp_factor*0.00508555*cos(freq_factor*37.69911184*t + 0.12101291 + phase_shift) + ...
    amp_factor*0.00605009*cos(freq_factor*43.98229715*t + -1.26761472 + phase_shift) + ...
    amp_factor*0.00250341*cos(freq_factor*50.26548246*t + 0.07190316 + phase_shift));

Time = t./(Freq); % t was already defined including freq_factor!


end
```

Figure A.1: Fourier Transform of the kinematics performed on Staubli, that goes as input to the Quasi-steady model.

```
%% transform F_y_c_XXX into F_lift_XXX
% loop through time
F_trans = zeros(3,length(F_y_c_trans));
F_rot = zeros(3,length(F_y_c_rot));
F_coup = zeros(3,length(F_y_c_coup));
F_am = zeros(3,length(F_y_c_am));
F_we = zeros(3,length(F_y_c_we));
for ii = 1:length(Time)

    Phi_inst   = Phi(ii);
    Theta_inst = Theta(ii);
    Alpha_inst = Alpha(ii);

    R_phi = [cos(Phi_inst) -sin(Phi_inst) 0 ; sin(Phi_inst) cos(Phi_inst) 0 ; 0 0 1]; % checked correct as per paper (eqn 1)
    R_theta = [cos(Theta_inst) 0 sin(Theta_inst) ; 0 1 0 ; -sin(Theta_inst) 0 cos(Theta_inst)];  % checked correct as per paper (eqn 1)
    R_alpha = [1 0 0 ; 0 cos(Alpha_inst) -sin(Alpha_inst) ; 0 sin(Alpha_inst) cos(Alpha_inst)];  % checked correct as per paper (eqn 1)
    R_all = (R_phi)*(R_theta)*(R_alpha);

    F_trans(:,ii) = R_all*[0 ; F_y_c_trans(ii) ; 0];
    F_rot(:,ii) = R_all*[0 ; F_y_c_rot(ii) ; 0];
    F_coup(:,ii) = R_all*[0 ; F_y_c_coup(ii) ; 0];
    F_am(:,ii) = R_all*[0 ; F_y_c_am(ii) ; 0];
    F_we(:,ii) = R_all*[0 ; F_y_c_we(ii) ; 0];

end

F_total_partial = F_trans + F_am; % used for testing
F_total = F_trans + F_rot + F_coup + F_am; % + F_we;
F_y_c_total = F_y_c_trans + F_y_c_rot + F_y_c_coup + F_y_c_am; % + F_y_c_we;
```

Figure A.2: Rotational Transforms used in QS Model